Thermal transport in strontium titanite and europium(II) titanate

Shan Jiang

▶ **To cite this version:**

Shan Jiang. Thermal transport in strontium titanite and europium(II) titanate. Condensed Matter [cond-mat]. Sorbonne Université, 2023. English. NNT : 2023SORUS472 . tel-04435118

HAL Id: tel-04435118
https://theses.hal.science/tel-04435118

Submitted on 2 Feb 2024

HAL is a multi-disciplinary open access archive for the deposit and dissemination of scientific research documents, whether they are published or not. The documents may come from teaching and research institutions in France or abroad, or from public or private research centers.

L'archive ouverte pluridisciplinaire **HAL**, est destinée au dépôt et à la diffusion de documents scientifiques de niveau recherche, publiés ou non, émanant des établissements d'enseignement et de recherche français ou étrangers, des laboratoires publics ou privés.

SORBONNE UNIVERSITÉ

ESPCI PARIS | PSL

THÈSE DE DOCTORAT
DE SORBONNE UNIVERSITÉ

Spécialité : Physique

École doctorale nº564: Physique en Île-de-France

réalisée

au Laboratoire de Physique et d'Étude des Matériaux

sous la direction de Kamran BEHNIA and Benoît FAUQUÉ

présentée par

Shan JIANG

pour obtenir le grade de :

DOCTEUR DE SORBONNE UNIVERSITÉ

Sujet de la thèse :

Transport de chaleur dans le titanate de strontium et titanate d'europium(II)

soutenue le le 20 octobre 2023

devant le jury composé de :

M.	Johan CHANG	Rapporteur
M^{me}	Sylvie HEBERT	Rapporteur
M.	Stephen ROWLEY	Examinateur
M.	Abhay SHUKLA	Examinateur
M.	Kamran BEHNIA	Directeur
M.	Benoît FAUQUÉ	co-Directeur

Abstract

In this thesis, we systematically studied the thermal transport properties in two quantum para electrics: strontium titanate($SrTiO_3$) and Europium Titanate ($EuTiO_3$).

In the first part, we reported a study on the thermal Hall effect in $SrTiO_3$ evolving with atomic substitution. When Sr is substituted by Ca stabilizing the ferroelectric order, the thermal Hall effect coming from the phonon is suppressed which points to the role of ferroelectric fluctuations in generating the thermal Hall effect. It is amplified by removing oxygen atoms and the emergence of dilute metallicity. In this case, we identify a new source of the thermal Hall effect, which is phonon drag in the context of an exceptionally large electronic Hall angle.

In the second part, we focus on the electronic thermal conductivity in Nb-doped $SrTiO_3$. By separating electron and phonon contributions to heat transport, we extract the electronic thermal resistivity and show that it displays a T-square temperature dependence. Then compared with its T-square electrical resistivity, we found that the Wiedemann-Franz law strictly holds in the zero-temperature limit but the two T-square prefactors are different by a factor of ≈ 3. It's similar to other Fermi liquids. Recalling the case of ^{3}He, we argue that T-square thermal resistivity does not require Umklapp events. The approximate recovery of the Wiedemann-Franz law in the presence of disorder would account for a T-square electrical resistivity without Umklapp.

In the third part, We studied the electric, thermoelectric, and thermal transport properties of $EuTiO_3$. The temperature dependence of electric resistivity and the Seebeck coefficient allowed us to conclude that the insulating band gap is 0.22 eV. Moreover, the thermal conductivity of $EuTiO_3$ is drastically reduced and has an amplitude and temperature dependence akin to amorphous silica. After excluding the Eu^{+3} impurities, We proposed two mechanisms that impede the thermal conductivity in $EuTiO_3$: one is valence fluctuation. The energy of the highest optical phonon in this crystal structure and the distance between the Eu f-level and the chemical potential are both around 0.1 eV. The other is the superexchange interaction between Eu spins that occurs through Ti ions.

Keywords:

Quantum paraelectric, thermal Hall effect, T-square resistivity and glass-like thermal conductivity

Remerciements/Acknowledgements

Remerciements

Tout d'abord, je tiens à exprimer ma sincère reconnaissance envers mon superviseur, Kamran Behnia. Il a été ma lumière directrice, me guidant vers les domaines de pointe de la recherche, élargissant mes horizons et fournissant une orientation inestimable tant en ce qui concerne les méthodologies que la pensée critique. Je tiens également à exprimer ma gratitude envers mon co-directeur, Benoît Fauqué, qui non seulement a partagé une connaissance approfondie des aspects expérimentaux, mais a également tendu la main pour m'aider à surmonter divers défis de la vie. Leur soutien et leur mentorat ont joué un rôle déterminant dans la conception de ma thèse et ma préparation à la présentation de ma défense.

Ensuite, j'étends ma gratitude aux membres distingués de mon jury. Johan Chang et Sylvie Hebert, vos éloges élevés à l'égard de ma thèse ont renforcé ma confiance dans la qualité de mon travail. Un merci spécial va également à Abhay Shukla et Stephen Rowley, qui ont gracieusement accepté le rôle d'examinateurs pour ma défense et ont fourni des informations et des suggestions précieuses.

Je tiens à exprimer mon appréciation envers tous ceux qui ont assisté à ma défense de doctorat. Votre présence a rendu l'occasion plus significative et mémorable.

Enfin, je tiens à remercier ma petite amie, Linru FANG, qui a partagé des moments inoubliables avec moi à Paris et a préparé un somptueux banquet. Je tiens également à exprimer ma gratitude envers mes amis qui non seulement m'ont offert de merveilleux cadeaux, mais ont également rempli ma vie de joie pendant mon séjour ici. À mes parents et à ma famille en Chine, votre soutien indéfectible a été une source de force tout au long de mon parcours.

Je vous remercie tous pour votre soutien constant et votre assistance. Mes meilleurs vœux vous accompagnent, à chacun d'entre vous.

Acknowledgements

First and foremost, I would like to extend my heartfelt appreciation to my supervisor, Kamran Behnia. He has been my guiding light, introducing me to the forefront of research, expanding my horizons, and providing invaluable guidance on both methodologies and critical thinking. I must also express my gratitude to my co-supervisor, Benoît Fauqué, who not only shared extensive knowledge about experimental aspects but also lent a helping hand in overcoming various life challenges. Their support and mentorship were instrumental in shaping my thesis and preparing me for the defense presentation.

Next, I extend my gratitude to the esteemed members of my jury. Johan Chang and Sylvie Hebert, your high praise for my thesis bolstered my confidence in the quality of my

work. Special thanks also go to Abhay Shukla and Stephen Rowley, who graciously accepted the role of defense examiners and provided valuable insights and suggestions.

I would like to express my appreciation to everyone who attended my Ph.D. defense. Your presence made the occasion more meaningful and memorable.

Lastly, I want to thank my girlfriend, Linru FANG, who shared unforgettable moments with me in Paris and prepared a sumptuous banquet. I also want to express my gratitude to my friends who not only provided me with wonderful gifts but also filled my life with joy during my time here. To my parents and relatives in China, your unwavering support has been a source of strength throughout my journey.

Thank you all for your unwavering support and assistance. My best wishes go out to each and every one of you.

Contents

Contents v

List of Figures ix

Introduction xi

1 Transport theory and measurement 1
- 1.1 Charge and heat transport . . . 1
  - 1.1.1 Electronic transport coefficients . . . 2
  - 1.1.2 The Wiedemann-Franz law . . . 5
  - 1.1.3 Phononic thermal conductivity . . . 6
  - 1.1.4 Transverse transport in magnetic field . . . 9
- 1.2 Experimental techniques . . . 11
  - 1.2.1 Measuring principle . . . 11
  - 1.2.2 Measurement setup . . . 13
  - 1.2.3 Measurement of voltage . . . 14
  - 1.2.4 Measurement of temperature difference . . . 15

2 Research background 19
- 2.1 Overview of $SrTiO_3$ . . . 19
  - 2.1.1 Crystal lattice properties . . . 19
    - 2.1.1.1 Antiferrodistortive Transition . . . 19
    - 2.1.1.2 Quantum paraelectricity . . . 21
    - 2.1.1.3 Ferroelectricity . . . 22
  - 2.1.2 Metallicity of doped $SrTiO_3$ . . . 24
  - 2.1.3 Lattice heat transport properties . . . 27
- 2.2 Other quantum paraelectric materias . . . 28
  - 2.2.1 Quantum paraelectric $KaTO_3$ . . . 28
  - 2.2.2 Magnetic $EuTiO_3$ . . . 28

3 Thermal Hall effect in strontium titanate 31
- 3.1 Thermal Hall Effect in metals and in insulators . . . 31
- 3.2 Origin of the thermal Hall effect in STO . . . 32
  - 3.2.1 Possible role of the AFD transition ? . . . 32
  - 3.2.2 Ferroelectric fluctuations? . . . 33
- 3.3 Samples . . . 33

3.3.1 $Sr_{1-x}Ca_xTiO_3$ . . . 34
3.3.2 $SrTiO_{3-\delta}$ preparation . . . 34
3.3.3 Thermal Hall effect in $Sr_{1-x}Ca_xTiO_3$ . . . 35
3.4 Thermal Hall effect in metallic STO . . . 36
3.4.1 Temperature dependence of κ_{xx} and κ_{xy} . . . 37
3.4.2 Field dependence of κ_{xy} . . . 37
3.4.3 Thermoelectric correction to thermal conductivity . . . 38
3.4.4 Phonon drag thermal Hall effect . . . 44
3.4.4.1 Phonon drag effect in lightly doped $SrTiO_3$ . . . 45
3.4.4.2 From Phonon drag to thermal Hall effect . . . 47
3.4.4.3 Comparison of our model with the experimental data . . . 49
3.4.5 Electron-phonon drag THE in other metallic solids . . . 51
3.5 Conclusion . . . 51

4 Electronic thermal transport in metallic STO 53
4.1 T-square resistivity in two dilute metals . . . 53
4.2 Electronic thermal conductivity in $SrTi_{1-x}Nb_xO_3$ . . . 56
4.2.1 Samples . . . 56
4.2.1.1 Resistivity and thermal conductivity . . . 56
4.2.1.2 Thermal conductivity influenced by thermoelectricity . . . 57
4.2.2 Difference of thermal conductivity in magnetic field . . . 58
4.2.3 Magnetic response on the conductivity of electrons . . . 61
4.2.4 Electronic and phononic thermal conductivity . . . 63
4.3 T-square resistivity prefactor in Nb-STO . . . 64
4.4 Comparison with ^3He . . . 65
4.5 Conclusion . . . 66

5 Thermal transport in $EuTiO_3$ 69
5.1 Motivation and samples . . . 69
5.2 Results . . . 70
5.2.1 Resistivity and Hall effect . . . 70
5.2.2 The Seebeck coefficient . . . 71
5.2.3 Resistivity hysteresis near the AFD transition . . . 72
5.2.4 Temperature dependent thermal conductivity . . . 73
5.2.5 Field dependent thermal conductivity . . . 75
5.3 Discussion . . . 75
5.3.1 Magnetization . . . 76
5.3.2 Sample dependence of thermal conductivity . . . 76
5.3.3 Glass-like thermal conductivity . . . 78
5.3.4 Specific heat . . . 79
5.3.5 Thermal diffusivity and phonon mean-free-path . . . 81
5.3.6 Discussion on glass-like thermal conductivity . . . 82
5.4 Conclusion . . . 84

Conclusion 85

Appendices **87**

A Using thermocouple measure thermal conductivity **89**

B Résumé long en français **91**
B.1 Résumé en français 91
B.2 Introduction en français 92

Bibliography **95**

List of Figures

1.1 Phonon specific heat, mean-free path, and velocity . . . 8
1.2 Sketch of transport measurement setup . . . 11
1.3 Homemade Sample holder and probe in PPMS . . . 14
1.4 Voltage measurement circuit . . . 15
1.5 Temperature measurement circuit . . . 17
1.6 Calibration curve of Cernox 1030 . . . 18

2.1 Illustration of the AFD transition in $SrTiO_3$ . . . 20
2.2 Γ_{25} soft phonon mode and second order transition at T_{AFD} . . . 21
2.3 Γ_{15} soft phonon mode and large permittivity . . . 22
2.4 Quantum paraelectric and photoelectric . . . 23
2.5 Band structure of $SrTiO_3$ . . . 24
2.6 Quantum oscillation and superconductivity . . . 25
2.7 T-square resistivity in metallic Strontium titanate . . . 26
2.8 Thermal conductivity and thermal Hall effect of $SrTiO_3$ . . . 27
2.9 Dielectric constant and soft phonon mode in $KTaO_3$ . . . 28
2.10 AFD transition in $EuTiO_3$ . . . 29
2.11 Magnetic structure and magneto-electric coupling . . . 30

3.1 Thermal Hall effect in insulators . . . 32
3.2 Thermal Hall effect in quantum paraelectric $SrTiO_3$ . . . 33
3.3 The process of preparation metallic $SrTiO_{3-\delta}$ samples. . . . 35
3.4 Carrier density of $SrTiO_{3-\delta}$ versus annealing temperature . . . 36
3.5 Electrical resistivity of $SrTiO_{3-\delta}$ samples . . . 37
3.6 $\kappa_x x$ and $\kappa_x y$ of $SrTi^{16}O_3$ and $SrTi^{18}O_3$ . . . 38
3.7 κ and κ_{xy} in $Sr_{1-x}Ca_xTiO_3$ . . . 39
3.8 κ and κ_{xy} evolve with O vacancies . . . 40
3.9 External thermal Hall signal in $SrTiO_{3-\delta}$ . . . 41
3.10 Phonon drag of seebeck effect in $SrTiO_{3-\delta}$ . . . 42
3.11 The modified κ and κ_{xy} . . . 43
3.12 The modified $\kappa_x x$ and κ_{xy} at differnet temperatures . . . 44
3.13 Electrical and thermal experiments . . . 45
3.14 Solving the transport coefficients . . . 46
3.15 Phonon-dominant κ and large Hall angle . . . 47
3.16 Phonon drag in Seebeck and Nernest effect . . . 47
3.17 From phonon drag to thermal Hall conductivity . . . 49

3.18 Quantitative analysis of $\Delta\kappa_{xy}$ 50

4.1 T-square resistivity in Fermi liquids 55
4.2 Electrical resistivity and thermal conductivity in $SrTi_{1-x}Nb_xO_3$ 56
4.3 Seebeck effect and the component of thermal conductivity 57
4.4 Thermal conductivity in Nb-doped $SrTiO_3$ 58
4.5 Longitudinal and Hall conductivity 59
4.6 Hall angle 60
4.7 Field dependence of the electric and thermal conductivity 61
4.8 Field dependence of the electric and thermal conductivity 62
4.9 Electron and phonon contributions to the thermal conductivity 63
4.10 Electronic thermal resistivity 64

5.1 Electrical resistivity and activation gap of $EuTiO_3$ 70
5.2 Hall effect and carrier concentration of $EuTiO_3$ 71
5.3 Temperature dependence of Seebeck coefficient S 72
5.4 Hysteresis of temperature-dependent resistivity 73
5.5 Thermal conductivity κ of $EuTiO_3$ and $SrTiO_3$ 74
5.6 Longitudinal thermal conductivity κ_{xx} in magnetic field 75
5.7 Magnetization of $EuTiO_3$ 77
5.8 Sample difference of thermal conductivity κ and magnetization M 78
5.9 Comparison with crystals, glasses and glass-like crystals 79
5.10 Thermal conductivity of three quantum para-electric solids 80
5.11 Specific heat in three quantum paraelectric solids 81
5.12 Thermal Diffusivity of $EuTiO_3$ and the mean-free-path of phonons 82
5.13 Crystal structure of $EuTiO_3$ in its paramagnetic phase 83

A.1 Using thermocouple measure thermal conductivity 89

Introduction

When a system is forced out of equilibrium, it will tend to recover to the equilibrium state. This is the case in transport phenomena. In solids, the potential difference leads the electron to move from the high electrical potential side to the low side, and the temperature difference will lead to heat flow from the hotter to the colder parts. These two phenomena are called electrical and thermal transport. In condensed matter physics, the electrical and thermal transport in solids usually participated by electrons and phonons can be described by the Boltzmann transport equation in a semi-classic picture. Nevertheless, the interplay of both types of quasiparticles can give rise to emergent properties such as superconductivity or phonon drag effect that is worth studying. This is the case in the perovskite strontium titanate ($SrTiO_3$) and its sister Europium titanate ($EuTiO_3$) that have attracted much attention recently.

The perovskite strontium titanate ($SrTiO_3$) has been known for a long time. It is a quantum paraelectric: The ferroelectric instability is suppressed due to quantum fluctuations [1]. The ferroelectric order can be stabilized by tiny chemical substitution (either by replacing Sr with Ca [2] or Ba [3], or by substituting ^{16}O with ^{18}O [4]). Pristine $SrTiO_3$ is an insulator with a large band gap but it can easily be turned into metal by introducing a tiny concentration of dopants (O vacancies, Nb, or La doping) due to its large permittivity [5]. This metal has a dilute superconducting ground state [5; 6].

The subject of this thesis is thermal transport in two quantum paralectric materials. It consists of a study of the evolution of thermal transport with atomic substitution in $SrTiO_3$ as well as a first study of thermal transport in $EuTiO_3$, a closely related material with the peculiarity of being magnetically ordered. The thesis is divided into three parts.

The first part is devoted to the thermal Hall effect (THE) in $SrTiO_3$ and its variation with atomic substitution. THE is the thermal analog of the electrical Hall effect. Instead of a transverse voltage induced by a perpendicular magnetic field in the presence of an electric current, a transverse temperature difference is generated in the presence of a heat current. In metals, the existence of such an effect is not surprising, because charged heat carriers are influenced by the Lorentz force. This is an electronic thermal Hall effect linked to the electrical Hall effect by the Wiedemann-Franz law. On the other hand, the presence of such an effect in insulators is not understood.

Phonon THE was first observed in the paramagnetic insulator $Tb_3Ga_5O_{12}$ [7; 8] and attributed to skew scattering of phonons by superstoichiometric Tb magnetic impurities. Successively, it was also found in nonmagnetic materials (such as $SrTiO_3$ [9]), where the phononic origin of THE is uncontested. Numerous theoretical scenarios [10–13] were proposed to explain how phonons can generate a THE. They can be broadly classified as either intrinsic (invoking the peculiarities of the phonon spectrum) or extrinsic (referring to con-

sequences of specific phonon scattering mechanisms). Up to now, the origin of the phonon THE is still an open question.

Continuing previous studies on $SrTiO_3$, I measured for the first time the thermal Hall effect in Ca-substituted and oxygen-reduced samples of $SrTiO_3$. This study found that Ca substitution, which stabilizes the ferroelectric order, drastically reduces THE, implying that the ferroelectric order is detrimental to the THE. On the other hand, I found that in oxygen-reduced samples THE is larger than in pristine STO. Surprisingly, in the dilute metallic STO, the amplitude of THE exceeds the sum of the [expected] electronic and the phononic contributions. We argued that this can be understood by invoking the drag between electrons and phonons. In our temperature range of interest, heat is almost exclusively carried by phonons, but the electronic Hall angle is much higher than the phonon Hall angle. The combination of these two features with frequent momentum exchange between phonons and electrons can be an additional source of THE. This is the first time that signatures of phonon drag have been observed by a purely thermal (and not thermoelectric) probe.

The second part is a contribution to the ongoing debate on the origin of quadratic temperature-dependent resistivity in dilute metals. In Fermi liquids, the collision between electrons is known to generate a contribution to electrical resistivity growing with the square of the temperature. This corresponds to the temperature dependence of the phase space for electron-electron scattering. Both electrons participating in a collision reside within a thermal window of the Fermi level. Therefore, the Pauli exclusion principle is applied twice, and hence a quadratic temperature dependence. However, the microscopic source of dissipation is not straightforward. To explain how electron–electron collisions lead to momentum leaks, two scenarios have been proposed. The first invokes Umklapp events [14; 15]. These are collisions in which the sum of the two colliding wave vectors becomes larger than the width of the Brillouin zone[16; 17]. A second scenario invokes multiple electron reservoirs. In this context, the observation of T-square resistivity in two dilute metals, namely $SrTiO_3$ and Bi_2O_2Se are enigmatic. Indeed, neither of these two scenarios is relevant in these cases. In the case of $SrTiO_3$, it has been proposed that T-square scattering may be caused by the scattering of electrons by two soft optical phonons[18; 19]. This scenario does not apply to Bi_2O_2Se [20].

The subject of the second part of my thesis is the thermal counterpart of T-square electrical resistivity in dilute metallic $SrTiO_3$. I have studied the electronic thermal conductivity of metallic Nb-doped STO at two carrier concentrations. Despite the dominance of the lattice component of thermal conductivity, we succeeded in extracting the electronic contribution to heat transport by exploiting the differentiating effect of the magnetic field on phonons and electrons. We found that thermal resistivity WT ($W = \kappa^{-1}$) follows T-square behavior and its prefactor is larger than its electric counterpart by a factor of ~ 3. This is incompatible with what is expected in the phonon-based scenario in which quasi-elastic scattering should lead a perfect equality between the two prefactors. Thus the T-square resistivity of Nb-doped STO cannot be distinguished from other metals in which the e-e origin of the T-square resistivity is uncontested. This leads us to conclude that T-square (electric and thermal) resistivity can be caused without Umklapp as a consequence of the T-square decrease in the amplitude of the (momentum and energy) diffusivity in a Fermi liquid caused by fermion-fermion scattering. A comprehensive theory of this phenomenon is yet to be elaborated.

In the third part, the focus of attention is another quantum paraelectric, $EuTiO_3$. Like

$SrTiO_3$, $EuTiO_3$ has a cubic structure at room temperature and goes also through an antiferrodistortive transition where adjacent TiO_6 octahedra rotate in opposite directions. Like $SrTiO_3$, it shows a quantum paraelectric behavior, but in a much more attenuated way[21]: Its dielectric constant saturates to 300, compared to 20000 in $SrTiO_3$. Eu $f-$electrons of order antiferromagnetically below $T_N = 5.5K$ [21]. Interestingly, the dielectric constant shows a cusp at this temperature. This magneto-electric coupling [22] has been a subject of theoretical and experimental research.

We studied the electric, thermoelectric, and thermal transport properties of $EuTiO_3$. The temperature dependence of electric resistivity and the Seebeck coefficient allowed us to conclude that the insulating band gap is $\sim$0.22 eV. Moreover, the thermal conductivity of $EuTiO_3$ is drastically reduced and has an amplitude and temperature dependence akin to amorphous silica. A comparison with other quantum paraelectric solids, namely $SrTiO_3$ and $KTaO_3$, shows that $4f$ spins at Eu^{2+} sites drastically impede heat transport by phonons well above the magnetic ordering temperature. This result provides a new challenge for the theory attempting to achieve a unified picture of thermal transport in crystals and glasses.

The three sets of results are detailed in chapters three to five of this manuscript. The first chapter will give an overview of transport theory and experimental techniques. The second chapter is an overview of the research background introducing the quantum paraelectric materials.

Chapter 1

Transport theory and measurement

Summary of the Chapter

Charge and thermal energy can travel in solids. The former is carried by charge carriers: electrons and holes. The latter can be also carried by neutral excitations such as lattice waves (phonons), electromagnetic waves, or spin waves. In this chapter, we discuss transport by electrons and phonons. Starting from the simple kinetic theory, we will introduce transport coefficients (electrical, thermal, and thermoelectric) and transport equations. Then, using the semi-classic Boltzmann equation, we will derive expressions for these coefficients. In the presence of a magnetic field, these coefficients have off-diagonal components. In the second part of the chapter, we will introduce the experimental methods employed in this thesis to extract the electrical, thermal, and thermoelectric conductivity coefficients and their off-diagonal components.

1.1 Charge and heat transport

Charge and heat can pass through solids, the former requires mobile electrons. Imposing an electric field along the solid will generate a charge flow and vice versa. The relation between the amplitude of the electric field $\vec{E}$ and charge flux density $\vec{J^e}$ (the number of electrons traveling through a given cross-section per second) is expressed by Ohm's law:

$$J^e = \sigma E \tag{1.1}$$ eq1.1

Here σ is the electrical conductivity. In the Drude picture, the electrons are treated as classical objects that suffer collisions with a characteristic time τ, the relaxation time. Within this simple approximation, the electrical conductivity is :

$$\sigma = ne\mu = \frac{ne^2\tau}{m} \tag{1.2}$$ eq1.2

where μ is mobility, n is the carrier density and m is mass of electron.

In the case of heat transport, applying a temperature gradient along the solid will produce a heat flow and vice versa. The relation between the amplitude of heat flux $\vec{J^Q}$ (the flow

of energy passing through a given cross-section per second) and temperature gradient $\vec{\nabla}T$ is expressed by Fourier's law:

$$J^Q = -\kappa \nabla T \tag{1.3}$$ eq1.3

here κ is the thermal conductivity. In the kinetic theory of gases [23], each heat carrier has a heat capacity of c. The rate of energy (E) change is equal to $\frac{\partial E}{\partial t} = c\vec{v} \cdot \vec{\nabla}T$ where v is the particle velocity. Introducing τ as the time between two collisions, the heat flux becomes $\vec{J^Q} = -nc\tau\langle \vec{v} \cdot \vec{v} \rangle \vec{\nabla}T$ where n is the carrier density. In the case of three dimensions, $\langle \vec{v} \cdot \vec{v} \rangle = \frac{1}{3}v^2$. This leads to the following expression for κ :

$$\kappa = \frac{1}{3}C\tau v^2 = \frac{1}{3}Cvl \tag{1.4}$$ eq1.4

where l is the mean free path ($l = v\tau$) and C is the total heat capacity per volume: nc. Eq. 1.4 is true for all quasi-particles, including electrons and phonons (or even magnons in magnetic materials). Here, we only care about electrons and phonons.

Carriers of electric charge can transport momentum and heat energy. Therefore, the two quantities can become entangled. This is known as the thermoelectric phenomenon (interconversion of the temperature difference and electric voltage). Eq. 1.1 and 1.3 have thus to be modified [24; 25] as follow :

$$J^e = \sigma E - \alpha \nabla T \tag{1.5}$$ eq1.5

$$J^Q = \beta E - \kappa \nabla T \tag{1.6}$$ eq1.6

where α is the thermoelectric conductivity, β is the electro-thermal conductivity. Both quantities are linked through the Kelvin relation: $\beta = \alpha T$.

After introducing these three transport coefficients, σ, κ, and α. Let us now introduce the Boltzmann equation that provides a mathematical way to calculate them and a microscopic insight into their amplitudes [24].

1.1.1 Electronic transport coefficients

The central concept of the Boltzmann approach is the distribution function $f_k(\vec{r})$ representing the probability of electron with wave vector $\vec{k}$ found at the position $\vec{r}$. An electric field or a temperature gradient can create variations in the magnitude of $f_k(\vec{r})$.

The travel of an electron with a charge of e and wave vector $\vec{k}$ can generate a flow of electric current equal to $e\vec{v}_k f_k$, so the total current flow (charge flux) is obtained by integrating over all wave-vectors $\vec{k}$:

$$J^e = \int e\vec{v}_k f_k d\vec{k} \tag{1.7}$$ eq1.7

here e and $\vec{v}_k$ are the electron charge and the electron velocity.

There is a corresponding expression for the energy flux. Since the thermal energy of each traveling electron is $\epsilon_k - \mu$ (ϵ_k is electron energy and μ is chemical potential), the heat flux is represented by the following integral:

$$J^Q = \int \vec{v}_k(\epsilon_k - \mu) f_k d\vec{k} \tag{1.8}$$ eq1.8

In the absence of electrical or heat current the probability distribution function $f_k(\vec{r})$ obeys the Fermi-Dirac distribution:

$$f^0 = \frac{1}{e^{\frac{\epsilon_k - \mu}{k_B T}} + 1} \tag{1.9}$$ eq1.9

where ϵ_k and μ are the energy of the electron and the chemical potential. k_B is Boltzmann constant and T is temperature. In the linear response approximation the time differential of $f_k(\vec{r})$ becomes

$$\frac{df_k(\vec{r})}{dt} = -\frac{f_k(\vec{r}) - f^0}{\tau} \tag{1.10}$$ eq1.10

where τ is the relaxation time.

In presence of electric field $\vec{E}$, the time differential of $f_k(\vec{r})$ in Eq.1.10 becomes

$$\frac{df_k(\vec{r})}{dt}|_{\vec{E}} = \frac{\partial f_k(\vec{r})}{\partial \epsilon_k}\frac{\partial \epsilon_k}{\partial \vec{k}}\frac{\partial \vec{k}}{\partial t} = \frac{\partial f_k(\vec{r})}{\partial \epsilon_k}\hbar\vec{v}_k\frac{e\vec{E}}{\hbar} \approx \frac{\partial f^0}{\partial \epsilon_k}\vec{v}_k e\vec{E} \tag{1.11}$$ eq1.11

Note that we introduced the group velocity of an electron, $\vec{v}_k$, which is equal to $\frac{1}{\hbar}\frac{\partial \epsilon_k}{\partial \vec{k}}$ [26] (where $\hbar$ is Planck constant) and that according to the conservation of momentum $\frac{\partial \vec{k}}{\partial t} = \frac{e\vec{E}}{\hbar}$.

In presence of a temperature gradient $\vec{\nabla}T$, the time differential of $f_k(\vec{r})$ becomes :

$$\frac{df_k(\vec{r})}{dt}|_{\vec{\nabla}T} = \frac{\partial f_k(\vec{r})}{\partial T}\frac{\partial T}{\partial \vec{r}}\frac{\partial \vec{r}}{\partial t} = \frac{\partial f_k(\vec{r})}{\partial T}\vec{v}_k\vec{\nabla}T \approx \frac{\partial f^0}{\partial T}\vec{v}_k\vec{\nabla}T \tag{1.12}$$ eq1.12

Combining Eq. 1.11, Eq. 1.12, and Eq. 1.10, the probability distribution function $f_k(\vec{r})$, in presence of electric field $\vec{E}$ and temperature gradient $\vec{\nabla}T$, becomes

$$f_k(\vec{r}) = f^0 - \tau\vec{v}_k(\frac{\partial f^0}{\partial \epsilon_k}e\vec{E} + \frac{\partial f^0}{\partial T}\vec{\nabla}T) \tag{1.13}$$ eq1.13

which can be simplified to

$$f_k(\vec{r}) = f^0 - \tau\vec{v}_k(\frac{\partial f^0}{\partial \epsilon_k}e\vec{E} + \frac{\partial f^0}{\partial \epsilon_k}\frac{\epsilon_k - \mu}{T}\vec{\nabla}T) \tag{1.14}$$ eq1.14

by assuming that : $\frac{\partial f^0}{\partial T} = -\frac{\partial f^0}{\partial \epsilon_k}\frac{\epsilon_k - \mu}{T}$

On the basis of Eq.1.14, we can now evaluate the charge (J^e) and heat (J^Q) current densities :

$$J^e = -\int e\vec{v}_k\tau\vec{v}_k(\frac{\partial f^0}{\partial \epsilon_k}e\vec{E} + \frac{\partial f^0}{\partial \epsilon_k}\frac{\epsilon_k - \mu}{T}(-\vec{\nabla}T))d\vec{k} \tag{1.15}$$ eq1.15

$$J^Q = -\int \vec{v}_k(\epsilon_k - \mu)\tau\vec{v}_k(\frac{\partial f^0}{\partial \epsilon_k}e\vec{E} + \frac{\partial f^0}{\partial \epsilon_k}\frac{\epsilon_k - \mu}{T}(-\vec{\nabla}T))d\vec{k} \tag{1.16}$$ eq1.16

In the steady-state situation, the average velocity is zero. Therefore, the integral of the first term of Eq. 1.14 is omitted as shown in Eq. 1.15 and Eq. 1.16. Comparing Eq. 1.15, Eq. 1.16 with Eq. 1.5 and Eq. 1.6, we can get the three transport coefficients:

$$\sigma = -e^2 \int v_k^2 \tau \frac{\partial f^0}{\partial \epsilon_k} d\vec{k} \tag{1.17}$$ eq1.17

$$\alpha = -ek_B \int v_k^2 \tau \frac{\partial f^0}{\partial \epsilon_k} \frac{\epsilon_k - \mu}{k_B T} d\vec{k} \tag{1.18}$$ eq1.18

$$\kappa = -k_B^2 T \int v_k^2 \tau \frac{\partial f^0}{\partial \epsilon_k} (\frac{\epsilon_k - \mu}{k_B T})^2 d\vec{k} \tag{1.19}$$ eq1.19

Let us make a last step to reach the final expressions of σ, α and κ. We introduce the function $\Xi(\epsilon)$:

$$\Xi(\epsilon) = \frac{h}{2} \int v_k^2 \tau(k) \delta(\epsilon - \epsilon(k)) dk^3 \tag{1.20}$$ eq1.20

where $\delta(\epsilon - \epsilon(k))$ is delta function. Assuming that $\epsilon(k)$ is a smooth function of the wave-vector $\vec{k}$ and presents no singularity, Eq. 1.20 can be written as

$$\Xi(\epsilon) = \frac{h}{2} v_k^2 \tau(k) N(\epsilon) \tag{1.21}$$ eq1.21

$N(\epsilon)$ is the density of states and $N(\epsilon)d\epsilon = dk^3$. Introducing $\Xi(\epsilon)$ into Eq. 1.17 1.18 and 1.19, we get :

$$\sigma = -2\frac{e^2}{h} \int \Xi(\epsilon) \frac{\partial f^0}{\partial \epsilon} d\epsilon \tag{1.22}$$ eq1.22

$$\alpha = -2\frac{ek_B}{h} \int \Xi(\epsilon) \frac{\partial f^0}{\partial \epsilon} \frac{\epsilon_k - \mu}{k_B T} d\epsilon \tag{1.23}$$ eq1.23

$$\kappa = -2\frac{k_B^2}{h} T \int \Xi(\epsilon) \frac{\partial f^0}{\partial \epsilon} (\frac{\epsilon_k - \mu}{k_B T})^2 d\epsilon \tag{1.24}$$ eq1.24

Using the Sommerfeld expansion [27], we can develop the integrals in powers series of $k_B T$ as follows:

$$\sigma = 2\frac{e^2}{h} [\Xi(\epsilon_F) + ...] \tag{1.25}$$ eq1.25

$$\alpha = 2\frac{\pi^2}{3} \frac{ek_B}{h} k_B T [\frac{\partial \Xi(\epsilon_F)}{\partial \epsilon} + ...] \tag{1.26}$$ eq1.26

$$\kappa = 2\frac{\pi^2}{3}\frac{k_B^2}{h}T[\Xi(\epsilon_F) + ...] \tag{1.27}$$ eq1.27

For a three-dimensional free electrons gas, the Fermi energy is $\epsilon_F = \frac{\hbar^2}{2m}(3\pi^2 n)^{\frac{2}{3}}$, the density of states is equal to $N(\epsilon_F) = \frac{3}{2}\frac{n}{\epsilon_F}$ and the electron specific heat $C = \frac{\pi^2}{3}N(\epsilon_F)k_B^2 T$ [27]. Introducing them in Eq. 1.25 and 1.26, they become that

$$\sigma \approx e^2 \cdot \frac{1}{3}v_k^2\tau(k)N(\epsilon) = \frac{ne^2\tau}{m} \tag{1.28}$$ eq1.28

$$\kappa \approx \frac{\pi^2}{3}k_B^2 T \cdot \frac{1}{3}v_k^2\tau(k)N(\epsilon) = \frac{1}{3}Cvl \tag{1.29}$$ eq1.29

We note that Eq.1.28 and 1.29 are closely related to the expression of the electric conductivity in the Drude model and of the thermal conductivity in the kinetic theory.

1.1.2 The Wiedemann-Franz law

An important consequence of Eq. 1.28 and Eq. 1.29 is that the ratio of thermal to electric conductivity is constant :

$$\frac{\kappa}{\sigma} = \frac{\pi^2}{3}\frac{k_B^2}{e^2}T = L_0 T \tag{1.30}$$ eq1.30

where L_0 is the Lorenz number equal to $2.4453 \times 10^{-8} W\Omega K^{-2}$ which only set by the two fundamental constant k_B and e. This result is known as the Wiedemann-Franz (WF) law discovered in 1853 [28].

One important hypothesis in the derivation of the WF law from the Boltzmann equation is that the scattering events affect the electrical and thermal conductivity in the same way. We used the same relaxation time τ in both Eq. 1.15 and Eq. 1.16). It is only true in the zero temperature limit where elastic scattering is the dominant one. At finite temperature, inelastic scattering events also exist and can give rise to the deviation of the WF law [27; 29; 30].

In solids, two well-known inelastic scattering events can give rise to a deviation from the WF law. First, the electron-electron scattering where the relaxation rate $(1/\tau)$ presents a characteristic T^2 dependence. Both participating electrons reside within a thermal window of the Fermi level, and the leak of momentum during the electron-electron collision can be interpreted by two mechanisms: Umklapp events [14; 31] or multiple electron reservoirs [16; 17] (it's not the case for dilute metal $SrTiO_3$ [32] and Bi_2O_2Se [20] and we will discuss in chapter 4). These lead to an electrical resistivity ($\rho = \sigma^{-1}$) behavior, at low temperature, of the form

$$\rho = \rho_0 + AT^2 \tag{1.31}$$ eq1.31

where ρ_0 is the residual resistance (associated with elastic scattering) and A the prefactor that sets the amplitude of the T^2-therm in ρ. This type of behavior is usually taken as

a hallmark of Fermi liquids (another one is T-linear specific heat). Like in the electrical resistivity, the electron-electron scattering also gives rise to a T^2 in the thermal resistivity ($W = \kappa^{-1}$) :

$$WT = W_0 T + BT^2 \tag{1.32}$$ eq1.32

At $T = 0$, electrons only undergo scattering events with impurities or boundaries of the system: these collisions are elastic and thus the WF law is satisfied that $\rho_0 = L_0 W_0 T$. However, the electron-electron contribution inelastic differs and leads to $L_0 B > A$ so that a deviation of the WF is found at finite temperatures. In Chapter 4 , I will discuss such deviation in the context of electron-doped $SrTiO_3$.

A second source of scattering that also leads to a finite temperature deviation of WF law is the electron-phonon scattering [29]. In contrast to the case of electron-electron scattering, the power law contribution of such scattering will be different in the electrical and thermal conductivity. At low temperatures when $T \ll \theta_D$, where θ_D is Debye temperature, $\rho_{e-ph} \propto T^5$ while the electronic thermal resistivity times by temperature $W_{e-ph} T \propto T^3$ that leads to another source of invalidation of WF law. At high temperatures ($T \gg \theta_D$), the electron-phonon scattering becomes elastic scattering, the WF law recovers and the resistivity becomes T-linear (ρ_{e-ph} and $W_{e-ph} T \propto T$). This is why the WF law has been first discovered at room temperature.

1.1.3 Phononic thermal conductivity

In addition to the charge carriers, there is another type of entropy carrier in solids, namely the phonons. In solids, atoms vibrate around their equilibrium positions. The crystal lattice vibration can be characterized by standing waves. The quanta of the crystal vibrational field are referred to as phonons.

Solids usually have two types of phonons: low-frequency acoustic phonons (characterized by a vanishing dispersion at the center of the Brillouin zone) and high-frequency optical phonons. The low-temperature thermal conductivity is generally dominated by the acoustic phonons however the optical phonons can also contribute to κ as they interact with the acoustic phonon.

Let's now derive the phonon contribution to thermal conductivity. In equilibrium, the phonon distribution function obeys the Bose-Einstein distribution:

$$N^0 = \frac{1}{e^{\frac{\hbar\omega_{\vec{q}}}{k_B T}} - 1} \tag{1.33}$$ eq1.33

where $\vec{q}$ and $\omega_{\vec{q}}$ are the phonon wave vector and frequency. Compared with electrons in Eq.1.10 1.12 and 1.13, the phonon distribution function in the presence of temperature gradient becomes

$$N_{\vec{q}} = N^0 - \tau_{\vec{q}} \vec{v}_{\vec{q}} \frac{\partial N^0}{\partial T} \vec{\nabla} T \tag{1.34}$$ eq1.34

where the $\vec{v}_{\vec{q}}$ is phonon group velocity, $\tau_{\vec{q}}$ is the phonon scattering relaxation time. The heat flux carried by all phonon modes is then given by :

$$J^Q = -\frac{1}{3} \sum_{\vec{q}} \hbar\omega_{\vec{q}} \tau_{\vec{q}} \vec{v}_{\vec{q}}^2 \frac{\partial N^0}{\partial T} \vec{\nabla} T \tag{1.35}$$ eq1.35

and thus the phonon thermal conductivity is equal to :

$$\kappa_{ph} = -\frac{1}{3}\sum_{\vec{q}} \hbar\omega_{\vec{q}}\tau_{\vec{q}}\vec{v}_{\vec{q}}^2\frac{\partial N^0}{\partial T} \tag{1.36}$$ eq1.36

According to the Debye theory [33], $v_{\vec{q}}$ is replaced by the average phonon velocity v (approximately equal to the velocity of sound in solids) and $\omega = v \cdot q$ (the dispersion relation of acoustic phonon mode) for all types of phonons. Eq.1.35 become an integral :

$$\kappa_{ph} = \frac{1}{3}\int \hbar\omega_{\vec{q}}\tau_{\vec{q}}\vec{v}_{\vec{q}}^2\frac{\partial N^0}{\partial T}d\vec{q} \tag{1.37}$$ eq1.37

here $d\vec{q} = \frac{3q^2}{2\pi^2}dq = \frac{3\omega^2}{2\pi^2 v^3}d\omega$ [34]. Using the Debye assumptions and Eq.1.32 and 1.36 it leads to

$$\kappa_{ph} = \frac{1}{2\pi^2 v}\int_0^{\omega_D} \hbar\omega^3\tau_q(\omega)\vec{v}_{\vec{q}}^2\frac{\hbar\omega}{K_B T^2}\frac{e^{\frac{\hbar\omega}{K_B T}}}{(e^{\frac{\hbar\omega}{K_B T}}-1)^2}d\omega \tag{1.38}$$ eq1.38

where ω_D is the Debye frequency that satisfies :

$$3N = \int_0^{\omega_D}\frac{3\omega^2}{2\pi^2 v^3}d\omega \tag{1.39}$$ eq1.39

where $3N$ is the total number of all distinguishable phonon modes. If we make the substitution $x = \frac{\hbar\omega}{k_B T}$ and define the Debye temperature $\theta_D = \frac{\hbar\omega_D}{k_B}$, Eq. 1.37 can be simplified to

$$\kappa_{ph} = \frac{k_B}{2\pi^2 v}(\frac{k_B}{\hbar})^3 T^3\int_0^{\frac{\theta_D}{T}}\tau_q(x)\frac{x^4 e^4}{(e^x-1)^2}dx \tag{1.40}$$ eq1.40

Within the Debye approximation, the lattice-specific heat is

$$C_V = \frac{3k_B}{2\pi^2 v^3}(\frac{k_B}{\hbar})^3 T^3\int_0^{\frac{\theta_D}{T}}\frac{x^4 e^4}{(e^x-1)^2}dx \tag{1.41}$$ eq1.41

The phonon mean free path $l = v\tau$ and then phonon thermal conductivity can be written as[34]

$$\kappa_{ph} = \frac{1}{3}\int_0^{\frac{\theta_D}{T}} C(x)vl(x)dx \tag{1.42}$$ eq1.42

We note that this last equation is also analogous to the thermal conductivity formula derived from simple kinetic theory.

According to Eq. 1.42, the phonon thermal conductivity is the product of the phonon heat capacity, phonon mean free path and sound velocity. Fig 1.1 shows the typical temperature dependence of these three quantities that allow a qualitative understanding of the typical temperature dependence of the thermal conductivity of insulating materials such as the one of $SrTiO_3$, see Fig 2.8 (a).

At sufficiently low temperatures, when $T \ll \theta_D$, the heat capacity behaves as $C \propto T^3$, the mean-free-path l of the phonons becomes comparable with the sample size as the low

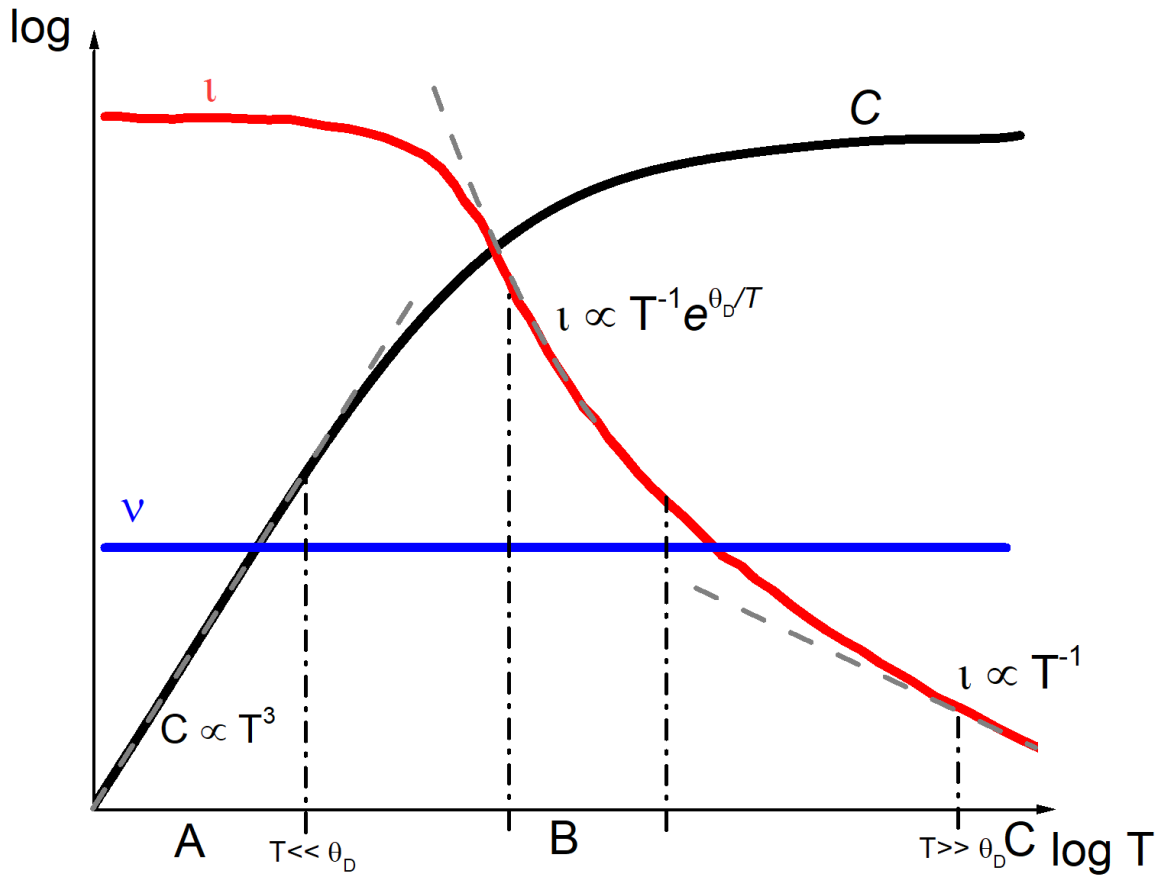

Fig. 1.1 *Schematic sketch of the temperature dependence of the specific heat (C), the mean free path (ℓ), and the velocity (v) of phonons. According to Eq. 1.42, the phonon thermal conductivity is the product of these three quantities. Regions A, B, and C correspond respectively to the ballistic, Ziman, and diffusive regimes phonons.*

fig1.1

energy acoustic phonons are only scatters by the sample boundaries. These lead to a T-cube thermal conductivity κ, this is the so-called ballistic regime (region A in Fig 1.1).

As temperature increases, the phonon-phonon scattering becomes more and more important. When the temperature is large enough to allow Umklapp scattering the scattering time trace as $\tau \propto T^{-1}e^{\theta_D/T}$[35] ($l = v\tau$). Combined with the T dependence of the heat capacity, the phonon thermal conductivity κ evolves as $\kappa \propto e^{\theta_D/aT}$. This is the Ziman regime [29] (region B Fig 1.1). As temperature increases to $T \gg \theta_D$, the heat capacity becomes saturated, and the mean free path traces as T^{-1} because of the dominance of Umklapp scattering. These lead to a T^{-1} thermal conductivity, the so-called diffusive or kinetic regime (region C in Fig 1.1).

Between the ballistic and Ziman regimes another regime can be found dominated by the normal phonon-phonon scattering known as the hydrodynamic regime[36], where κ is faster than T^3 κ. It has been found in many handful systems: ^{3}He[37], Bi[38], solid H[39], $SrTiO_3$[40](Fig 1.1) and Black P[41]. I will come back to this peculiar regime in Chapter 2.

1.1.4 Transverse transport in magnetic field

In this section, we will add another parameter to the study of the electrical, thermal, and thermoelectric transport properties: a magnetic field. In the presence of a magnetic field, the charge carriers experience an additional force : the Lorenz force $e\vec{v} \times \vec{B}$ that will affect the dynamic of the electron momentum as follows $\hbar\frac{d\vec{k}}{dt} = e\vec{v_k} \times \vec{B}$. The distribution function in the presence of a magnetic field can be rewritten as :

$$\hbar\frac{df_k(\vec{r})}{dt} \mid_{\vec{B}} = \hbar\frac{df_k(\vec{r})}{d\vec{k}}\frac{d\vec{k}}{dt} = e(\vec{v_k} \times \vec{B})\frac{df_k(\vec{r})}{d\vec{k}} \tag{1.43}$$ eq1.43

In the presence of a magnetic field, we recall the electric field affects the distribution function. Suppose that the actual distribution is only barely different from the original Fermi-Dirac distribution, one can write

$$f_k(\vec{r}) = f_k^0(\vec{r}) + g_k(\vec{r}) \tag{1.44}$$ eq1.44

here $e(\vec{v_k}\times\vec{B})\frac{df_k^0(\vec{r})}{d\vec{k}} = e(\vec{v_k}\times\vec{B})\cdot\hbar\vec{v_k}\frac{df_k^0(\vec{r})}{d\epsilon_k} = 0$ (this is only true when the Landau quantization is negligible). In other words, a lonely magnetic field does not disturb the Fermi-Dirac distribution. It only works on those electrons that are kicked out of equilibrium by an electric field or a thermal gradient [24].

Considering the electric field $\vec{E}$, temperature gradient $\vec{\nabla}T$, and magnetic field $\vec{B}$ at the same time, Using the linear perturbation same as Eq. 1.10 that $\frac{df_k(\vec{r})}{dt} = -\frac{g_k(\vec{r})}{\tau}$ and combining the Eq. 1.11, Eq. 1.12 and Eq. 1.43, then we get

$$\frac{df_k(\vec{r})}{dt} = \frac{e}{\hbar}(\vec{v_k} \times \vec{B})\frac{\partial g_k(\vec{r})}{\partial\vec{k}} + \frac{\partial f^0}{\partial\epsilon_k}\vec{v}_k e\vec{E} + \frac{\partial f^0}{\partial T}\vec{v}_k\vec{\nabla}T = -\frac{g_k(\vec{r})}{\tau} \tag{1.45}$$ eq1.45

We introduce mobility $\mu = \frac{e\tau}{m} = \frac{e\tau}{\hbar}\frac{\partial v}{\partial k}$, Eq 1.45 becomes

$$\begin{aligned} g_k(\vec{r}) &= -\mu(\vec{v_k} \times \vec{B})\frac{\partial g_k(\vec{r})}{\partial\vec{v}} - e\tau\frac{\partial f^0}{\partial\epsilon_k}\vec{v}_k\vec{E} - \tau\frac{\partial f^0}{\partial T}\vec{v}_k\vec{\nabla}T \\ &= -\vec{v_k}\cdot(\mu\vec{B} \times \frac{\partial g_k(\vec{r})}{\partial\vec{v}} + e\tau\frac{\partial f^0}{\partial\epsilon_k}\vec{E} + \tau\frac{\partial f^0}{\partial T}\vec{\nabla}T) \end{aligned} \tag{1.46}$$ eq1.46

here using the scalar triple product of three vectors that $\vec{a}\cdot(\vec{b}\times\vec{c}) = \vec{b}\cdot(\vec{c}\times\vec{a})$.

Defining the $g_k(\vec{r}) = \vec{v_k}\cdot\vec{G}$ and in absence of magnetic field, $\vec{G}$ becomes $\vec{G_0} = -e\tau\frac{\partial f^0}{\partial\epsilon_k}\vec{E} - \tau\frac{\partial f^0}{\partial T}\vec{\nabla}T$. Assuming that $\vec{G}$ is independent of velocity $\vec{v_k}$ ($\frac{\partial g_k(\vec{r})}{\partial\vec{v}} = \vec{G}$), so $\vec{G} = \vec{G_0} + \mu\vec{B}\times\vec{G}$. Then we get

$$\vec{G}\times\mu\vec{B} = (\vec{G_0} + \mu\vec{B}\times\vec{G})\times\mu\vec{B} \tag{1.47}$$ eq1.47

Then replacing the left-hand side of Eq. 1.46 by $\vec{G_0} - \vec{G}$ and using a simple rule of vector algebra ($\vec{a}\times(\vec{b}\times\vec{c}) = (\vec{a}\cdot\vec{c})\vec{b} - (\vec{a}\cdot\vec{b})\vec{c}$), then it becomes

$$\vec{G_0} - \vec{G} = \vec{G_0}\times\mu\vec{B} + \mu^2B^2\vec{G} - \mu^2(\vec{B}\cdot\vec{G})\vec{B} \tag{1.48}$$ eq1.48

$$\vec{G} = \frac{\vec{G_0} - \vec{G_0} \times \mu\vec{B} + \mu^2(\vec{B} \cdot \vec{G})\vec{B}}{1 + \mu^2 B^2} \tag{1.49}$$ eq1.49

Then using $\vec{B} \cdot \vec{G} = \vec{B} \cdot \vec{G_0}$, eventually we get

$$\begin{aligned} g_k(\vec{r}) = -\tau e \frac{\partial f^0}{\partial \epsilon_k} \vec{v_k} \cdot \frac{\vec{E} - \vec{E} \times \mu\vec{B} + \mu^2(\vec{B} \cdot \vec{E})\vec{B}}{1 + \mu^2 B^2} - \\ \tau e \frac{\partial f^0}{\partial T} \vec{v_k} \cdot \frac{\vec{\nabla} T - \vec{\nabla} T \times \mu\vec{B} + \mu^2(\vec{B} \cdot \vec{\nabla} T)\vec{B}}{1 + \mu^2 B^2} \end{aligned} \tag{1.50}$$ eq1.50

Assuming that the electric field and thermal gradient are parallel and perpendicular to the magnetic field, the electrical and heat current can be written as :

$$J^e = -\int e\vec{v}_k \tau \vec{v}_k \left(\frac{\partial f^0}{\partial \epsilon_k} e \frac{\vec{E} - \vec{E} \times \mu\vec{B}}{1 + \mu^2 B^2} + \frac{\partial f^0}{\partial \epsilon_k} \frac{\epsilon_k - \mu}{T} \left(-\left(\frac{\vec{\nabla} T - \vec{\nabla} T \times \mu\vec{B}}{1 + \mu^2 B^2}\right)\right)\right) d\vec{k} \tag{1.51}$$ eq1.51

$$J^Q = -\int \vec{v}_k (\epsilon_k - \mu) \tau \vec{v}_k \left(\frac{\partial f^0}{\partial \epsilon_k} e \frac{\vec{E} - \vec{E} \times \mu\vec{B}}{1 + \mu^2 B^2} + \frac{\partial f^0}{\partial \epsilon_k} \frac{\epsilon_k - \mu}{T} \left(-\left(\frac{\vec{\nabla} T - \vec{\nabla} T \times \mu\vec{B}}{1 + \mu^2 B^2}\right)\right)\right) d\vec{k} \tag{1.52}$$ eq1.52

All the components of σ, κ, and α can be expressed in terms of a product of their zero field values (labeled σ_0, κ_0 and α_0) and a function of the magnetic field which involved only one parameter the electronic mobility $\mu = \frac{e\tau}{m}$:

$$\sigma_{\parallel} = \frac{\sigma_0}{1 + \mu^2 B^2} \tag{1.53}$$ eq1.53

$$\sigma_{\perp} = \frac{\sigma_0 \mu B}{1 + \mu^2 B^2} \tag{1.54}$$ eq1.54

$$\kappa_{\parallel} = \frac{\kappa_0}{1 + \mu^2 B^2} \tag{1.55}$$ eq1.55

$$\kappa_{\perp} = \frac{\kappa_0 \mu B}{1 + \mu^2 B^2} \tag{1.56}$$ eq1.56

$$\alpha_{\parallel} = \frac{\alpha_0}{1 + \mu^2 B^2} \tag{1.57}$$ eq1.57

$$\alpha_{\perp} = \frac{\alpha_0 \mu B}{1 + \mu^2 B^2} \tag{1.58}$$ eq1.58

We can see that the application of the magnetic field leads to a decrease in longitudinal electrical, thermal, and thermoelectric conductivity, it also induces an off-diagonal response. Note that we only discuss here the effect of the magnetic field on electrons as phonons are neutral particles and thus are not expected to be sensitive to the magnetic field. However, I will show in Chapter 3 that phonons can still play a key in the thermal properties of solids in the presence of a magnetic field due to electron-phonon scattering.

1.2 Experimental techniques

In the last section, we introduced the theoretical framework employed to understand the electrical, thermal, and thermo-electrical properties of solids. In this section, I will present the measuring principles. The cryogenic and magnetic environments, measurement of voltage, and temperature yielding these three quantities will be discussed.

1.2.1 Measuring principle

As we discussed before, the tensors of electrical, thermal, and thermoelectric are quantifiable physical properties of a solid. They represent the relation between the electrical (or the heat) current and the electric field (and or the temperature gradient) in a solid. Fig 1.2 is a sketch of the experimental setup used to measure on the same sample the three tensors: $\bar{\sigma}$, $\bar{\kappa}$, and $\bar{\alpha}$:

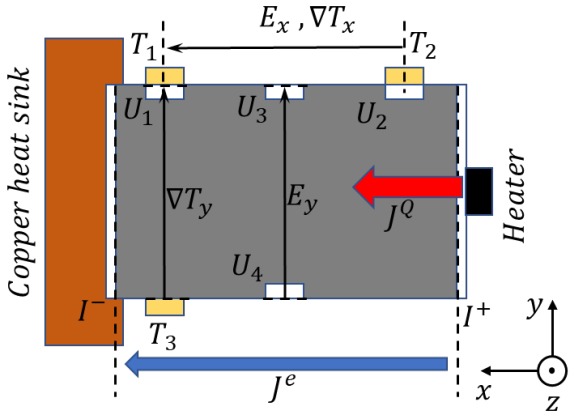

Fig. 1.2 *Sketch of the setup that allows to measure the three tensors $\bar{\sigma}$, $\bar{\kappa}$, and $\bar{\alpha}$ at the same time. T_1 T_2 and T_3 are three Cernox CX-1030 thermometers. The heater is a 1 $K\Omega$ chip resistor. All connections on the sample were made using silver paste. Six tin pads (white rectangles) are soldered on the sample for ohmic contacts.*

fig1.2

Let us first consider the case where there is no magnetic field so that the transverse responses are vanishing for the three tensors. The electric field and the temperature gradient are oriented parallel to the current flux or heat flux, so we can reduce these vectors to scalars as shown in Eq. 1.5 and 1.6 evaluate the transport coefficients.

The electric conductivity (σ)

For measuring the electrical conductivity: $J^e \neq 0$ and $J^Q = 0$. This induces an electrical potential parallel to the direction of the electrical current. By measuring the electrical potential difference between U_1 and U_2 (see Fig 1.2) we can evaluate the electrical resistivity $\rho = \frac{E}{J^e} = \sigma^{-1}$.

The thermal conductivity (κ)

For measuring the thermal conductivity: $J^Q \neq 0$ and $J^e = 0$. This induces a temperature difference on the two sides of the sample along the direction of the heat current. By measuring

the temperature difference between T_1 and T_2, we can evaluate the thermal resistivity $W = \frac{-\nabla T}{J^Q} = \kappa^{-1}$.

The thermoelectric conductivity (α)

As electrons are charged particles, the flow of particles induced by a heat current is also accompanied by an electrical potential to keep $J^e = 0$. This potential difference is known as the Seebeck effect, $S = \frac{E}{\nabla T} = \alpha\sigma^{-1}$. Inversely, an electric current induces a temperature difference. This is known as the Peltier effect. The Peltier coefficient is $\Pi = \frac{-\nabla T}{J^e}$ with $\Pi = ST$ according to the Kelvin relation [24]. Although there is always a thermoelectric contribution in any electrical or thermal measurement (see Eq. 1.5 and Eq. 1.6), in most cases these contributions are tiny and can be ignored while measuring the electrical and thermal conductivities.

Combining the expression of σ Eq 1.25 and α Eq 1.26 allows us to express the Seebeck effect :

$$S = \frac{\pi^2}{3}\frac{k_B^2}{e}T\frac{\partial ln\sigma}{\partial\epsilon}\mid_{\epsilon=\epsilon_F} \tag{1.59}$$ eq1.59

This equation is the so-called Mott formula, as it was first formulated in the thirties by Mott and Jones [42]. If we approximate : $\frac{\partial\sigma}{\partial\epsilon}\mid_{\epsilon=\epsilon_F} \approx \frac{\sigma}{\epsilon_F}$ Eq 1.59 becomes[24]

$$\frac{S}{T} = \frac{\pi^2}{3}\frac{k_B}{e}\frac{1}{T_F} \tag{1.60}$$ eq1.60

Eq 1.59 and 1.60 describe the diffusive thermal power. As electrons and phonons can both carry heat, there is an extra contribution to the thermo-power resulting from the electron-phonon momentum exchange known as the phonon drag effect. I will discuss both contributions in the case of lightly doped $SrTiO_3$ in Chapter 3.

In the presence of magnetic field- As discussed before, a magnetic field not only influences the longitudinal transport coefficients but also produces a transverse response, so we need to treat the Eq. 1.5 and 1.6 as tensors. Here we consider the case of an in-plane isotropic material which means that σ, α, and κ can simplify to 2×2 tensors:

$$\bar{\sigma} = \begin{bmatrix} \sigma_{xx} & \sigma_{xy} \\ -\sigma_{xy} & \sigma_{xx} \end{bmatrix}, \bar{\alpha} = \begin{bmatrix} \alpha_{xx} & \alpha_{xy} \\ -\alpha_{xy} & \alpha_{xx} \end{bmatrix}, \bar{\kappa} = \begin{bmatrix} \kappa_{xx} & \kappa_{xy} \\ -\kappa_{xy} & \kappa_{xx} \end{bmatrix} \tag{1.61}$$ eq1.61

Magnetoresistivity and Hall effect- In the presence of a magnetic field along the z axis, the electrical current flux $\vec{J^e}$ along the x axis direction will lead to an electrical potential difference along the y axis too. This is known as the Hall effect. The longitudinal resistivity $\rho_{xx} = \frac{E_x}{J^e}$ and transverse resistivity $\rho_{xy} = \frac{E_y}{J^e}$. Here $\frac{\rho_{xy}}{B} = \frac{1}{ne}$ (using to obtain the carrier concentration). Since $\bar{\sigma} = \bar{\rho}^{-1}$, one has:

$$\sigma_{xx} = \frac{\rho_{xx}}{\rho_{xx}^2 + \rho_{xy}^2} \tag{1.62}$$ eq1.62

$$\sigma_{xy} = \frac{-\rho_{xy}}{\rho_{xx}^2 + \rho_{xy}^2} \tag{1.63}$$ eq1.63

Thermal Hall effect- In the presence of a magnetic field along the z axis, a heat flux $\vec{J^Q}$ along the x axis will lead to a temperature gradient along the y axis too. This is known

as the thermal Hall effect (originally called the Righi-Leduc effect [43]). The longitudinal thermal resistivity is $W_{xx} = \frac{-\nabla T_x}{J^Q}$ and the transverse thermal resistivity is $W_{xy} = \frac{-\nabla T_y}{J^Q}$.

$\bar{\kappa} = \bar{W}^{-1}$, therefore

$$\kappa_{xx} = \frac{W_{xx}}{W_{xx}^2 + W_{xy}^2} \tag{1.64}$$ eq1.64

$$\kappa_{xy} = \frac{-W_{xy}}{W_{xx}^2 + W_{xy}^2} \tag{1.65}$$ eq1.65

In most cases, $W_{xx} \gg W_{xy}$, so the $\kappa_{xx} \approx -\frac{J^Q}{\nabla T_x}$ and $\kappa_{xy} \approx -\kappa_{xx}\frac{\nabla T_y}{\nabla T_x}$

The Nernst effect- In the presence of a magnetic field along the z axis, the heat flux $\vec{J^Q}$ along the x axis direction will also lead to an electric field along the y axis which is known as Nernst effect. In this case; Eq. 1.5 becomes

$$\begin{bmatrix} E_x \\ E_y \end{bmatrix} = \bar{\sigma}^{-1}\bar{\alpha} \begin{bmatrix} \nabla T_x \\ \nabla T_y \end{bmatrix} = \begin{bmatrix} S_{xx} & S_{xy} \\ -S_{xy} & S_{xx} \end{bmatrix} \begin{bmatrix} \nabla T_x \\ \nabla T_y \end{bmatrix} \tag{1.66}$$ eq1.66

with

$$S_{xx} = \frac{E_x \nabla T_x + E_y \nabla T_y}{\nabla T_x^2 + \nabla T_y^2} \tag{1.67}$$ eq1.67

$$S_{xy} = \frac{E_x \nabla T_y - E_y \nabla T_x}{\nabla T_x^2 + \nabla T_y^2} \tag{1.68}$$ eq1.68

As $\nabla T_x \gg \nabla T_y$, $S_{xx} = \frac{E_x}{\nabla T_x}$ and $S_{xy} = \frac{-E_y}{\nabla T_x}$. Combining the expression of $\bar{\sigma}$ and $\bar{S}$, we obtains α_{xx} and α_{xy}.

1.2.2 Measurement setup

The transport experiments were carried out in the Physical Property Measurement System (PPMS) or in a dilution cryostat. The combination allowed covering a large temperature range from 30 mK to 300 K with a magnetic field as high as 16 T. Homemade sticks and sample holders have been developed to measure during the same experimental run the three tensors. A sketch of the sample holder and of the PPMS probe is shown in Fig 1.3.

Resistivity and Hall effect measurements were done in four contact geometries as shown in Fig 1.2. Two wires were used to inject the electrical current, and 4 wires were used to measure the longitudinal and transverse voltages in order to determine E_x and E_y.

The situation is slightly more complicated for the thermal and thermoelectric transport measurements. The sample was glued on the cold sink with silver paste. Three thermometers (typically Cernox 1030) and one heater (Chip resistors) were glued on the sample using silver paint. Note that this is the insulating substrate side that is glued on the sample to prevent electrical contact between the sample and the thermometers. Gold wires on the

thermometers and heater are connected to manganin coils, formed by four twist wires, to avoid heat loss between the sample and the sample holder(radiation will also lead to a heat loss [44] but in our case, with a good thermal conductivity it can be ignored). The whole setup, shown on 1.3, is then mounted on a stick that fits into the PPMS of our laboratory. The resistance of thermometers and heaters is measured with the 4-wire method.

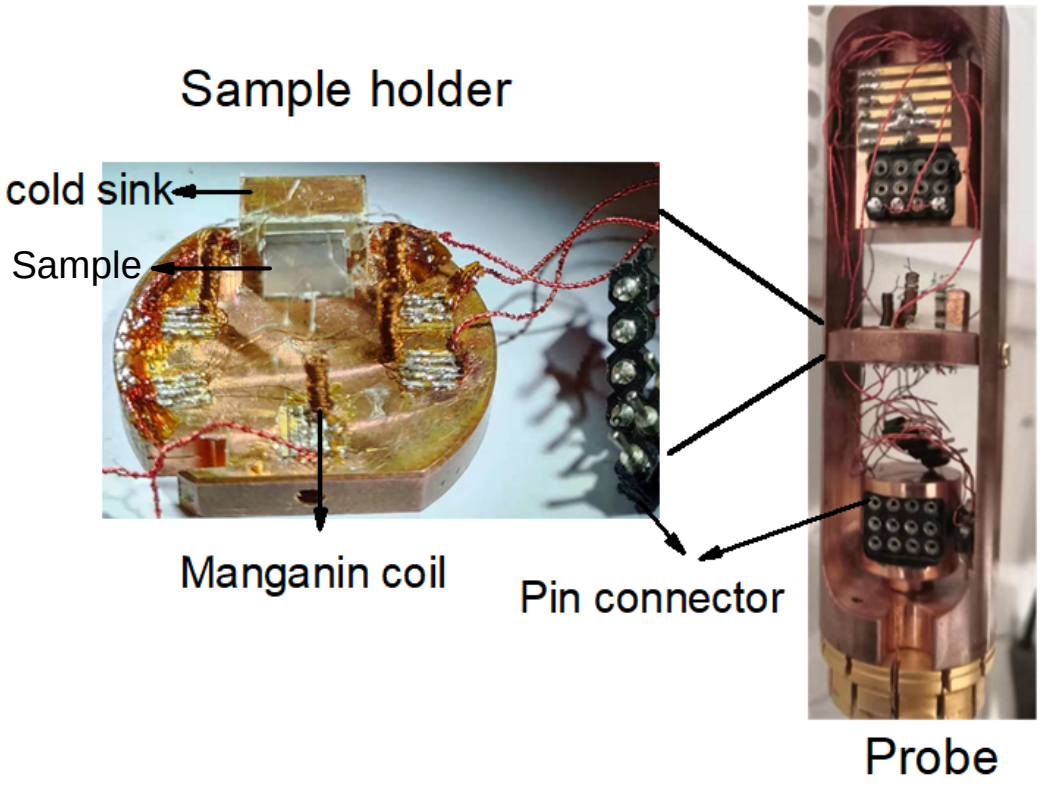

Fig. 1.3 *Photography of the sample holder response to the Sketch(Fig 1.2). The probe can be inserted into PPMS.*

fig1.3

1.2.3 Measurement of voltage

After preparing the setup, the last thing is measuring the longitudinal and transverse electric field (E_x and E_y) and temperature gradient (∇T_x and ∇T_y) and electrical current flux J^e and heat flux J^Q as shown in Fig 1.2.

Electrical current flux J^e and heat flux J^Q

The electric current is provided by a current source (Keithley-Model 6221) (see Fig 1.4). It can provide DC or AC from 1 nA to 100 mA (AC for measuring the resistance of Cernox and RuO_2 thermometers and DC for measuring sample resistance). The heat current is provided by a heater (RuO_2 chip resistor). We use the 4-wire method to detect the heat power of the heater, 2 wires are used to impose a current by Model 6221 and the other is for measuring the voltage. Ignoring the thermal radiation and heat leak from the manganin coil (We will discuss this later), the heat current density through the sample to the cold sink is equal to the power of the heater divided by the cross-section of the sample.

Electrical field E_x and E_y

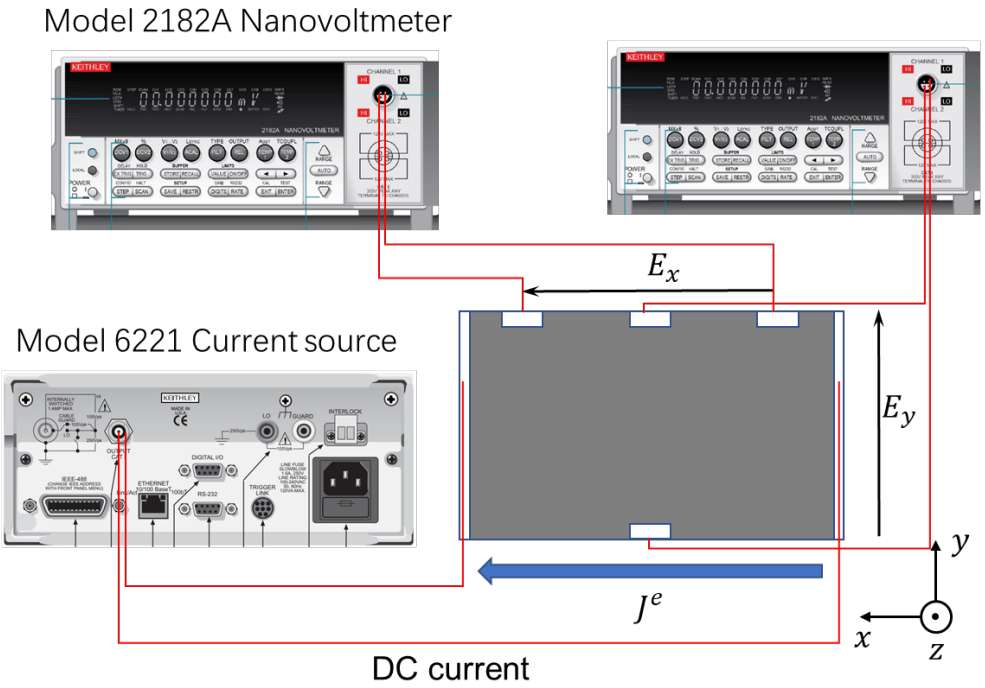

Fig. 1.4 *Measurement of the longitudinal and transverse electric field E_x and E_y along the sample. Model 6221 provides a DC current along the x axis. E_x and E_y are detected by two Model 2182A nanovoltmeters in the same time*

fig1.4

We used a (Keithley-Model 2182A) nanovoltmeter to measure the voltage between the two contacts on the sample along the x (y) axis as shown in Fig. 1.4. The noise level achieved was around 10 nV. The electric field equals the voltage divided by the distance between the two contacts. Even without the electrical and heat current through the sample, there is an offset signal. For measuring the resistivity and Hall effect, the current-reverse mode is used to compensate for the offset. For measuring the Seebeck and Nernst effect, we can subtract the measured voltage without heat current from the measured voltage with heat current to exclude the offset. Another detail is the unavoidable misalignment between each pair of lateral (and even longitudinal) electric and thermal contacts, so we need to symmetrize (for longitudinal) and antisymmetrize (for transverse) the signals for the magnetic field. This is relevant to both tE_x and ∇T_x (and much more for E_y and ∇T_y).

1.2.4 Measurement of temperature difference

We used three kinds of thermometers: Cernox 1030, RuO_2 chip resistor, and type E thermocouple to probe the local temperature at a given point of a sample. The temperature can be monitored by measuring the resistance of Cernox 1030 or RuO_2 chip resistor, or by measuring the thermoelectric voltage across a type E thermocouple.

Fig 1.5 shows the measuring circuit using the Cernox 1030 or RuO_2 chip resistor. Three thermometers are first connected in series. Then AC current provided by Model 6221 passes through the three thermometers. The AC voltage of each of the three thermometers is first amplified by the Model SR560 preamplifier and then detected by the Model SR830 lock-in amplifier. The voltage difference between a pair of resistive chips is measured with a high-precision. This yields the temperature difference.

Taking the Cernox 1030 as an example, we will show how can we get the absolute temperature and temperature difference in T_1 and T_2 as shown in Fig 1.2. Note that here T_1 is used as the standard thermometer. Before mounting it on the sample, its temperature-resistivity curve has already been calibrated in PPMS as shown in Fig 1.6 (b). This is the first calibration curve and we fit the temperature-resistivity curve in the log-log scale

$$f(lgT) = lgR_1 \tag{1.69}$$ eq1.69

During the measurement, we will measure another calibration curve using the resistivity of T_1 (R_1) to calibrate the resistivity of T_2 (R_2) when the heat current is zero (note that we use the differential mode to measure R_2) as shown in Fig 1.6 (a). From this curve, we can get another fit function

$$g(R_2) = R_1 \tag{1.70}$$ eq1.70

Having referred to two fit functions, we can accurately acquire the absolute temperatures T_1 and T_2 when the heat current is not equal to zero. For T_1, we need to inject lgR_1 into the first fit function Eq. 1.69. For T_2, we put R_2 into the first fit function (Eq. 1.70) to get its map to R_1. Then according to the first fit function, we get the T_2. Having obtained absolute T_1 and T_2, the temperature difference (equal to $T_1 - T_2$) and the sample temperature (equal to $\frac{T_1+T_2}{2}$) are both obtained. Note that the thermal conductivity is usually not linear with temperature, so we need to keep the temperature difference less than 10% of its absolute temperature.

We can use the same method to get a transverse thermal gradient in a magnetic field. These resistive thermometers also show magneto-resistivity, which can not be ignored especially at low temperatures. Compared to Cernox 1030, RuO_2 shows a smaller magneto-resistivity below 2 K. This is why we usually use it to do relative measurements at the temperature range of dilution.

In Chapter 5, the thermal conductivity of $EuTiO_3$ above 50 K is measured by using Type E thermocouples. Relevant measurement principles will be introduced in the Appendix.

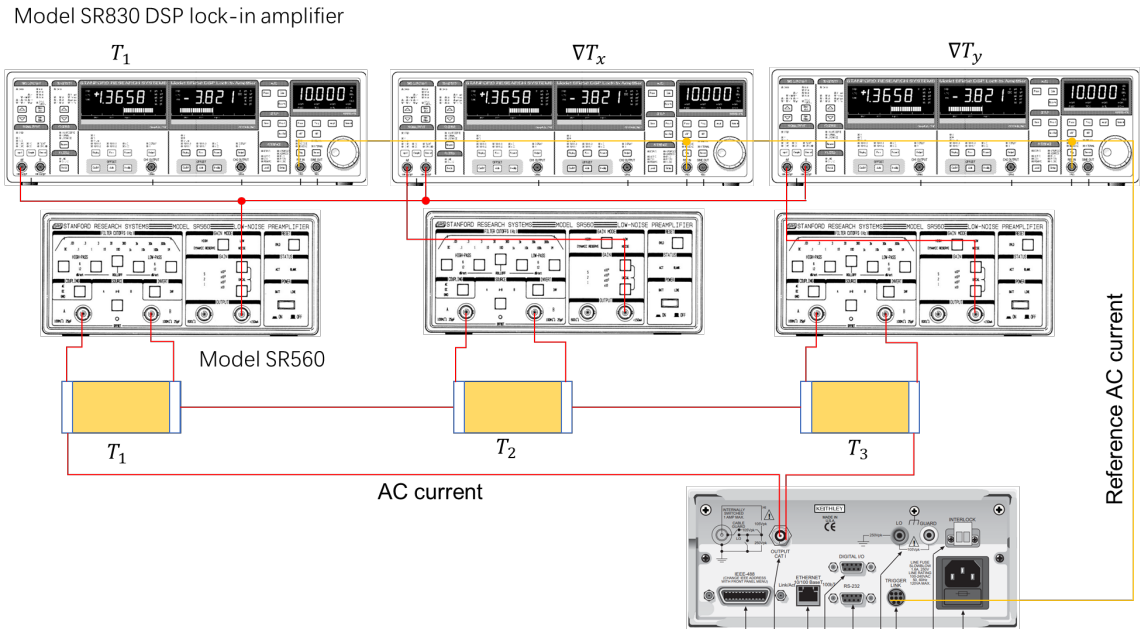

Fig. 1.5 *Measurement of temperature and temperature difference using three thermometers (Cernox 1030 or RuO_3 chip resistor). The AC current provided by Model 6221 passes through the three thermometers. The AC voltage of each three thermometers is first amplified by the Model SR560 preamplifier and then detected by the Model SR830 lock-in amplifier. The voltage difference between T_1 and T_2 (T_1 and T_3) is measured to have a high-precision temperature difference signal ∇T_x (∇T_y)*

fig1.5

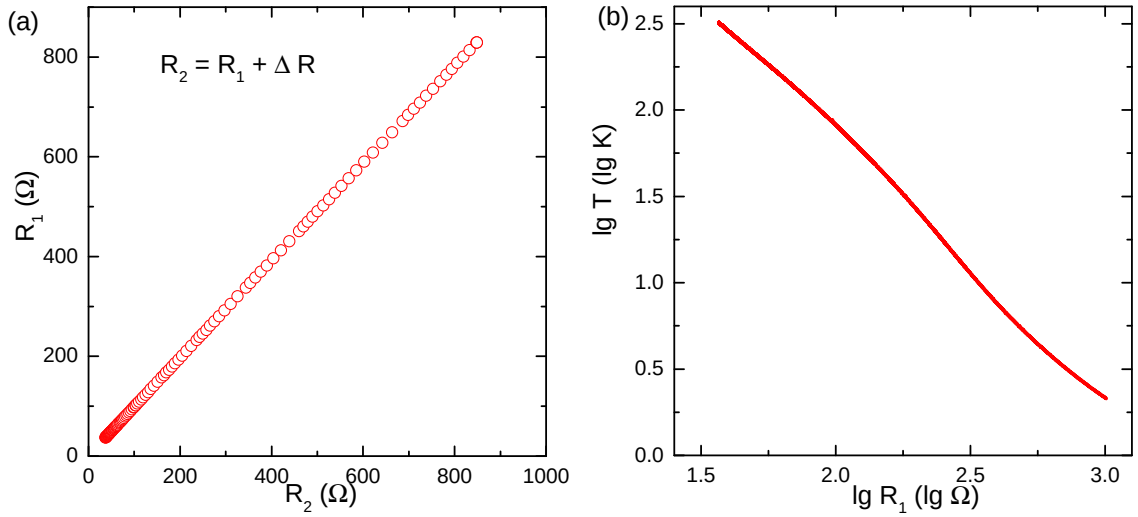

Fig. 1.6 *(a) the resistivity relation of thermometer T_2 and T_1 measured by the referred setup with no heat current(R_1 and R_2 are the resistance of thermometer T_2 and T_1). T_1 is the standard thermometer. (b) The resistivity and temperature calibration curve of standard thermometer T_1 in lg-lg scale. We use this curve to obtain the absolute temperature.*

fig1.6

Chapter 2

Research background

Summary of the Chapter

A member of the perovskite family, the quantum paraelectric $SrTiO_3$ has been studied for several decades. In this chapter, I will begin by reviewing its structural properties, including the antiferrodistortive transition and quantum paraelectricity, each associated with a distinct soft phonon mode. The electronic properties, the metallic and the superconducting states will be discussed afterward. These discussions will provide proper context for the new results presented in chapters 3 and 4. Then, I will introduce two other quantum paraelectrics with perovskite structure: $KTaO_3$ and $EuTiO_3$. The latter also shows an antiferromagnetic order due to the presence of Eu^{2+}. The coupling between quantum paraelectricity and magnetism provides context for the results presented in Chapter 5.

2.1 Overview of $SrTiO_3$

$SrTiO_3$ is a fascinating quantum paraelectric material known for its significant permittivity. Originally an insulator with a band gap of 3.2 eV, it can be transformed into a metallic and even superconducting state through n-type doping. The interplay between its lattice structure and the doping electrons has garnered recent attention due to the intriguing transport properties observed. Before delving into these properties, let us first revisit the comprehensive study of the structural and electronic characteristics of $SrTiO_3$.

2.1.1 Crystal lattice properties

2.1.1.1 Antiferrodistortive Transition

At room temperature, $SrTiO_3$ exhibits an ideal perovskite structure, formed by the tessellation of TiO_6 octahedra and SrO_{12} cuboctahedra (see Fig 2.1 (a)). It belongs to the cubic space group $Pm\bar{3}m$ with a lattice parameter of $a_c = 0.3905nm$ [45]. As the temperature decreases, a cubic-to-tetragonal transition occurs at around $T_{AFD} \approx 110$ K, where the TiO_6 octahedra tilt around the c axis. This structural change is referred to as the antiferrodistortive (AFD) transition and is non-ferroelectric in nature.

In 1964, X-ray measurements quantified the lattice change during the AFD transition, detecting a small tetragonal distortion with $c/a = 1.00056$ [46]. Three years later, electron

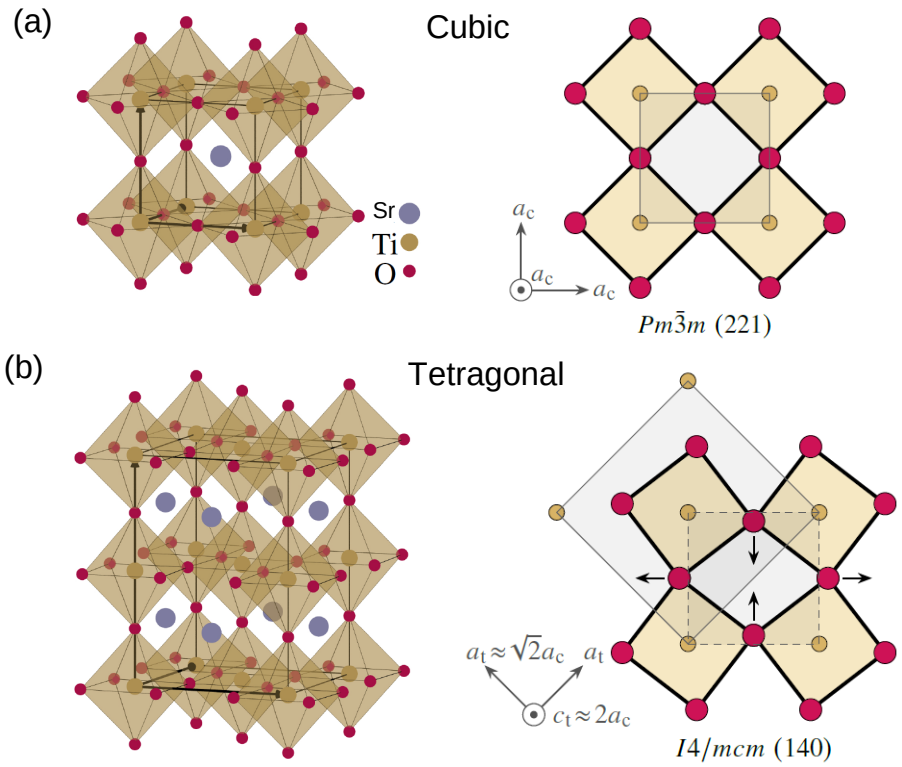

Fig. 2.1 **Illustration of the AFD transition in $SrTiO_3$.** *(a) Ideal cubic perovskite with the space group $Pm\bar{3}m$ at high temperature. (b) $I4/mcm$ of the low-temperature tetragonal phase. At the AFD transition, the oxygen ions move as indicated by black arrows. Along c_t, the octahedra tilt in an antiphase manner. The tetragonal unit cell volume is four times larger than the cubic phase.*

fig2.1

spin resonance measurements by Unoki and Sakudo determined the tetragonal phase to have a space group of $I4/mcm$ [47]. In this phase, the unit cell becomes $\sqrt{2}a_c \times \sqrt{2}a_c \times 2a_c$, resulting from adjacent TiO6 octahedra rotating clockwise and anticlockwise around the c axis (illustrated in Fig 2.1 (b)). The angle of rotation ϕ is approximately 1.4° at 77 K and increases to 2.1° at 4.2 K [47]. Raman and neutron scattering measurements in the late 1960s revealed that the triply degenerate phonon $F2u$ (Γ_{25}) at the R point of the Brillouin zone softens (approaches zero frequency) as the temperature decreases to T_{AFD} (Fig 2.2 (a)). Below T_{AFD}, this soft mode splits into a singlet for rotations around the c axis and a doublet for rotations around the a and b axes, and these two new zone center phonons (in the tetragonal structure) become harder. The second-order nature of this transition has been confirmed by the presence of a well-defined peak in the specific heat (Fig 2.2 (b)) [48].

Below T_{AFD}, the TiO_6 octahedra can rotate around each of the three perpendicular cubic axes. Consequently, as the temperature cools below T_{AFD} without any external strain, three types of tetragonal domains with three different directions of c axes along the cubic axes emerge. Researchers have managed to obtain single-domain samples by manipulating the crystal's shape or applying directional stress [49]. Additionally, the AFD transition is sensitive to the presence of minute amounts of extrinsic atoms. Introducing oxygen vacancies

reduces T_{AFD} [50; 51], while substituting Ti with Nb shifts it upward (both of these cases also introduce electrons, see section 2.1.2). Substituting Sr with La or Ca [51; 52] is beneficial for T_{AFD}, whereas it is detrimental with Ba and Pb [53]. Recently, McCalla et al. [54] conducted a comprehensive examination of the complex response of T_{AFD} to substitution and proposed a unified picture based on a combination of impurity-induced changes in the Goldschmidt tolerance factor and the ionic valence mismatch between the host and the impurity.

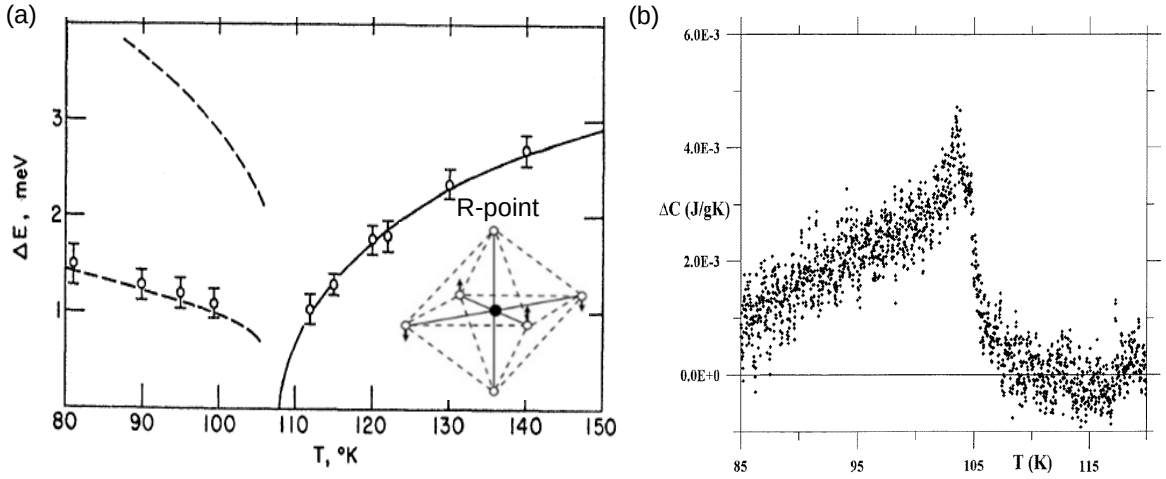

Fig. 2.2 **Γ_{25} soft phonon mode and second order transition at T_{AFD}** *(a) is the phonon energy of Γ_{25} mode at R-point in $SrTiO_3$ as the function of temperature and the insert is the vibration of Γ_{25} mode in octahedra [55]. At AFD transition temperature 105 K, Γ_{25} mode softens.(b) is the differential heat capacity as a function of temperature around AFD transition temperature 105 K [48].*

fig2.2

2.1.1.2 Quantum paraelectricity

Below 105 K, in the AFD phase with a tetragonal structure, $SrTiO_3$ experiences another lattice instability. While the first instability was linked to the condensation of a zone boundary acoustic mode, this second one arises from the softening of a transverse optical mode at the Γ-point, known as the $\Gamma 15$ mode, making it associated with a ferroelectric instability. The softening of the Γ_{15} mode (transverse optical mode) has been observed through Raman [58] and neutron scattering [55], as depicted in Fig 2.3 (a). Compared to the AFD transition, where the softening of the TA mode is complete, the frequency of the Γ_{15} mode never reaches zero even at the lowest temperature, and it stabilizes at a value of approximately $\omega_0 \approx$ 1-2 meV. Consequently, the system is near being ferroelectric and is often described as an incipient ferroelectric [59].

The presence of incipient ferroelectricity [59] in $SrTiO_3$ is evident in its large dielectric constant (ϵ_0), which follows the Lyddane-Sachs-Teller expression connecting ϵ_0 and ω_0: $\epsilon_0 \propto 1/\omega_0^2$. As the system is cooled from room temperature to liquid helium temperatures, the dielectric constant increases dramatically, reaching values as high as 20,000 times the vacuum permittivity [4]. With decreasing temperature, it deviates from the Curie-Weiss law and saturates, as depicted in Fig 2.3 (b) [4]. This state of quantum paraelectricity has been attributed to the presence of zero-point quantum fluctuations, which hinder the

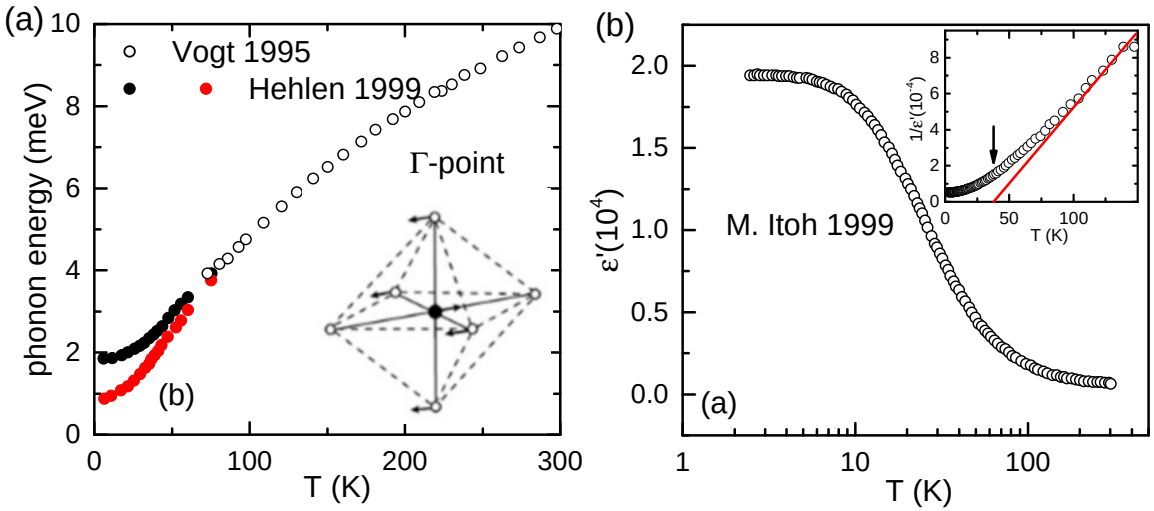

Fig. 2.3 **Γ_{15} soft phonon mode and large permittivity** *(a) is the phonon energy of Γ_{15} mode in $SrTiO_3$ as the function of temperature [56; 57]. The insert is the vibration of Γ_{15} mode in octahedra. Note that in the tetragonal phase below T_{AFD}, it is located at Γ-point. (b) is dielectric permittivity evolving with temperature [4]. There is no ferroelectricity peak. Inset shows the temperature dependence of $1/\varepsilon'$, the red line is a linear fit by using the Curie-Weiss law.*

fig2.3

establishment of long-range ferroelectric order [1; 60]. In the potential energy landscape of the polar soft mode as a function of the relative displacements of anions (O) and cations (Sr, Ti), a double-well shape with two minima corresponding to ferroelectric ground states with opposite polarizations is observed [61] (see Fig 2.3 (a)). In pristine $SrTiO_3$, zero-point fluctuations between these two states impede the emergence of long-range ferroelectric order.

The traditional knowledge of quantum paraelectric in $SrTiO_3$ has been challenged. In 2017, Rowley proposed that the quantum paraelectric in $SrTiO_3$ is attributed to ferroelectric quantum criticality [62; 63]. More recently another source of this remarkable state has been proposed. A series of inelastic neutron scattering measurements on $SrTiO_3$ shows that the softening of the TO mode is accompanied by a large TA-softening [64]. Motivated by this result Guzmán-Verri, Liang, and Littlewood [65] propose a Landau theory including a flexoelectric term in the Landau free energy. Such coupling not only softens the TA branch at a finite q vector but also leads to the repulsion of the modes giving rise to a saturation of the TO mode. In their picture, the TO/TA hybridization identified by the neutron results is the ultimate driver of the ground state of $SrTiO_3$ and not the zero point fluctuations as previously thought [66].

2.1.1.3 Ferroelectricity

As discussed above, $SrTiO_3$ is a quantum paraelectric while the ferroelectric order can be easily stabilized. It can be done in several ways by chemical substitution of a small fraction of Sr atoms with Ca [2] or Ba[3], by isotopic substitution (of ^{16}O with ^{18}O [4]), or by application of stress [59] or an electric field [69].

$Sr_{1-x}Ca_xTiO_3$ becomes ferroelectric for Ca concentrations restricted to a narrow win-

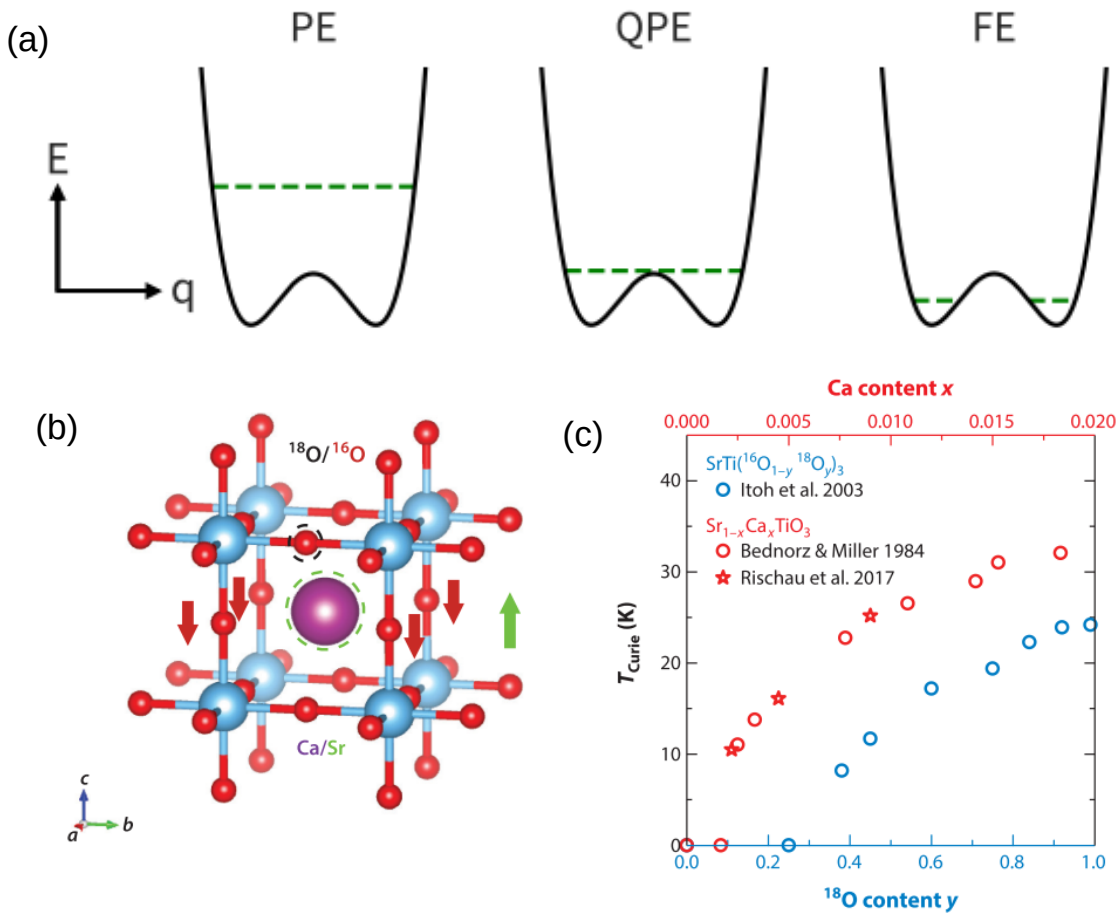

Fig. 2.4 *(a) Ferroelectric double-well potentials[61]. The vertical axis is internal energy, and the horizontal axis is the polarization (or relative displacements of the anionic and cationic sublattices), with the curves centered around zero polarization. The green dashed lines represent the zero-point energy levels. (b) Substituting ^{16}O with ^{18}O or Sr with Ca favors ferroelectricity [5]. Ca atoms are smaller than Sr and ^{18}O atoms are heavier than ^{16}O. (c) Curie temperature, T_{Curie}, determined from dielectric measurements in $SrTi(^{16}O_{1-y}{}^{18}O_y)$ [67] and $Sr_{1-x}Ca_xTiO_3$ [2; 68] as a function of Ca and ^{18}O content respectively.*

fig2.4

dow of $0.002 < x < 0.02$, while $SrTi(^{16}O_{1-y}{}^{18}O_y)_3$ begins at $y \approx 0.35$ as shown in 2.4 (c). Both of their Curie temperature T_C increase with increasing concentration. For the $SrTi(^{16}O_{1-y}{}^{18}O_y)_3$, the substitution of ^{16}O with larger-mass ^{18}O atoms lowers the zero-point energy in the ferroelectric double-well potential and tunneling between the two ground states is reduced, thus enabling a condensation of the polar soft mode [70](see in 2.4 (a)). It is more complicated in $Sr_{1-x}Ca_xTiO_3$. The substituted Ca atoms have a slightly smaller ionic radius ($0.099nm$) than that of Sr ($0.112nm$)(see Fig 2.3(b)). In the first (order–disorder or percolation) picture, Ca atoms take off-center positions and form polarized dipole clusters that grow in size with decreasing temperature. The percolation of these clusters at T_C leads

to a long-range ferroelectric order [71]. In the second picture, Ca substitution damps the quantum fluctuations that prevent ferroelectricity in pure $SrTiO_3$. A transverse Ising model has been used to describe the competition between the zero-point quantum fluctuations and the ferroelectric order [72]. In this model, the dipolar interaction between Ca sites enhances the cooperative exchange coupling between dipoles and suppresses tunneling between the possible ferroelectric ground states.

2.1.2 Metallicity of doped $SrTiO_3$

After discussing the lattice properties of $SrTiO_3$ I will now describe its electronic properties. This wide-gap semiconductor can be tuned into a metal once it is n-doped by substituting tiny Sr with La or Ti with Nb or removing O atoms [5]. Due to its large dielectric constant $SrTiO_3$ has a long Bohr radius. It is thus remarkably easy to change this insulator into a metal, and even a superconductor, with a very low electronic density. I will present in this section the electronic properties in its normal as well as state superconducting properties of $SrTiO_3$.

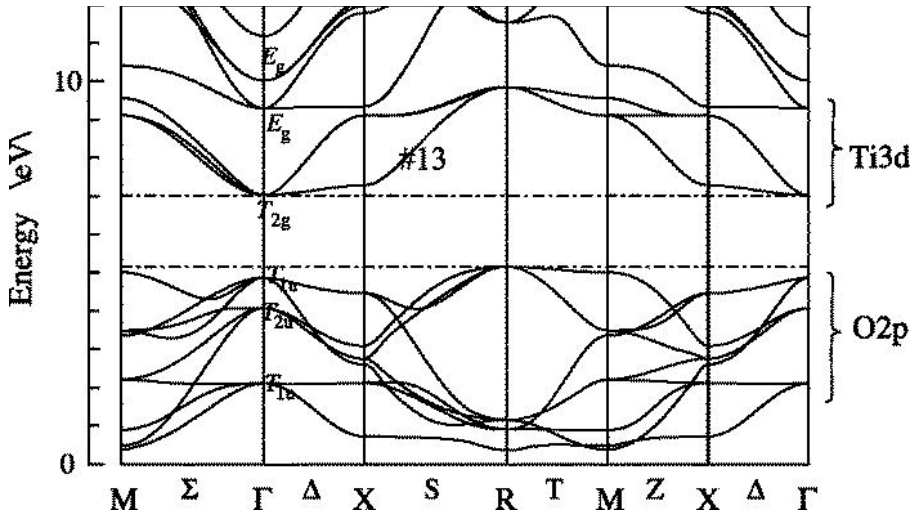

Fig. 2.5 *DFT calculation of the electronic structure for cubic phase $SrTiO_3$. The t_{2g} are the lowest-lying conduction bands. The # 13 is the dxy band. Adapted from[73].*

fig2.5

Band structure

Figure 2.5 shows the band structure of $SrTiO_3$ [73] according to DFT calculation. $SrTiO_3$ has an indirect bandgap of 3.25 eV and a direct bandgap of 3.75 eV, experimentally determined from valence electron-energy loss spectroscopy (VEELS)[74]. The primary contribution of the valence band is the $2p$ orbitals of oxygen atoms[75] and the conduction band is mainly composed of the Ti $3d$ orbitals. The tetragonal crystal field and the finite spin-orbit coupling [76] lead to the $3d$ orbitals split into t_{2g} and e_g. The d_{xy} (the # 13 in Figure 2.5), d_{yz} and d_{xz} orbitals of t_{2g} bands are degenerate at the conduction band minimum, the Γ point.

Fermi surface

The evolution of the Fermi surface of electronic doped $SrTiO_3$ has been well documented through the observation of quantum oscillations in magnetotransport measurements such as the Nernst effect [77] or magneto-resistivity[68; 78]. Fig 2.6 (a) shows the trace of these oscillations for a sample with a Hall carrier density n_H=1×10^{18}cm^{-3}. At this doping level, a single frequency was found [77]. As the carrier concentration increases, this Fermi surface grows in size and above a threshold concentration, n_{c1}, close to what the theory had suggested [79], a second small frequency, pointing to the emergence of an additional concentric pocket, is detected. The outer Fermi surface becomes heavier when $n > n_{c1}$, confirming another expectation of *ab*-initio calculation. An angle-dependent study of quantum oscillations in La-doped SrTiO3 thin films confirmed the expected anisotropy of the lower band at low carrier concentration. The success of the rigid-band picture using virtual crystal approximation in describing nonstoichiometric $SrTiO_3$ is remarkable. Here is not surprising that observing the quantum oscillation down to $10^{17}cm^{-3}$[77; 80] or even $10^{16}cm^{-3}$[81] because of the parent insulator of dilute metallic $SrTiO_3$ is a quantum paraelectric with a large dielectric constant which leads a large effective Bohr radius[24; 82].

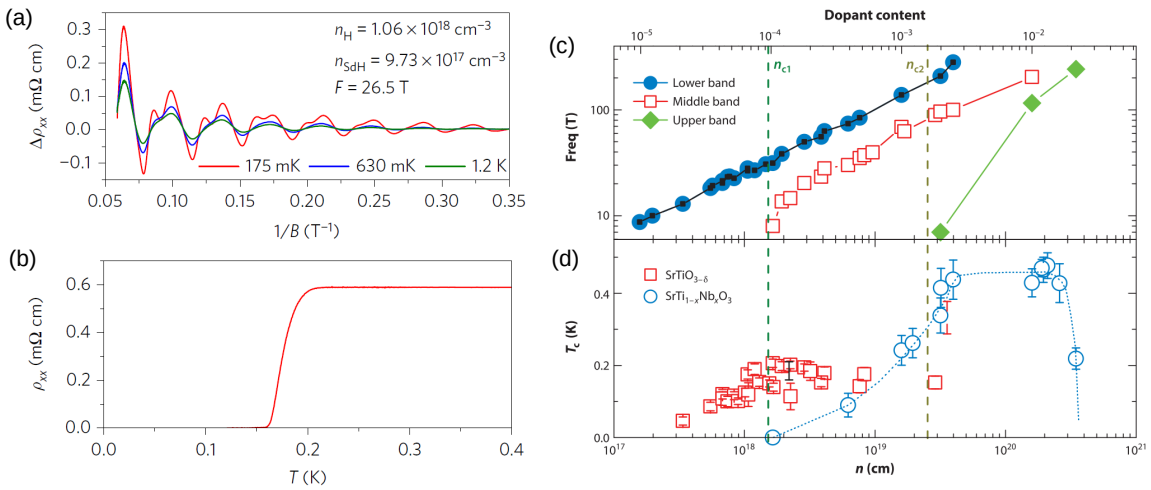

Fig. 2.6 *(a) and (b) dilute metallic $SrTiO_3$ displays quantum oscillations of resistivity and a superconducting transition[68]. (c) The evolution of the frequency of quantum oscillations with carrier concentration. At two critical doping levels, n_{c1} and n_{c2}, new frequencies emerge, marking the occupation of new bands[5]. (b) The resistive superconducting phase diagram in $SrTiO_{3-\sigma}$ and in $SrTi_{1-x}Nb_xO_3$[5].*

fig2.6
section1.4

T-square resistivity

At low temperatures, the electric resistivity of n-doped $SrTiO_3$ can be expressed as $\rho = \rho_0 + AT^2$ as shown in Fig 2.7 (a). This behavior persists over four orders of magnitude in carrier density from $3\times10^{17}cm^{-3}$ (corresponding to $2\times10^{-5}e^-perf.u.$) up to $2\times10^{21}cm^{-3}$ [83]. As the doping decreases the amplitude of this T^2-therm increases to become as large as a few $\mu\Omega cmK^{-2}$ as shown in Fig 2.7 (b), which is typical of a heavy-electron metal.

As discussed in section 1.2, T^2 resistivity in a Fermi liquid is related to the temperature dependence of the phase space for electron-electron scattering. This phase space is inversely proportional to the square of the Fermi energy; therefore, the smooth increase in

the magnitude of the prefactor with decreasing Fermi energy[84] (which scales with carrier concentration[83]) is qualitatively expected. In Fermi liquids, there are two known ways for collision between electrons to generate a finite contribution to electric resistivity. The first is Umklapp scattering [14; 31], during which the colliding electrons lose a unit vector of the reciprocal lattice. The second is the Baber mechanism [16]. If there are two reservoirs of electrons, with one being more coupled to the lattice than the other one, even if the momentum is ultimately lost by electron-phonon collisions, the rate is set by a bottleneck set by the momentum exchange rate between the two reservoirs. While below the threshold concentration n_{c1} in metallic $SrTiO_3$, both the two ways don't exist (the single Fermi surface is too small for Umkalp scattering). In Chapter 4, we will combine the study of thermal resistivity to discuss the origin of T^2 resistivity in dilute $SrTiO_3$.

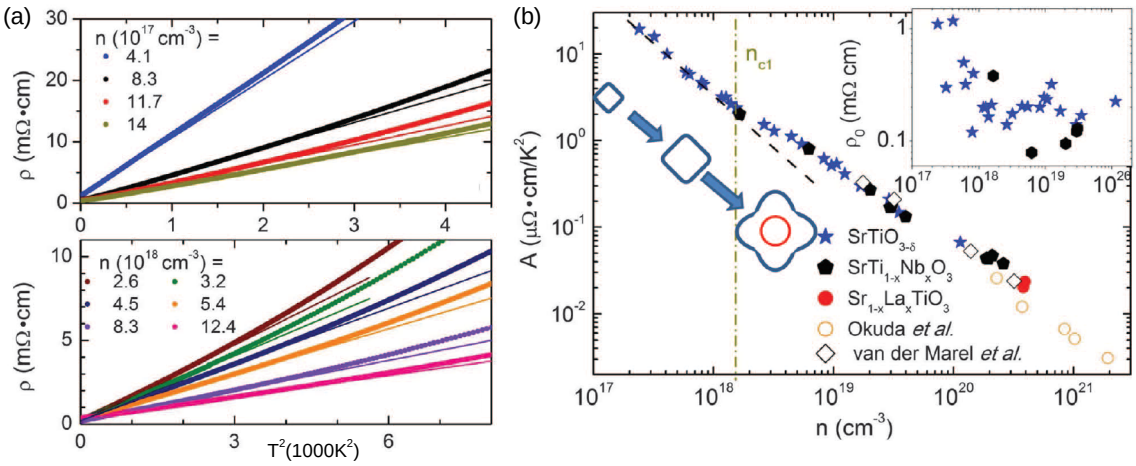

Fig. 2.7 *(a) Resistivity versus T^2 in $SrTiO_{3-\sigma}$ evolve with the carrier density. Straight solid lines represent the best fits to low-temperature data[83]. (b) The prefactor A of T^2 resistivity as a function of carrier concentration on a log-log scale[83]. The evolution of the Fermi surface with increasing concentration is also depicted here. Below n_{c1}, the Fermi surface is a simply squeezed ellipsoid, whereas above n_{c1} it has two concentric components with growing outer lobes. (Inset) Residual resistivity ρ_0 extracted from $\rho = \rho_0 + AT^2$ fits.*

fig2.7

Superconductivity

In the 1960s, superconductivity was discovered in n-doped STO[85; 86]. It is a key moment in the history of solid-state physics as $SrTiO_3$ has been the first superconducting oxide discovery paving the way for many others. Moreover, it is the first system where a superconducting dome has been discovered. As a function of the carrier density the superconducting critical temperature traces out a dome peaked at $T_c \approx 200mK$ for O-reduced $SrTiO_3$ and $T_c \approx 450mK$ for Nb-doped $SrTiO_3$ (see Fig 2.6 (d)). More recently the discovery of superconductivity down to very low density in $SrTiO_{3-\delta}$ (which is absent in Nb-doped STO) has triggered a renewal of interest in the pairing mechanism governing superconductivity in $SrTiO_3$ (for more details, see recent reviews by Collignon et al.[5] and by Gastiasoro et al.[6] and Enderlein et al. [87]).

2.1.3 Lattice heat transport properties

Two transport phenomena related to phonon hydrodynamics[88], second sound, and Poiseuille flow have been observed in $SrTiO_3$ due to the presence of soft modes in the phonon spectrum. The second sound is a wave-like propagation of temperature or entropy, found in $SrTiO_3$ by using Brillouin scattering[89] and low-frequency light scattering [90]. Poiseuille flow, on the other hand, occurs when the temperature dependence of thermal diffusivity is affected by the variable viscosity of the phonon fluid, and it has been detected through a study of thermal conductivity [40] as shown in Fig 2.8(a). The faster-than-cubic thermal conductivity is attributed to a Poiseuille flow of phonons. Both the second sound and Poiseuille flow of phonons require a combination of frequent normal scattering and rare resistive collisions such as Umklapp and impurity scattering. Strong coupling between soft and acoustic phonons [91] can enhance normal scattering, and this has been invoked to explain the observation of phonon hydrodynamics in $SrTiO_3$ [40; 90].

In addition to the phonon hydrodynamics signatures, a recent discovery in $SrTiO_3$ is the presence of a giant thermal Hall effect (THE) [92], as depicted in Fig 2.8(b). Unlike electrons affected by Lorenz force or magnons and spinons, phonons are the exclusive heat carriers in $SrTiO_3$ (high-temperature superconductor cuprates[93] or the Kitaev spin-liquid candidate $\alpha-RuCl_3$[94–96]), exhibiting a transverse response. The origin of the phonon chirality in these materials remains unknown. However, experimental measurements in strontium titanate indicate a connection between the thermal Hall effect and the AFD transition [9] or the instability of ferroelectricity [97], which paves the way for studying the chiral phonons. In Chapter 3, we will show our new result of the thermal Hall effect in $SrTiO_3$.

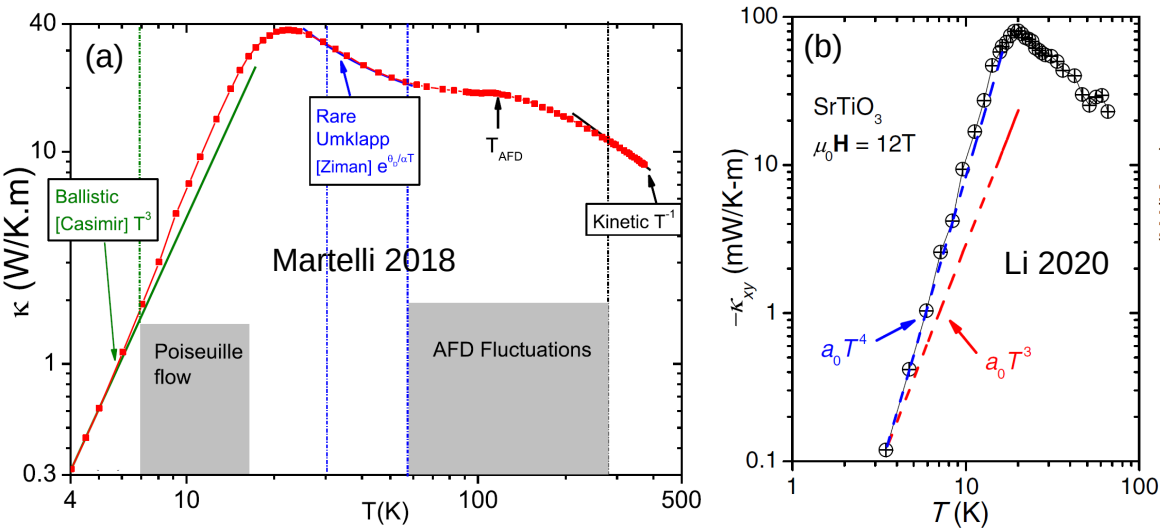

Fig. 2.8 *(a) Thermal conductivity of a $SrTiO_3$ crystal (closed red squares) in a log-log plot[40]. Different regimes of thermal transport are identified. Solid lines represent the expected behaviors in these regimes. An additional window due to enhanced Umklapp scattering opens up in the vicinity of the antiferrodistortive (AFD) transition. (b) The temperature dependence of κ_{xy} in the presence of a magnetic field of 12 T in $SrTiO_3$[92].*

fig2.8

2.2 Other quantum paraelectric materias

The remarkable quantum paralectric properties of $SrTiO_3$ can also be found in other ABO_3 perovskites. This is the case in potassium tantalate $KTaO_3$ (KTaO) and europium titanate $EuTiO_3$ that I will introduce in this section.

2.2.1 Quantum paraelectric $KaTO_3$

Compared to $SrTiO_3$, $KTaO_3$ is a much simpler case. In contrast to $SrTiO_3$, there is no structural transition. It remains cubic down to the lowest temperature [98]. Like in $SrTiO_3$ a large softening of the transverse optical mode (triply-degenerate) was found by neutrons and hyper-Raman measurement as shown in Fig 2.9 (b). Its frequency never goes to zero [99] and its dielectric constant reaches a value as large as 5000 (see Fig 2.9 (a)), slightly smaller than in $SrTiO_3$, giving rise to its quantum paralectric behavior [100].

In the last years, there has been a renewal of interest in the case of $KTaO_3$ as superconductivity has been found on $KTaO_3$ interfaces. It has been, first, found on LAO/KTO(111) with a $T_c = 2$ K [101], on LAO/KTO(110) T_c=0.9 K [102], but not on LAO/KTO(001) down to 25 mK [101]. The striking orientation dependence of T_c in $KTaO_3$ interfaces and its absence in bulk is the subject of intense discussions.

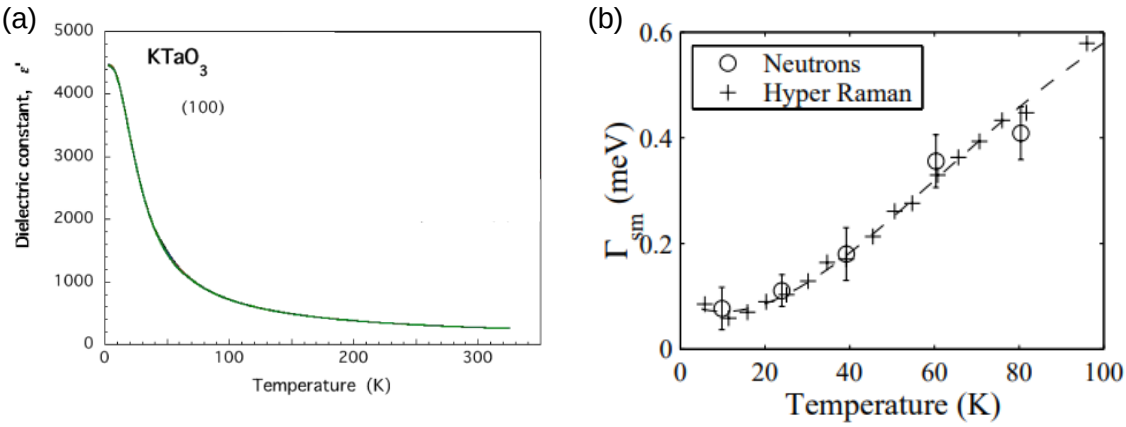

Fig. 2.9 *(a)Dielectric constant ϵ' of $KTaO_3$ along [100] as a function of heating temperature[100]. (b) the energy damping of soft zone center TO-mode by neutrons and hyper-Raman measurements[99].*

fig2.9

2.2.2 Magnetic $EuTiO_3$

$EuTiO_3$ displays the same lattice structure as $SrTiO_3$: $EuTO_3$ still shows the AFD transition which is not surprising since the ionic radius of Eu^{2+} is nearly the same as Sr^{2+} [103; 104]. Both the lattice parameters and heat capacity show the trace of the cubic-to-tetragonal transition that occurs at the AFD transition shift to the same as the AFD transition in STO as shown in Fig 2.10.

In contrast to $SrTiO_3$ there is an additional degree of freedom at work in $EuTiO_3$: the $4f$ moments the Eu^{2+} ($S = \frac{7}{2}$) which becomes a G-type antiferromagnet below 5 K (see

Fig 2.11 for the spin structures). Katsufuji et al. have shown that the onset of the AFM order is correlated with an appreciable anomaly in the dielectric permittivity [21], see Fig 2.11 (b). This in turn has been related to a soft optical mode reminiscent of ferroelectric instability, thereby suggesting the possibility of multiferroic capabilities [105]. I will discuss in Chapter 5 another striking manifestation of the spin-lattice coupling in $EuTiO_3$ giving rise to a reduced phononic thermal conductivity.

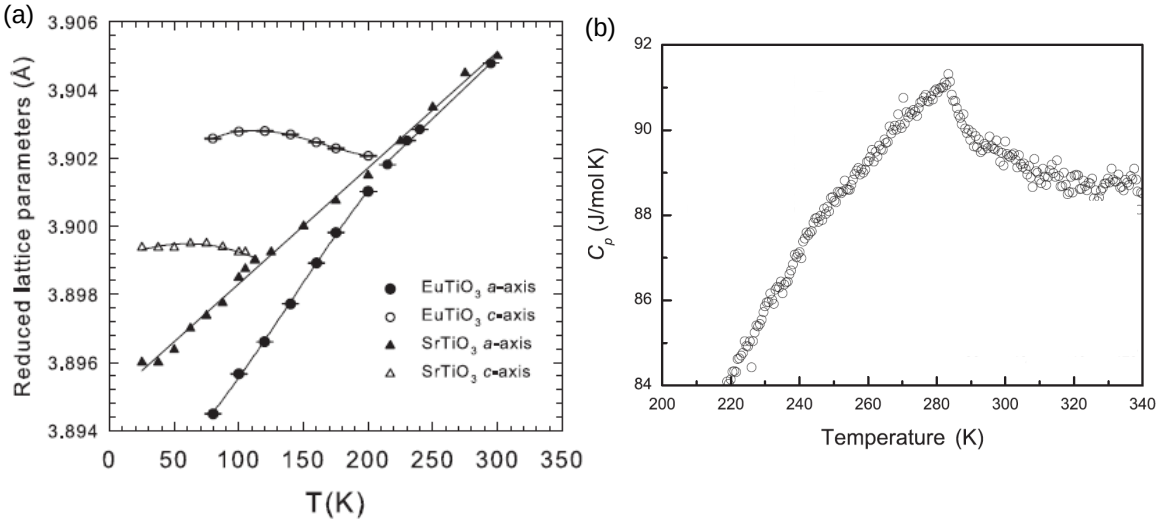

Fig. 2.10 *(a)Reduced lattice parameters of $EuTiO_3$ and $SrTiO_3$ as a function of temperature[106]. (b) Specific heat of ETO as a function of temperature in the temperature range around the AFD transition[107].*

fig2.10

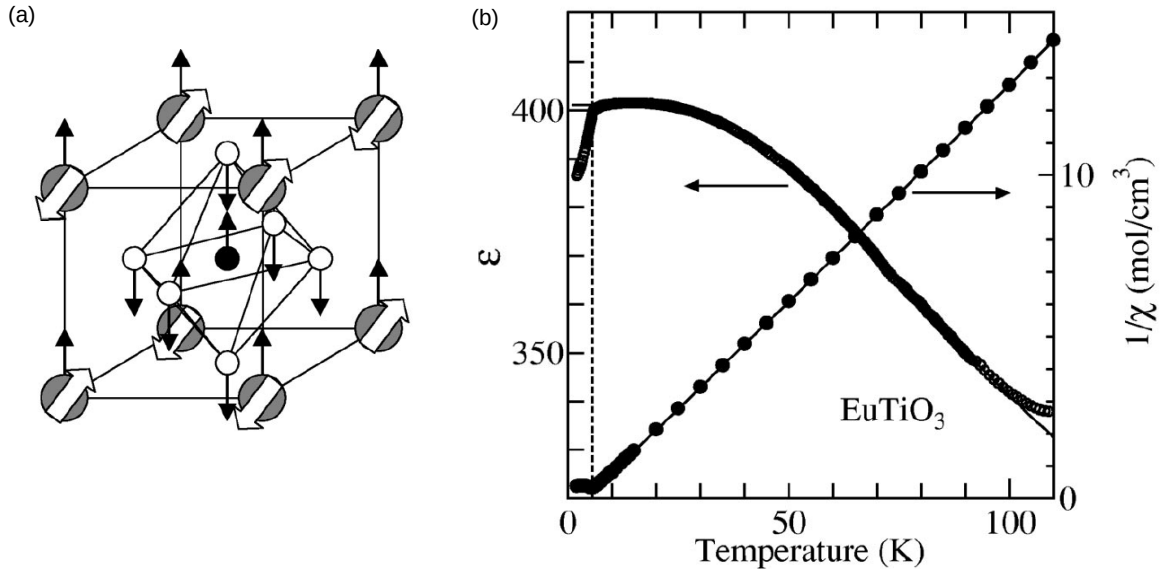

Fig. 2.11 *(a) crystal structure of $EuTiO_3$[21]. Gray, white, and black circles correspond to Eu, O, and Ti, respectively. White thick arrows represent the antiferromagnetic ordering of Eu spins. Thin arrows show the atomic motion of the soft-phonon mode with T_{1u} symmetry (b) temperature dependence of dielectric constants (left axis) and inverse magnetic susceptibility (right axis) for $EuTiO_3$[21].*

fig2.11

Chapter 3

Thermal Hall effect in strontium titanate

Summary of the Chapter

In this chapter, I will introduce the phenomenon known as the phonon thermal Hall effect (THE) and its occurrence in $SrTiO_3$. We examined how THE in $SrTiO_3$ changes with different atomic substitutions, focusing on two types of doping: substitution of Sr by Ca, which stabilizes the ferroelectric order, and the introduction of oxygen vacancies that turn the insulator into a metal. THE is suppressed by the ferroelectric order, suggesting that ferroelectric fluctuations play a crucial role in generating THE in $SrTiO_3$. On the other hand, the removal of oxygen atoms and the emergence of dilute metallicity amplifies THE. I will argue that the source of this enhancement is a specific case of phonon drag effect driven by an exceptionally large electronic Hall angle.

The content of this chapter is based on the paper published in S. Jiang et al., PNAS. 119 (35) [108].

3.1 Thermal Hall Effect in metals and in insulators

The first observation of the thermal Hall effect was made by A. Righi and S. A.Leduc at the end of the 19th century in the semi-metal bismuth. This phenomenon, initially observed in conductors, is called the Righi-Leduc effect as introduced in Chapter 1. Since the electrons carry a non-negligible portion of the thermal current in metals they can be deflected by the Lorentz force and give rise to a transverse thermal gradient.

In insulators, the original discovery was made in the insulator $Tb_3Ga_5O_{12}$ [7; 8]. The small thermal Hall conductivity κ_{xy} ($\approx$1 mW $K^{-1}m^{-1}$) was attributed to skew scattering of phonons by superstoichiometric Tb impurities [109]. A much larger thermal Hall effect was successively observed in other insulating solids.

Besides magnetic insulators [110–112], a thermal Hall effect in multiferroic $Fe_2Mo_3O_8$ [113] whose was attributed to magnetic excitations. Thermal Hall effect was also found in Kitaev spin-liquid candidate α-$RuCl_3$ [95], cuprate Mott insulators [93; 114; 115], such as La_2CuO_4 and $Sr_2CuO_2Cl_2$, and the quantum paraelectric $SrTiO_3$ [9].

In the latter case, the thermal Hall effect is purely phononic, but its origin is still

unknown. More recently, the thermal Hall effect reported in antiferromagnetic insulators Cu_3TeO_6 [116] and Sr2IrO4 [117] and black phosphorus [118]. Fig 3.1 shows the evolution of the experimentally observed κ_{xy} in different materials as a function of time in a semi-log scale. Note that although the κ_{xy} in these materials differs in three orders of amplitude, while the ratio of κ_{xy} and κ_{xx} which is called thermal Hall angle are not so different around few per thousand[118].

Let us now focus on the thermal Hall effect in quantum paraelectric $SrTiO_3$, its origin, and its evolution with atomic substitution.

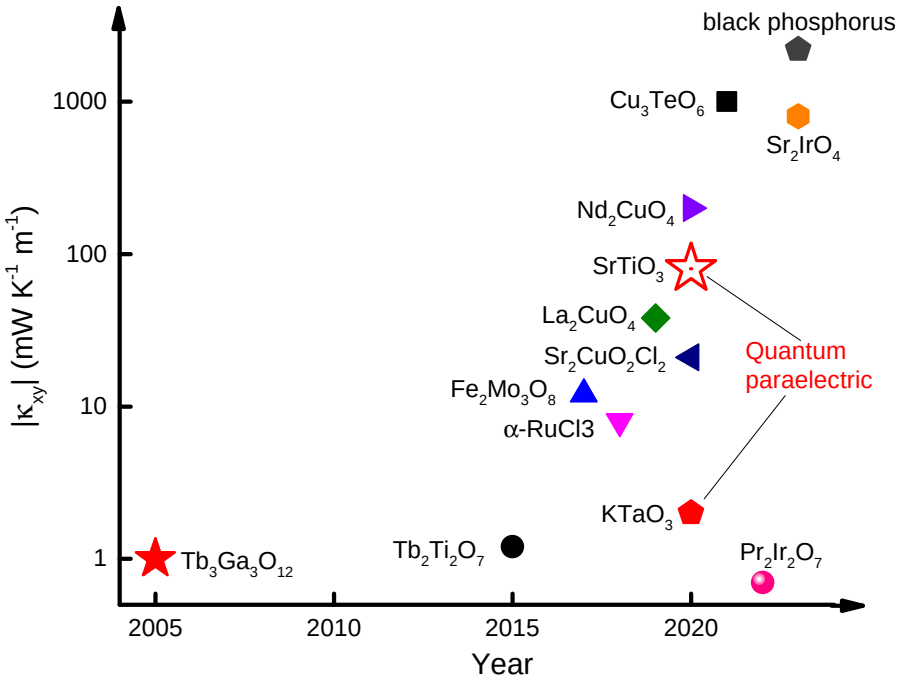

Fig. 3.1 *Thermal Hall effect in insulators. The absolute peak value of κ_{xy} of different materials [7; 9; 93; 113–120] in log scale as a function of year.*

fig3.0

3.2 Origin of the thermal Hall effect in STO

The underlying cause of the THE in STO is still a subject of debate. Two possible causes are the presence of antiferrodistortive (AFD) transition [92]. Another possibility is the role played by the ferroelectric fluctuations [97].

3.2.1 Possible role of the AFD transition ?

$KTaO_3$ is a quantum paralectric with a thermal conductivity similar to STO. However, the transverse thermal conductivity κ_{xy} in $KTaO_3$ is more than one order of magnitude

smaller than in STO, as shown in Fig 3.2 (a) and (b). Moreover, the amplitude of κ_{xy} is sample-dependent, and warming above the AFD transition temperature can alter its value, as illustrated in Fig 3.2 (c). These experimental observations suggest the involvement of tetragonal domains in producing THE [92].

Theoretically[11], two possible sources have been proposed: extrinsic κ_{xy} related to skew scattering and intrinsic κ_{xy} linked to ferroelectric fluctuations. The intrinsic κ_{xy} is still orders of magnitude smaller than the observed effect, and the extrinsic κ_{xy} proportional to the phonon mean-free path appears likely to explain the observations. However, the detailed scattering mechanism in the AFD phase is yet to be established.

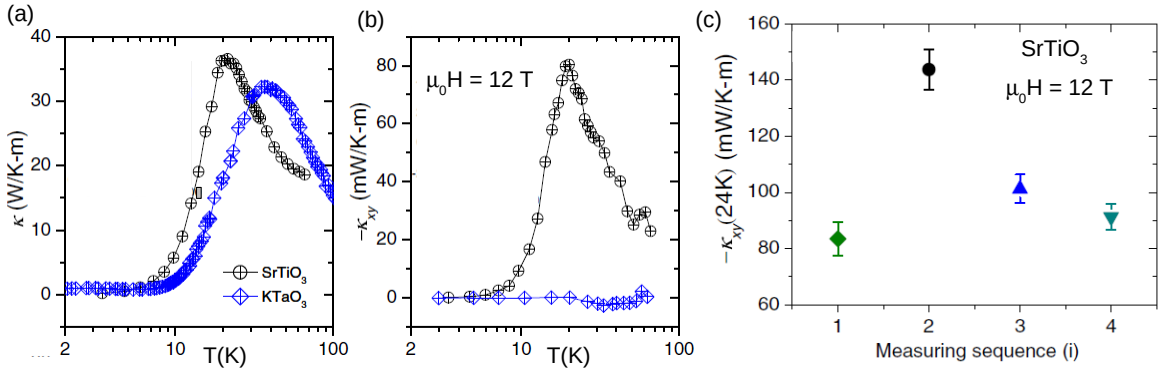

Fig. 3.2 *(a) and (b) longitudinal thermal conductivity κ and transverse thermal conductivity κ_{xy} in $SrTiO_3$ and $KTaO_3$ [92]. (c) κ_{xy} of the $SrTiO_3$ at 24 K as a function of measuring sequence [92], separated by the warming history of being warmed to room temperature and staying in the air for days, data extracted from the field-sweeping curves.*

fig3.1

3.2.2 Ferroelectric fluctuations?

Substituting ^{16}O by ^{18}O in STO makes the system ferroelectric. In isotopically-substituted STO (STO18) the AFD transition persists and the ferroelectric order is stabilized. It has been found that κ_{xy} in STO18 is two orders of magnitude smaller than in STO [97] (Fig 3.6), indicating that the ferroelectricity in STO18 suppresses the THE. However, the amplitude of the effect cannot be explained by ferroelectric fluctuations in the previously referred theory [11]. Somehow the large THE in STO shows the strong link between THE and the presence of quantum critical fluctuations of polarization and phonons.

Thus, the large thermal Hall effect in STO remains to be explained. In the following sections of this chapter, I will present my experimental findings on the thermal Hall effect [insulating] Ca-substituted and [metallic] oxygen-reduced STO.

3.3 Samples

In this section, I will introduce the samples and their preparations.

3.3.1 $Sr_{1-x}Ca_xTiO_3$

$SrTiO_3$ (STO) and $Sr_{1-x}Ca_xTiO_3$ (CaSTO) single crystals were provided by CrysTech and SurfaceNet GmbH. The list of STO and CaSTO samples studied in this work, together with their dimensions, the peak amplitude of κ_{xx} and κ_{xy} and their Ca concentration, is shown in Table 3.1. Ca concentration has been determined using Secondary Ion Mass Spectrometry (SIMS) like in [52]. The amplitude of the κ_{xx} peak is similar in all STO samples while the amplitude of κ_{xy} peak varies from 20 to 80 $mWK^{-1}m^{-1}$. This variation does not clearly correlate with the amount of residual Ca impurities determined by SIMS.

No.	Supplier	Dimensions (mm)	Peak of κ_{xx} ($W.K^{-1}m^{-1}$)	Peak of κ_{xy} ($mW.K^{-1}.m^{-1}$)	Ca concentration (ppm)
Ref#1 [92]	SurfaceNet	$5 \times 5 \times 0.5$	37	80	3.8
Ref#3 [92]	SurfaceNet	$5 \times 5 \times 0.5$	35	26	2.5
#1	CrysTech	$5 \times 5 \times 0.93$	38.6	21.6	290
#2	SurfaceNet	$5 \times 5 \times 0.5$	34	24	69
#3	SurfaceNet	$5 \times 5 \times 0.5$	32	24	-
#4	CrysTech	$5 \times 5 \times 0.82$	-	3.3	4500
#5	CrysTech	$5 \times 5 \times 0.99$	-	0.6	9100

Table 3.1: Properties of the insulating samples studied in this work. Ca concentration was determined using Secondary Ion Mass Spectrometry (SIMS) and is expressed in part per million (ppm).

table3.1

3.3.2 $SrTiO_{3-\delta}$ preparation

The preparation of reduced $SrTiO_3$ is divided into two steps sketched in Fig.3.3. The first step is the sample reduction and the second one is the deposit of electrodes.

$SrTiO_{3-\delta}$ samples were obtained by annealing them in a temperature range extending from 700^oC to 1000 ^oC under a high vacuum ($< 10^{-5}$ mbar) for 1 to 2 hours as shown in Fig 3.3. MILA-5000 furnace was employed as the heating system which uses a high-intensity lamp as the primary heat source. This system can precisely control the annealing temperature and is programmable. A secondary vacuum is achieved thanks to a turbo pump connected to the furnace chamber.

After annealing the STO sample, we put contact on the sample. This can be done in two ways: either by sputtering gold on the sample surface with a mask (see Fig 3.3 step 2) or by directly soldering thin with an ultrasonic soldering system (please give the reference of the machine). Both methods give ohmic contact resistivity during the measurement. In the case of gold sputtering an extra sample heating of the sample in the air at 300 ^oC can be reacquired to improve the contact resistance. This last has almost no effect on the carrier density induced by the oxygen vacancies.

As shown in Fig 3.3 the color of the STO sample changes from elementary to blue after undergoing annealing. This simple observation serves as an elemental indicator of the presence of oxygen vacancies after the annealing [121; 122]. However, a more precise method to quantify the oxygen vacancies number is to measure the carrier concentration using the Hall effect ($\frac{\rho_{xy}}{B} = \frac{1}{ne}$). I have shown in Fig. 3.4 how the annealing temperature is linked to the Hall carrier density. As the temperature increases the number of vacancies increases and thus the Hall carrier density. This result is consistent with previous reports [77; 123] and provides us a benchmark for producing samples with the desired carrier concentration.

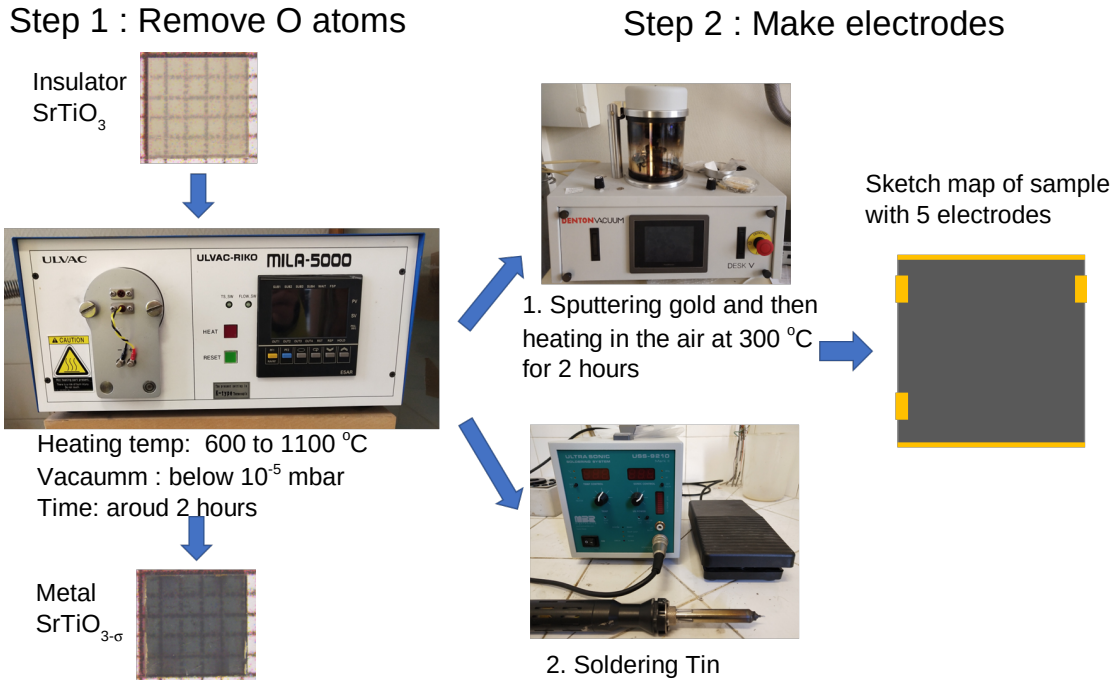

fig3.2

Fig. 3.3 *The process of preparation metallic $SrTiO_{3-\delta}$ samples.*

In the course of this PhD tens of samples have been prepared following the procedure described above and shown in Fig 3.3. Fig.3.5 shows the typical temperature dependence of the electrical resistivity (ρ) for four of them. These four samples have been used in our study of THE which I will present in the next section. In order to minimize the change in the amplitude of THE found in the different batches the four samples have been reduced from samples from the same batch (#3 in table 3.1).

Hall effect measurements allow us to estimate the carrier concentration for these four samples. It is ranging from 2.3×10^{16} to 1.6×10^{18} cm^{-3}. As each oxygen vacancies provide $2e^-$ we can roughly estimate the number of oxygen vacancies ($\sigma = \frac{na^3}{2}$ where a is the $SrTiO_3$ lattice parameter) in each sample : it varies from 7×10^{-7} to 4.8×10^{-5} per formula unit.

The temperature dependence of ρ for these four samples is in good agreement with previous works [83; 123]. Samples with carrier density larger than 10^{17}cm^{-3} display a metallic behavior down to the lowest temperature. In contrast, the lowest doped sample ($n = 2.3 \times 10^{16} cm^{-3}$) shows an upturn below 30 K, possibly due to inhomogeneous oxygen vacancies distribution or to the approach of a genuine metal-insulator transition. This is in agreement with a previous study, which reported an insulating behavior in samples with a carrier density below $n = 3 \times 10^{16} cm^{-3}$ [123].

3.3.3 Thermal Hall effect in $Sr_{1-x}Ca_xTiO_3$

Another way to stabilize the ferroelectric order in $SrTiO_3$ is to substitute Sr by Ca. Fig.3.7 shows the result of our study of the longitudinal and transverse thermal conductivity in three $Sr_{1-x}Ca_xTiO_3$ samples. One can clearly see that the Ca-doping decreases both the

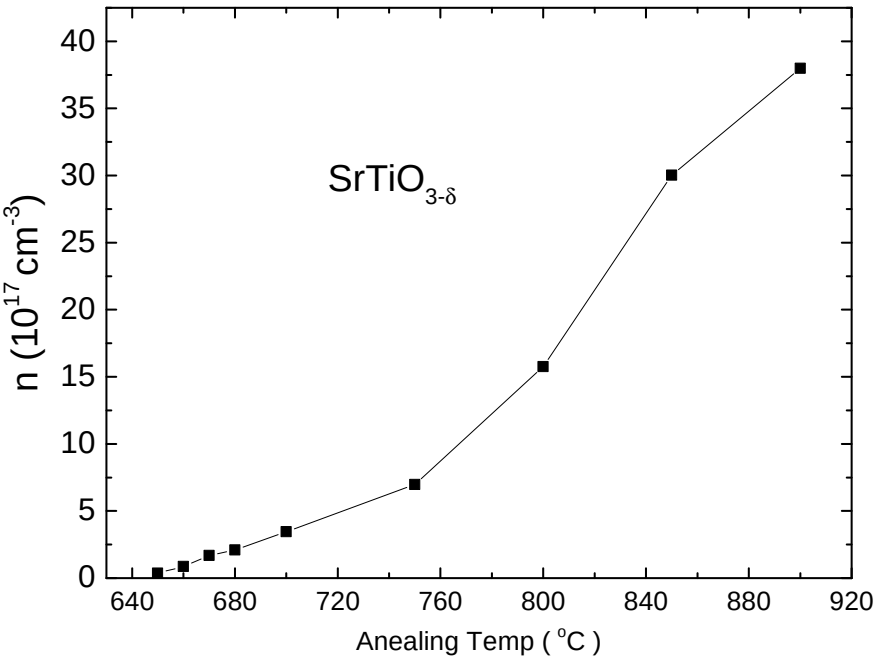

Fig. 3.4 *Carrier density of $SrTiO_{3-\delta}$ as a function of annealing temperature (the vacuum chamber was kept below 10^{-5} mbar)*

fig3.3

amplitude of κ_{xx} and κ_{xy}.

The decrease in κ_{xx} can be attributed to the random distribution of Ca atoms that introduce additional scattering. As in the case of Nb substitution [40], introducing less than a percent concentration of extrinsic atoms is sufficient to wipe out the 20 K peak of the thermal conductivity. The decrease in κ_{xy} is even more drastic. Substituting a tiny fraction (x=0.002) of Sr atoms with Ca is sufficient for stabilizing a long-range ferroelectric order [2]. This substitution eventually leads to a fifty-fold decrease in the magnitude of κ_{xy} which is comparable with the ^{18}O substitution referred to before(Fig 3.6).

Substituting Sr by Ca [68; 124] and substituting ^{16}O with ^{18}O [4; 125] both stabilize the ferroelectric order, modify the superconducting dome and generate a polar metal in the presence of Nb doping [126]. In both cases, the large κ_{xy} of the quantum paraelectric solid is drastically suppressed with the stabilization of the ferroelectric order. This suggests a link between the amplitude of κ_{xy} and the presence of ferroelectric fluctuations [11]. Note that in ^{18}O-enriched strontium titanate [97], most ^{16}O atoms were substituted and the 20 K peak in κ_{xx} is still present, in contrast to what is seen here. Yet, κ_{xy} was similarly damped, ruling out that κ_{xy} is simply more sensitive to disorder.

3.4 Thermal Hall effect in metallic STO

After discussing the fate of THE in ferroelectric STO, let's now discuss what happens to THE of STO once electrons are added to the system.

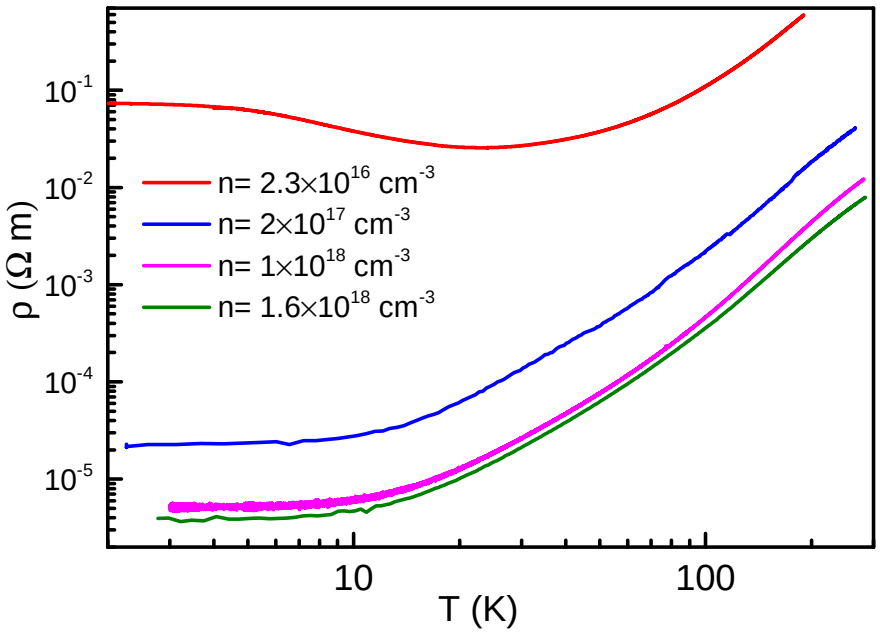

Fig. 3.5 *Electrical resistivity (ρ) as function of temperature for $SrTiO_{3-\delta}$ samples with different carrier concentrations.*

fig3.4

3.4.1 Temperature dependence of κ_{xx} and κ_{xy}

The temperature dependence of longitudinal and transverse thermal conductivity in $SrTiO_{3-\delta}$ are shown in Fig.3.8 (a),(b). The magnitude of longitudinal κ_{xx} barely changes with oxygen reduction. By using the resistivity data measured at the beginning and combining the Wiedemann-Franz (WF) law, we estimated the amplitude of the electronic thermal conductivity κ^e. It remains less than 10^{-2} : the total thermal conductivity (κ) is thus purely phononic. Therefore, the phonon contribution to κ is not significantly reduced by the addition of oxygen vacancies and of a finite electronic contribution. We note that the concentration of vacancies for $n = 1.6 \times 10^{18} cm^{-3}$ is only $\delta = 4.8 \times 10^{-5}$ per formula unit is much lower than the lowest amount of Ca substitution (x= 4.5×10^{-3}).

Like κ, κ_{xy} peaks at the same temperature in the four samples however the amplitude of the peak increases with the increasing n. Fig. 3.8 (c) compares the amplitude of κ_{xy} peak as a function of the concentration of Ca atoms (x) and O vacancies (δ) in parts per million (ppm) in log-log scale. While κ_{xy} is increases by about a factor of four in the presence of O vacancies it decreases by one order of magnitude with Ca doping. Clearly, the two dopants have different effects on the THE of $SrTiO_3$ and show that the enhanced THE in oxygen reduced sample is linked to the introduction of electrons in STO.

3.4.2 Field dependence of κ_{xy}

Fig. 3.9 (a) compares the field dependence of κ_{xy} in different samples at 20 K (i.e. near its peak). In the sample with the lowest carrier concentration ($n = 2.3 \times 10^{16} cm^{-3}$), the amplitude of κ_{xy} is almost identical to the insulating sample and remains linear in a magnetic field. In samples with higher carrier concentration, the amplitude of κ_{xy} is larger and shows

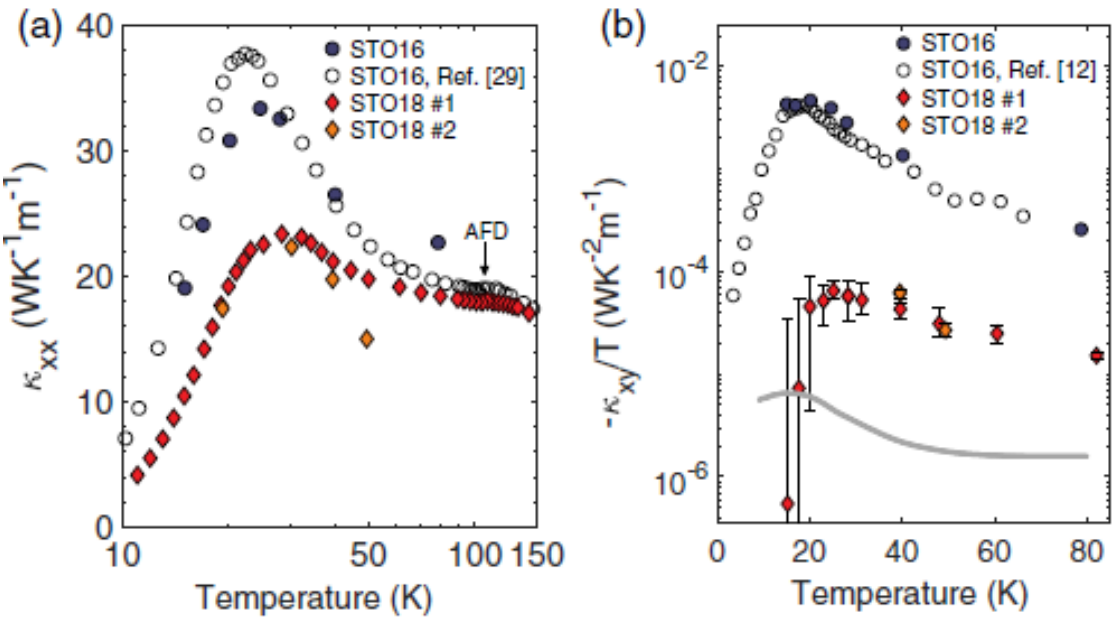

Fig. 3.6 *(a) Longitudinal thermal conductivity κ_{xx} of $SrTi^{16}O_3$ (STO16) and $SrTi^{18}O_3$ (STO18) [97]. STO18 samples have a slightly lower κ_{xx} value but behave similarly to STO16. Both have similar peak positions and a subtle suppression of κ_{xx} near the AFD transition around 110 K. (b) Transverse thermal conductivity (κ_{xy}) as function of temperature at $B = 9$ T [97].*

fig3.5

a gradual trend towards high-field saturation. This last behavior contrasts with the usual B-linear dependence usually observed for THE. This point should have been discussed in section 2.

At first sight the enhancement of κ_{xy} with the carrier density is not surprising as electrons have a thermal Hall response. Fig. 3.9 (b) shows the electronic contribution to THE (estimated from the measured electric Hall conductivity of the metallic samples: $\kappa^e_{xy} = L_0\sigma_{xy}T$ as seen in chapter 1). It shows a field-induced saturation similar to what is observed in κ_{xy}. However, subtracting the purely phononic component (taken to be equal to what is observed in the insulator) and the purely electronic component (estimated from the WF law) from the total κ_{xy} leaves us with an additional $\Delta\kappa_{xy} = \kappa_{xy} - \kappa^{ph}_{xy} - \kappa^e_{xy}$ as shown in Fig. 3.9 (c). Fig. 3.9 (d) shows the temperature dependence of the different components of THE in the sample with the highest carrier concentration ($n = 1.6 \times 10^{18} cm^{-3}$). One can see that $\Delta\kappa_{xy}$ exceeds κ^{ph}_{xy} and is several times larger than κ^e_{xy} in most of the temperature range. Note also that the temperature dependence of $\Delta\kappa_{xy}$ is significantly different from κ^e_{xy}. We thus conclude that there is, in addition to the usual electronic and phononic contribution, a third contribution to THE effect in electron-doped $SrTiO_3$.

3.4.3 Thermoelectric correction to thermal conductivity

Before discussing this unexpected extra-contribution to κ_{xy} let's make two comments about the above estimation of the electron contribution to κ_{xy}.

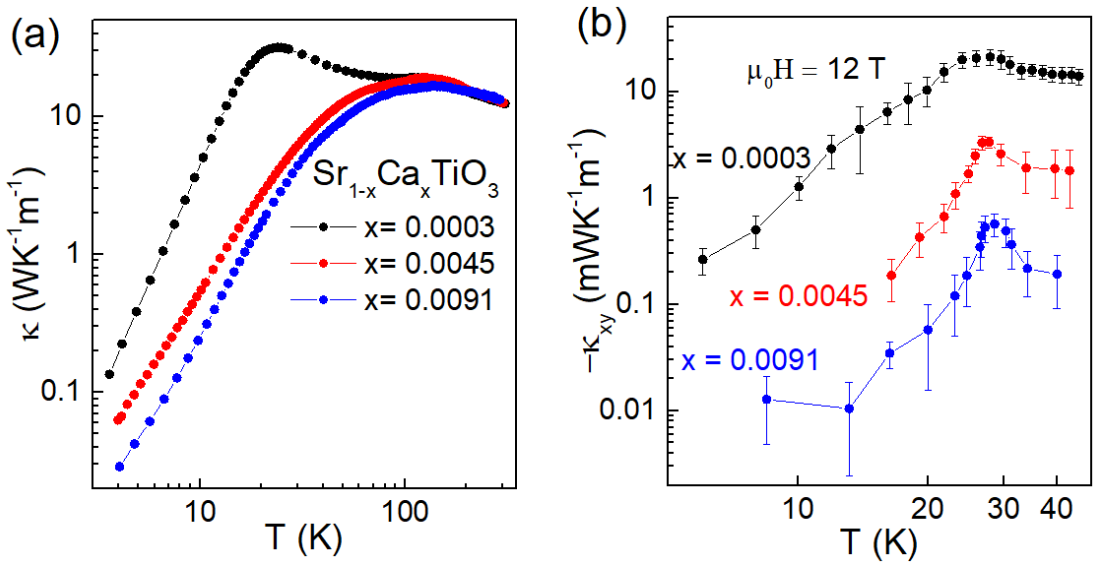

Fig. 3.7 *(a) and (b) Temperature dependence of the longitudinal (κ) and transverse (κ_{xy}) thermal conductivity in $Sr_{1-x}Ca_xTiO_3$*

fig3.6

First, we note that the WF law is only valid in the zero temperature limit and is not strictly valid at finite temperatures. However, the finite-temperature correction does not modify the order of magnitude of the expected electronic thermal conductivity. Moreover, since inelastic scattering damps thermal transport more than electrical transport, the expected correction to the Lorenz ratio is downward. Thus, $L_0\sigma_{xy}T$ gives an upper bound to the expected κ^e_{xy} and we can safely conclude that enhanced THE is not simply due to the introduction of mobile electrons.

Second, in the discussion above, we also neglect the contribution of the thermo-electric response to the thermal response. As discussed in the Chapter 3 in the presence of both an electrical and heat current the transport equations can be written as:

$$\vec{J^e} = \overline{\sigma'}\vec{E} - \overline{\alpha}\vec{\nabla}T \tag{3.1}$$ eq3.1

$$\vec{J^Q} = \overline{\alpha}T\vec{E} - \overline{\kappa'}\vec{\nabla}T \tag{3.2}$$ eq3.2

where $\overline{\sigma'}$ and $\overline{\kappa'}$ are different from $\overline{\sigma}$ and $\overline{\kappa}$ defined by Ohm's law($\vec{J^e} = \overline{\sigma}\vec{E}$) and Fourier's law ($\vec{J^Q} = -\overline{\kappa}\vec{\nabla}T$). In the case of a thermal experiment where $\vec{J^Q} \neq \vec{0}$, $\vec{J^e} = \vec{0}$) Eq. 3.2 becomes :

$$\vec{J^Q} = (\overline{\alpha}\,\overline{\rho}\,\overline{\alpha}\,T - \overline{\kappa'})\vec{\nabla}T \tag{3.3}$$ eq3.3

where $\overline{\rho} = \overline{\sigma}^{-1}$ and :

$$\overline{\kappa} = \overline{\kappa'} - \overline{\alpha}\,\overline{\rho}\,\overline{\alpha}\,T \tag{3.4}$$ eq3.4

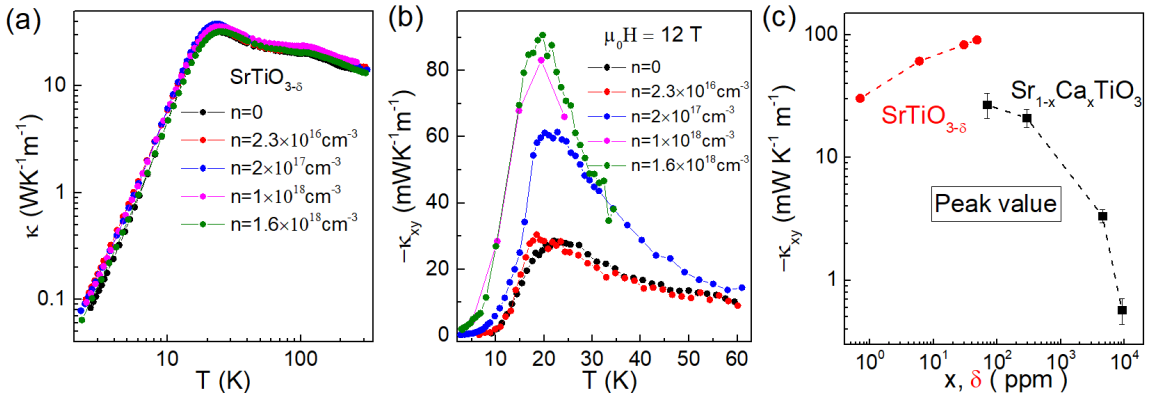

Fig. 3.8 *(a) Temperature dependence of longitudinal thermal conductivity κ in $SrTiO_{3-\sigma}$. Electron doping has almost not effect on κ. (b) Temperature dependence of transverse thermal conductivity κ_{xy} in $SrTiO_{3-\delta}$ in log-log scale. The amplitude is enhanced with oxygen substitution. (c) The amplitude of κ_{xy} peak as a function of the concentration of Ca atoms (x) and O vacancies (δ) in parts per million (ppm).*

fig3.7

The estimate correctly $\overline{\kappa'}$ in electron-doped STO we thus need to measure on the same sample $\overline{\kappa}$, $\overline{\alpha}$ and $\overline{\sigma}$.

We describe below the different ways that we used to evaluate κ, $\kappa^{'}$, σ, and $\sigma^{'}$ in a consistent way. Fig. 3.12 (b) - (e) shows the field dependence of the tensor component of α, σ κ and $\kappa^{'}$. The transverse thermal flow (but not the longitudinal one) is drastically affected by the particle-driven flow of entropy represented by the thermoelectric response. In other words, $\kappa_{xx} \simeq \kappa'_{xx}$, but κ_{xy} and κ'_{xy} are significantly different. This striking difference is the consequence of two properties of the dilute electron-doped $SrTiO_3$. First it has a large Hall angle ($\sigma_{xx} \approx \sigma_{xy}$) as shown in [127]. Second, it has a large thermoelectric power. Fig 3.10 shows the temperature dependence of the Seebeck coefficient for samples with different carrier densities. On top of a diffusive response which is large due to the low Fermi energy of the charge carrier, there is a second contribution which peaks at 20 K due to the phono-dragg contribution.

As the consequence of these large Hall angle and large Seebeck effect the diagonal and off-diagonal components $\overline{\alpha}$ have of the same order of magnitude. In contrast, the diagonal component of the thermal conductivity tensor (Fig 3.11 d) is orders of magnitude larger than the off-diagonal one (Fig 3.11 e). As a consequence, while the difference between κ_{xx} and κ'_{xx} is of the order of percent (Fig 3.11 d), κ'_{xy} is 2 times larger than κ_{xy} (Fig 3.11 e). It is also the case at different temperatures that we are interested in as shown in Fig 3.12

Thus, the corrected transverse thermal conductivity κ'_{xy} is larger than the measured one κ_{xy}, which is itself larger than the expected one(the sum of κ^{ph}_{xy} and κ^{e}_{xy}). The large electric and thermoelectric Hall angles which led to this correction is a key ingredient of the solution to the puzzle. Let us now consider the others.

To determine the components of the 2 × 2 tensors $\overline{\sigma'}$, $\overline{\kappa'}$ and $\overline{\alpha}$, we conducted two types of experiments (See Fig. 3.13 a and d). In the first one, a heat current is applied along the x-axis ($\vec{J^Q} \neq \vec{0}$) and the electric current was kept at zero ($\vec{J^e}$=$\vec{0}$), and we call it the thermal experiment. In the second one, an electric current is applied along x axis ($\vec{J^e} \neq \vec{0}$)

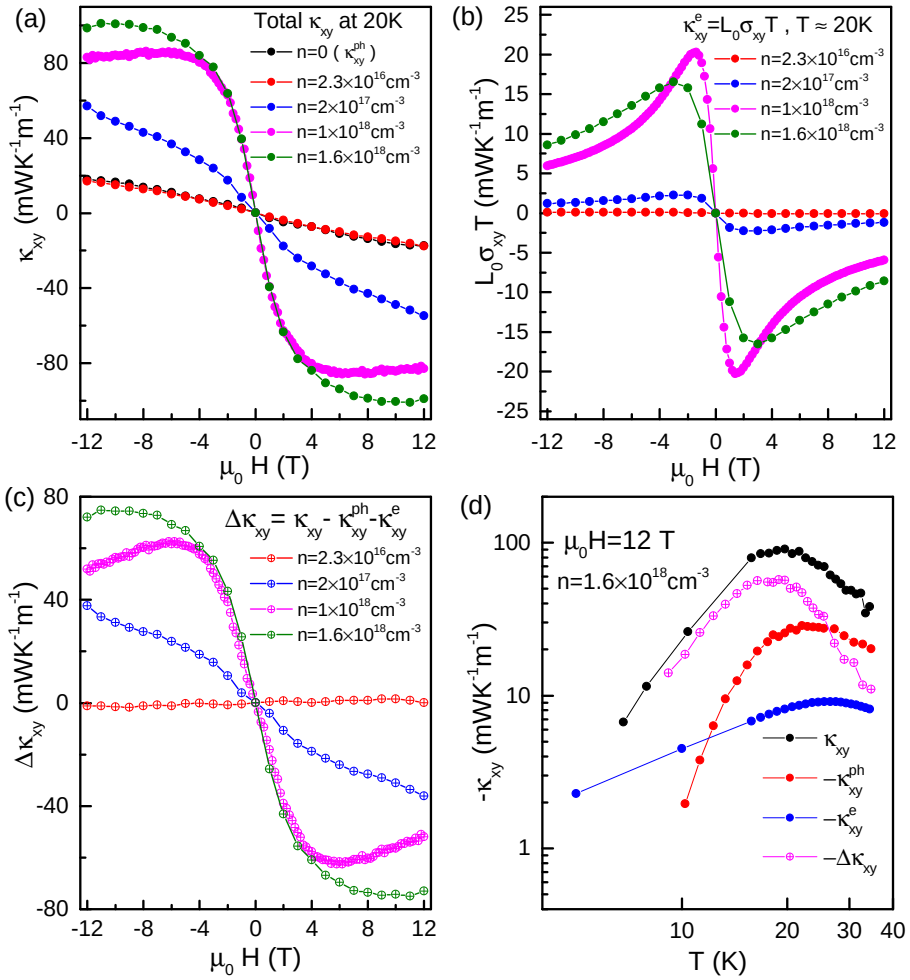

Fig. 3.9 *(a) κ_{xy} as a function of the magnetic field in samples with different carrier densities at 20 K. With growing metallicity, the amplitude of κ_{xy} increases and its field dependence becomes less linear. (b) Field dependence of the electrical Hall conductivity, σ_{xy}, multiplied by $L_0 = \frac{\pi^2}{3}\frac{k_B^2}{e^2}$, and the temperature, T, in the metallic samples. (c) Field dependence of the differential $\Delta\kappa_{xy} = \kappa_{xy} - \kappa_{xy}(n=0) - L_0\sigma_{xy}T$, which signals the presence of a third term in addition to the purely electronic and the purely phononic terms. (d) The evolution of κ_{xy} and its three components as a function of temperature. Below 25 K, $\Delta\kappa_{xy}$ is the largest component.*

fig3.8

without heat current ($\vec{J^Q}$=$\vec{0}$), and we call it the electric experiment. In both experiments, we measured the temperature difference and the electric field along x and y axes at the same time. Fig. 3.10 b,c and e,f show typical data for both configurations at T= 19.4 K for $SrTiO_{3-\delta}$ (n=1×10^{18} cm^{-3}).

In the first configuration ($\vec{J^Q} \neq 0$ and $\vec{J^e}$=$\vec{0}$), Eq.3.1 and Eq.3.2 become:

$$\overline{\sigma'}\vec{E_t} = \overline{\alpha}\nabla\vec{T_t} \qquad (3.5)$$

eq3.5

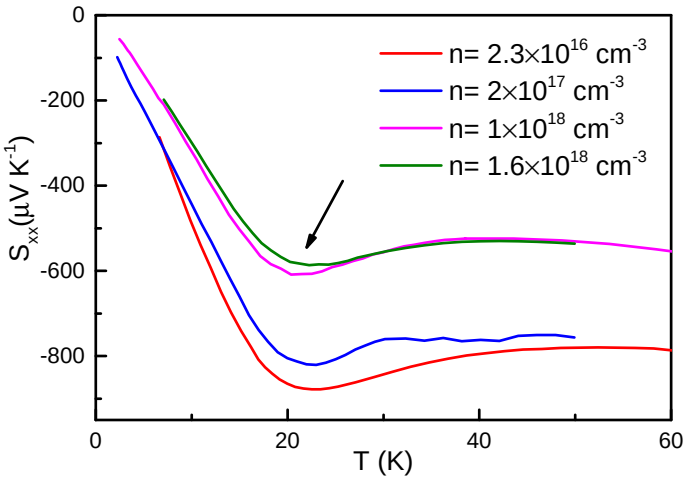

Fig. 3.10 *Seebeck coefficient (S_{xx}) as function of temperature for $SrTiO_{3-\delta}$ samples with different carrier concentrations. The arrow in (b) indicates the phonon drag peak.*

fig3.9

$$\vec{J^Q} = \overline{\alpha} T \vec{E_t} - \overline{\kappa'} \vec{\nabla T_t} \tag{3.6}$$

eq3.6

In the second configuration ($\vec{J^e} \neq 0$ and $\vec{J^Q}$=$\vec{0}$) Eq.3.1 and Eq.3.2 become:

$$\vec{J^e} = \overline{\sigma'} \vec{E_e} - \overline{\alpha} \vec{\nabla T_e} \tag{3.7}$$

eq3.7

$$\overline{\alpha} T \vec{E_e} = \overline{\kappa'} \vec{\nabla T_e} \tag{3.8}$$

eq3.8

The four equations 3.5, 3.6, 3.7 and 3.8 projected along the x and y directions give us eight equations to determine six unknown quantities, which are the two components of the three tensors: $\overline{\sigma'} = \begin{bmatrix} \sigma'_{xx} & \sigma'_{xy} \\ -\sigma'_{xy} & \sigma'_{xx} \end{bmatrix}$, $\overline{\alpha} = \begin{bmatrix} \alpha_{xx} & \alpha_{xy} \\ -\alpha_{xy} & \alpha_{xx} \end{bmatrix}$ and $\overline{\kappa'} = \begin{bmatrix} \kappa'_{xx} & \kappa'_{xy} \\ -\kappa'_{xy} & \kappa'_{xx} \end{bmatrix}$ assuming that they are isotropic in the xy plane. The redundancy allows us to make a check on self-consistency.

We calculated $\overline{\sigma'}$, $\overline{\alpha}$ and $\overline{\kappa'}$ in two different ways, leading to $\overline{\kappa'}_{1,2}$ and $\overline{\sigma'}_{1,2}$, where the index refers to the set of equations and experimental data used (see Fig 3.10 (g)). Here, we give explicit expressions for deriving $\overline{\sigma'_1}$ and $\overline{\kappa'_1}$.

Starting with Eq. 3.5 and 3.7 and setting $S = \sigma^{-1}\alpha$, we obtain :

$$S_{xx} = \frac{E_{tx}\nabla T_{tx} + E_{ty}\nabla T_{ty}}{\nabla T_{tx}^2 + \nabla T_{ty}^2}; S_{xy} = \frac{E_{tx}\nabla T_{ty} - E_{ty}\nabla T_{tx}}{\nabla T_{tx}^2 + \nabla T_{ty}^2} \tag{3.9}$$

eq3.9

$$\sigma'^{-1}_{1xx} = \frac{E_{ex} - (S_{xx}\nabla T_{ex} + S_{xy}\nabla T_{ey})}{J^e}; \sigma'^{-1}_{1xy} = \frac{E_{ey} - (-S_{xy}\nabla T_{ex} + S_{xx}\nabla T_{ey})}{-J^e} \tag{3.10}$$

eq3.10

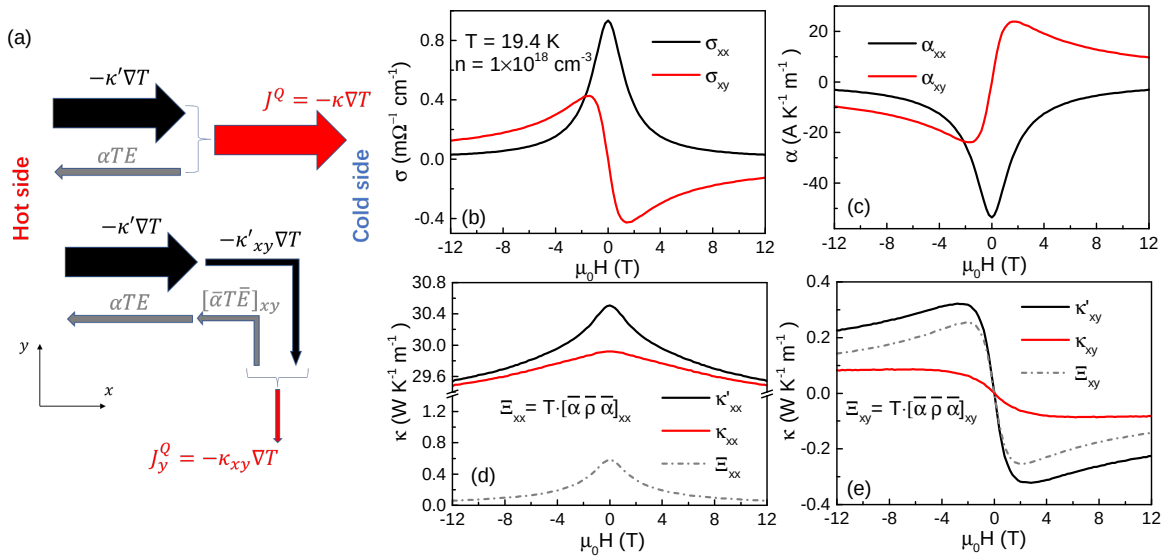

Fig. 3.11 *(a) The heat current density, $\vec{J^Q}$, consists of two terms in both longitudinal and transverse channels. The first component ($-\overline{\kappa'}\vec{\nabla T}$) represents the flow of entropy without particle flow. The second ($\overline{\alpha}T$) is the flow of entropy thanks to particle flow. The difference between κ and κ' is significant when the second term is not negligible. In our case, this happens for the transverse channel. The width of the arrows schematizes the weight of different components. (b) The longitudinal and the transverse electric conductivity as a function of the field at 20 K for $SrTiO_{3-\delta}$ (n=1 × $10^{18} cm^{-3}$).(c) The same for longitudinal and transverse thermoelectric conductivity. $\overline{\alpha} = \overline{\sigma}\,\overline{S}$. Note that the off-diagonal components rapidly become as large as the diagonal components. (d) κ_{xx} and κ'_{xx} as function of magnetic field. The difference is small. (e) κ_{xy}, κ'_{xy} as function of magnetic field. The difference is significant. Also shown in the panels are the diagonal and the off-diagonal components of the $\overline{\Xi} = \overline{\alpha}\,\overline{\rho}\,\overline{\alpha}\,T$ tensor, which quantifies the correction.*

fig3.10

$$\alpha_{1xx} = \sigma'_{1xx}S_{xx} - \sigma'_{1xy}S_{xy}; \alpha_{1xy} = \sigma'_{1xx}S_{xy} + \sigma'_{1xy}S_{xx} \tag{3.11}$$

eq3.11

Injecting α into Eq. 3.6, we get $\overline{\kappa'_1}$

$$\kappa'_{1xx} = \frac{[T\cdot(\alpha_{1xx}E_{tx} + \alpha_{1xy}E_{ty}) - J^Q]\cdot -\nabla T_{tx} - T\cdot(-\alpha_{1xy}E_{tx} + \alpha_{1xx}E_{ty})\cdot\nabla T_{ty}}{-\nabla T^2_{tx} - \nabla T^2_{ty}} \tag{3.12}$$

eq3.12

$$\kappa'_{1xy} = \frac{T\cdot(-\alpha_{1xy}E_{tx} + \alpha_{1xx}E_{ty})\cdot\nabla T_{tx} - [T\cdot(\alpha_{1xx}E_{tx} + \alpha_{1xy}E_{ty}) - J^Q]\cdot -\nabla T_{ty}}{-\nabla T^2_{tx} - \nabla T^2_{ty}} \tag{3.13}$$

eq3.13

Method 2 starts with Eq. 3.6 and 3.8 and leads to σ'_2, α_2 and κ'_2. Figure 3.13 compares the results of the two methods. Onsager reciprocity implies no difference because of the identity between the components of the thermoelectric tensor in the two Eq.3.1 and 3.2.

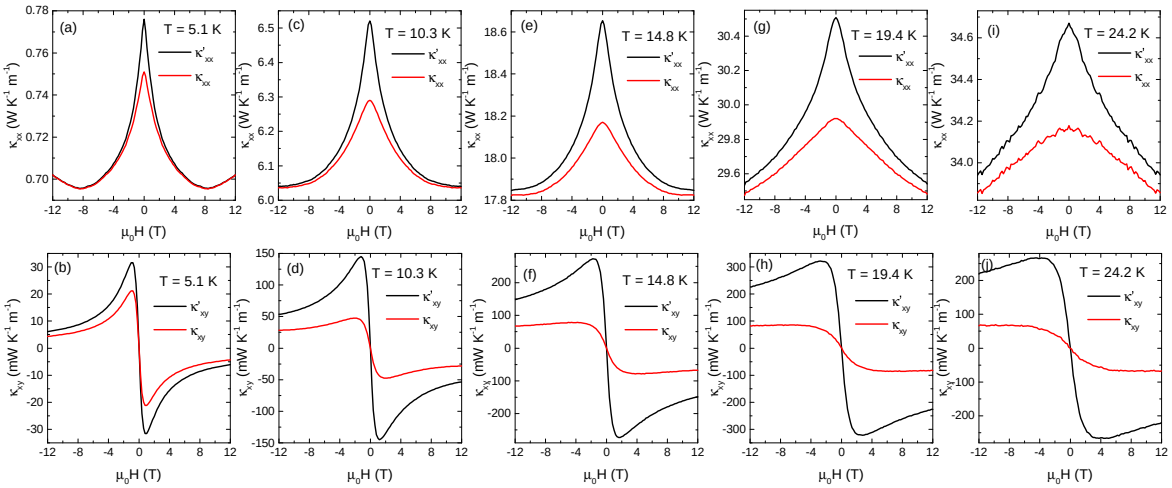

Fig. 3.12 *(a)-(e) Field dependence of κ_{xx} and κ'_{xx} for different temperature in $SrTiO_{3-\delta}$ (n=1×10^{18} cm^{-3}). (f)-(j) Same as (a)-(e) for κ_{xy} and κ'_{xy}.*

fig3.11

Experimentally, we find that this is indeed the case: $\sigma'_{1ij} = \sigma'_{2ij}$; $\alpha'_{1ij} = \alpha'_{2ij}$ and $\kappa'_{1ij} = \kappa'_{2ij}$. Here, i and j refer to x and y orientations and 1 and 2 refer to method 1 and method 2.

Then we compared the $\overline{\sigma'}$ with $\overline{\sigma}$, there is no difference in both longitudinal and transverse channels. While the $\overline{\kappa'}$ and $\overline{\kappa}$ show obvious differences especially in the transverse channel as shown in Fig 3.14 somehow it related to the large thermoelectric conductivity $\overline{\alpha}$ especially in the transverse channel.

3.4.4 Thermal Hall effect enhancement due to electron-phonon drag in lightly doped Strontium Titanate

In this section, I will present a scenario to explain the extra contribution to κ_{xy} that we have identified. Our scenario invokes three different features of lightly doped strontium titanate :

- The first is that momentum exchange between phonons and electrons is frequent. Since both the Fermi radius and the phonon thermal wavelength (at our temperature range of interest) are much smaller than the width of the Brillouin zone, such collisions are not Umklapp and conserve momentum.

- The second feature is that heat is mainly carried by phonons (and not by electrons), $\kappa^e_{xx} \ll \kappa^{ph}_{xx}$, see Fig 3.15 a).

- The Third is that the Hall angle of electrons exceeds by far the (thermal) Hall angle of phonons. As one can see in Fig 3.15 b, the phonon thermal Hall angle is 3 orders of magnitude smaller than the electric Hall angle. Lightly-doped strontium titanate is a dilute metal with highly mobile carriers. A moderate magnetic field puts the system in the high field limit, where $\mu B \gg 1$ [127]

The combination of these three features generates an additional thermal Hall response where the longitudinal energy flow, mostly carried by phonons, is accompanied by a flow of

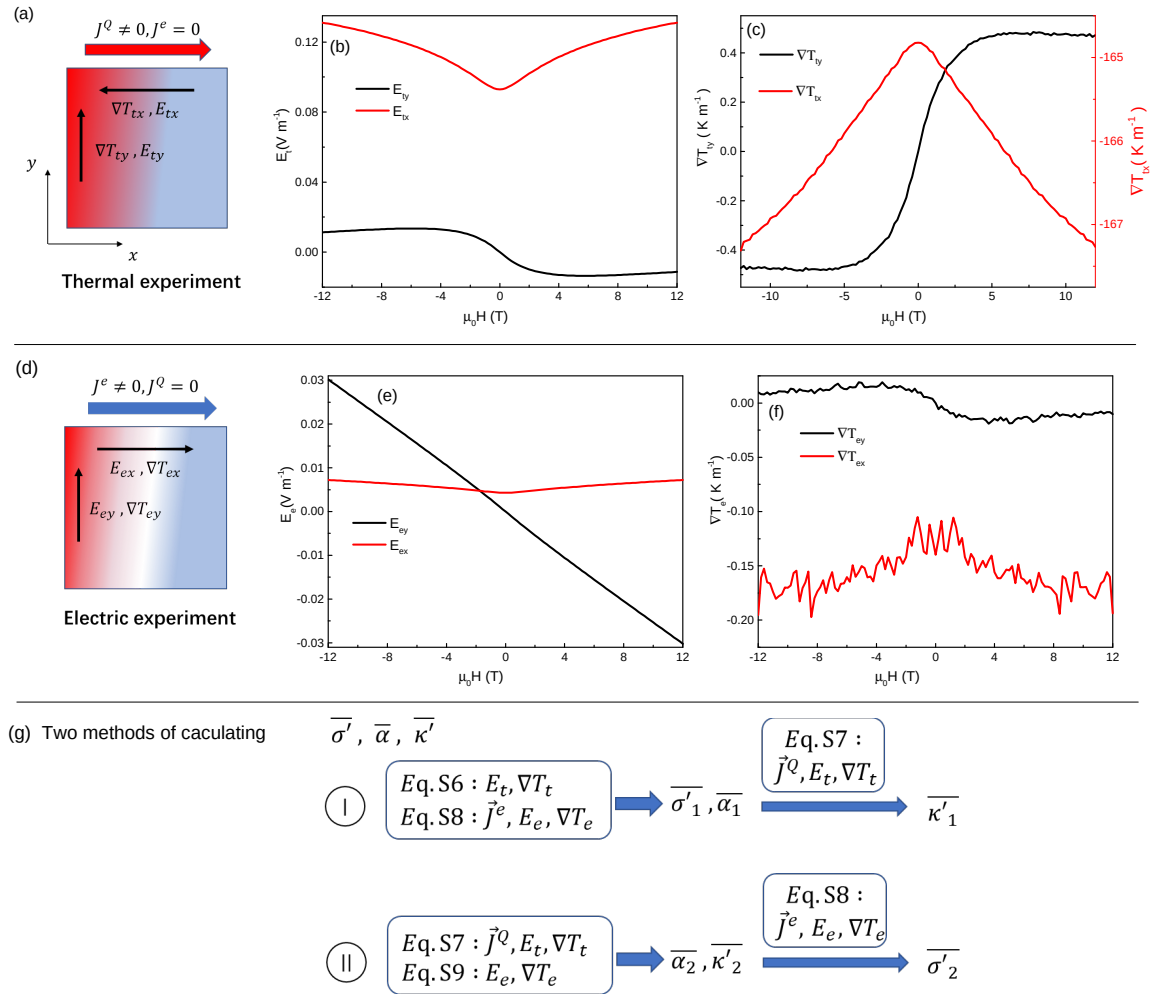

Fig. 3.13 *(a)The first configuration of thermal experiment. (b) Electrical field and (c) thermal gradient measured in* $SrTiO_{3-\delta}$ *(n=1×10*^{18} *cm*$^{-3}$*) at T = 19.4 K in the thermal experiment (*$\vec{J^Q} \neq \vec{0}$ *and* $\vec{J^e}=\vec{0}$*). (d)The second configuration of the electric experiment. (e) and (f) same as (b) and (c) in the electric experiment (*$\vec{J^e} \neq 0$ *and* $\vec{J^Q}=\vec{0}$*).(g) Two methods by combining the two configurations to calculate* $\overline{\sigma'}$, $\overline{\kappa'}$ *and* $\overline{\alpha}$.

fig3.12

electrons and its unavoidable transverse counterpart, which ends up by triggering a phononic transverse flow.

3.4.4.1 Phonon drag effect in lightly doped $SrTiO_3$

Momentum exchange between electrons and phonons (in the presence of heat flow and in the absence of charge current) is known as phonon drag [128; 129]. It is known to amplify the thermoelectric response, mostly in semiconductors [128], but also in metals [130]. In the case of strontium titanate, previous studies [131; 132] have shown that phonon drag causes

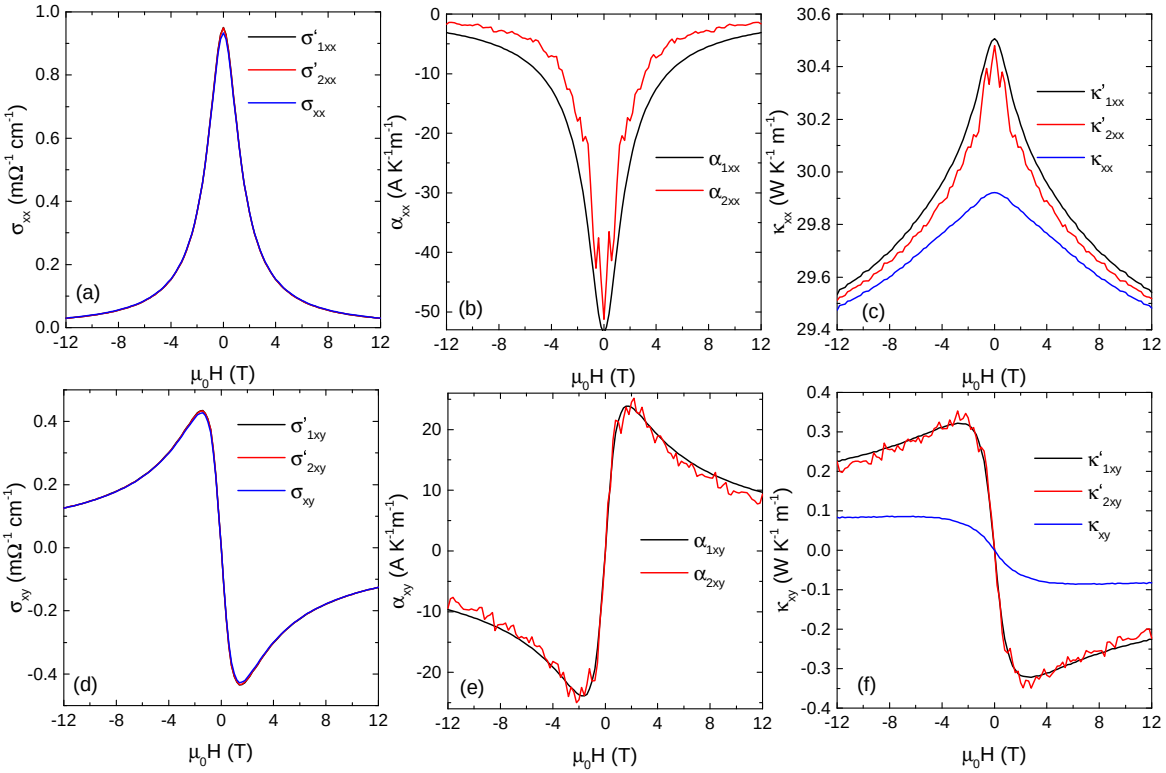

Fig. 3.14 *(a)-(c) Longitudinal electric (σ_{xx}), thermoelectric (α_{xx}) and thermal conductivity (κ_{xx}) as a function of field at $T = 19.4$ K for $SrTiO_{3-\delta}$ ($n = 1{\times}10^{18}$ cm^{-3}). The black and red colors correspond to two different combinations of Eq. 3.5, 3.6, 3.7, and 3.8. Black (red) line results were obtained using Eq. 3.5(3.6) 3.6(3.7) and 3.7(3.8). (d)-(f) same as (a)-(c) but for the transverse components of $\overline{\sigma'}$, $\overline{\alpha}$ and $\overline{\kappa'}$.*

fig3.13

a peak in the zero-field Seebeck coefficient around ~ 20 K. We confirmed the presence of such a peak in our samples (See Fig 3.10). Before quantifying the expected contribution of phonon drag to transverse thermal transport conductivity, let's first estimate the amplitude of the phonon drag term in the Seebeck effect.

The thermal power Fig. 3.16 (a) compares the temperature dependence of S_{xx}/T in doped sample ($n = 1 \times 10^{18}$ cm^{-3}) with previous measurements [77; 131]. Sub-kelvin measurements have shown that S_{xx}/T becomes flat at low temperatures (see Fig. 3.16 (a)) with the expected amplitude for the diffusive response of a degenerate semiconductor with an energy-independent mean free path [77] :

$$\left|\frac{S}{T}\right| = \frac{\pi^2}{3}\frac{k_B}{e}\frac{1}{T_F} \tag{3.14}$$

eq3.14

T_F is the Fermi temperature, which can be deduced from quantum oscillations. Using Eq.3.14 we estimate the amplitude of the diffusive response in our sample with $n = 1 \times 10^{18} cm^{-3}$ to be in the range of $-15 \sim -23$ $\mu V K^{-2}$. On top of it, there is a second contribution, the phonon drag (labeled S_{drag}), shown in gray in Fig.3.16b). S_{drag} peaks around

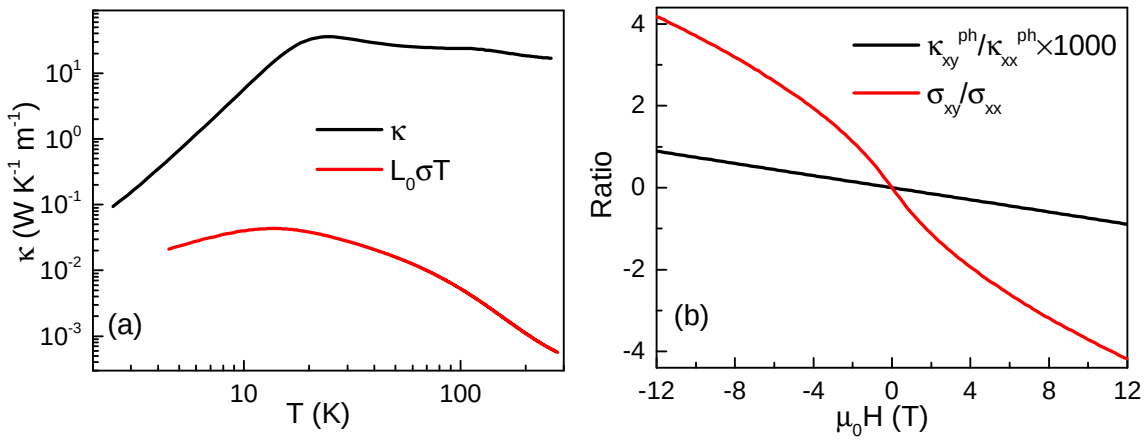

Fig. 3.15 *(a) Thermal conductivity (κ_{xx}) of $SrTiO_{3-\delta}$ ($n = 1 \times 10^{18} cm^{-3}$) as function of temperature and its electronic component ($L_0\sigma T$). Phonons are by far the dominant carriers of heat. (b) The phonon thermal and the electronic Hall angles as the function of field at T= 20 K. The former is three orders of magnitude smaller than the latter.*

fig3.14

20 K, in good agreement with previous work [131]. A similar phonon drag contribution is also detected in the Nernst effect ($S_{xy} = \frac{E_y}{\Delta T_x}$) see Fig. 3.16 (c).

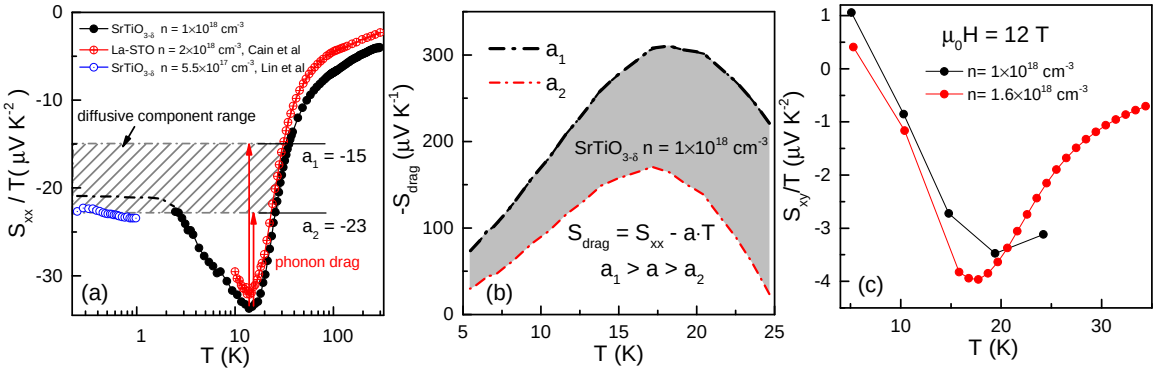

Fig. 3.16 *(a) Temperature dependence of S_{xx}/T in $SrTiO_{3-\delta}$ for n=1× 10^{18} cm^{-3} compared with previous works [77; 131]. The hatched area is the estimated diffusive contribution using Eq.3.14. (b) The amplitude of the phonon drag contribution of S_{xx} (gray area) as a function of the temperature. $S_{drag} = S_{xx} - a \cdot T$ where $a \cdot T$ is the diffusive contribution shown in (a).(c) Temperature dependence of S_{xy}/T at B= 12 T for n=1× 10^{18} cm^{-3} and 1.6× 10^{18} cm^{-3}. A phonon drag contribution leads to a peaks in S_{xy} around 20 K.*

fig3.15

3.4.4.2 From Phonon drag to thermal Hall effect

Let's now see how the phonon drag combined with the large Hall angle of lightly doped $SrTiO_3$ can give rise to an enhanced thermal Hall effect. Phonons streaming from hot to cold

exert a drag on the charge carriers. To quantify this effect, Herring considered an equivalent phenomenon: the enhancement in the Peltier coefficient of an isothermal sample caused by the drag exerted on phonons by the electric current [128]. Assuming an approximate proportionality between heat current and crystal momentum, he found that a phonon drag Peltier effect, Π_{drag}, of either sign can arise :

$$\Pi_{drag} = \pm \frac{m^* v_s^2}{e} f \frac{\tau_p}{\tau_e} \tag{3.15}$$ eq3.15

Here, m^* is the effective mass of electrons, v_s is the sound velocity, e is the fundamental charge, τ_p and τ_e are respectively, the phonon and the electron scattering times and $0 < f < 1$ represents the fraction of collisions suffered by phonons, which leads to momentum exchange between the phonon bath and the electron bath. Using the Kelvin relation, the phonon drag component of the Seebeck coefficient becomes Π_{drag}/T. To derive Eq. 3.15, Herring put forward two arguments. First of all the energy density flux, J^Q, can be approximated by the product of the crystal momentum per unit volume, P and the square of sound velocity, v_s:

$$J^Q = P v_s^2 \tag{3.16}$$ eq3.16

The second argument is that the rate at which phonons receive crystal momentum from the electronic carriers is to be balanced with the rate at which they lose it. Therefore:

$$\frac{P}{\tau_p} = \pm f n e E \tag{3.17}$$ eq3.17

Here, n is the carrier concentration, and E is the electric field. The loss of crystal momentum out of the phonon bath is countered by what electrons are introduced to this bath. The parameter f is a measure of the efficiency of momentum flow between the phonon and electron baths. Herring invoked a 'hydraulic analogy' where momentum first flows from electrons to small q phonons and then is distributed among phonons and then eventually lost. In this analogy, f plays the role of a half-open valve. Eq.3.15 can be obtained from Eq.3.16 and Eq.3.17, using the Drude link between the electric field and the electric current ($J^e = \frac{ne^2\tau_e}{m^*} E$).

Let us now consider the twist brought by a large Hall angle to this picture. The Peltier phonon drag implies that an electric current can lead to a phonon energy flow (Fig. 3.17a). A finite THE driven by phonon drag can be explained in the following way. A finite off-diagonal thermoelectric conductivity implies that a longitudinal (transverse) thermal gradient will generate a transverse (longitudinal) electric current. Then, this electric current, following Herring's original picture, will generate a thermal current. The latter will be perpendicular to the thermal gradient (Fig. 3.17b). Therefore, the overall magnitude of this phonon drag THE will be given by the product of the off-diagonal thermoelectric conductivity, α_{xy}, and Herring's expression for Peltier phonon drag:

$$\kappa_{xy}(drag) = -\alpha_{xy} \frac{m^* v_s^2}{e} f \frac{\tau_p}{\tau_e} \tag{3.18}$$ eq3.18

Thus, the component of thermal Hall conductivity generated by mutual drag between electrons and phonons is proportional to the product of α_{xy}, the ratio of phonon and electron scattering times $\frac{\tau_p}{\tau_e}$ and the efficiency of momentum transfer between the two baths,

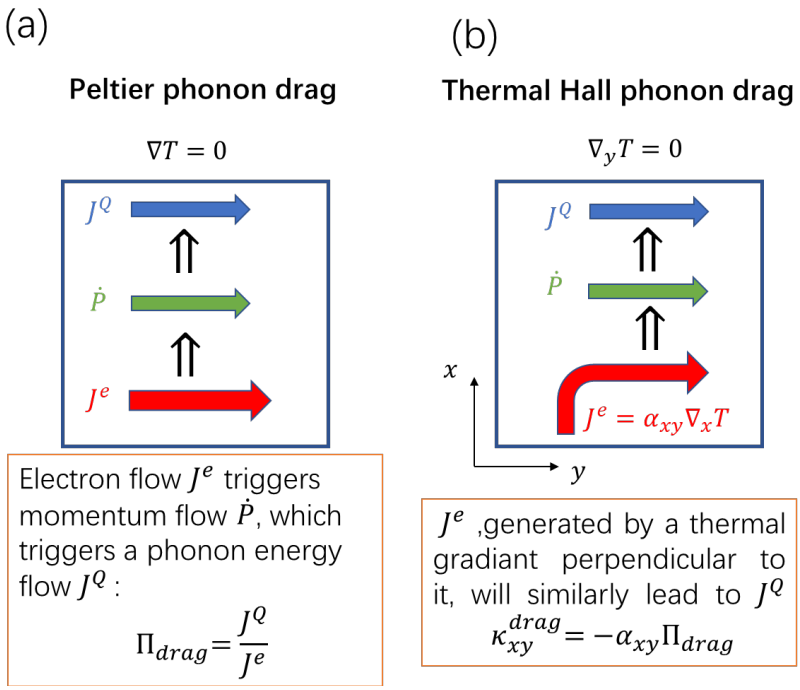

Fig. 3.17 ***From phonon drag to thermal Hall conductivity:*** *(a) Herring's picture of phonon drag in an isothermal sample. Electronic momentum flow generates a phonon momentum flow which in turn leads to a phonon heat flow. The amplitude of this Peltier effect sets the amplitude of the phonon drag Seebeck effect. (b) Replacing the electronic charge current with a finite longitudinal thermal gradient multiplied by off-diagonal thermoelectric conductivity quantifies the amplitude of the phonon drag thermal Hall effect.*

fig3.16

parametrized by f. Let us also note the presence of mv_s^2. This is the kinetic energy of an electron drifting with the velocity of sound, a less familiar energy scale emerging when electrons and phonons couple to each other [133].

3.4.4.3 Comparison of our model with the experimental data

We proceed now to compare $\Delta\kappa_{xy}$ resolved by experiment, with $\kappa_{xy}(drag)$, expected by Eq.3.18. With the exception of f, all terms of Eq.3.18 are experimentally accessible. The sound velocity is $v_s = 7.8km/s$ [134], the effective mass of electrons is $m^\star = 1.8m_e$ [77]. τ_p can be extracted from phonon thermal conductivity and τ_e from the electrical conductivity.

Fig. 3.18a shows the non-monotonous field dependence of $\kappa_{xy}(drag)$, which mirrors the field dependence of α_{xy} (Fig. 3.18b), which, after an initial increase, steadily decreases in the high-field regime. Since $S_{xx} > S_{xy}$ and $\sigma_{xy} \geq \sigma_{xx}$, $\alpha_{xy} \simeq S_{xx}\sigma_{xy}$ and the field dependence of α_{xy}, is similar to the field dependence of Hall conductivity, which steadily decreases in the high-field regime ($\sigma_{xy}(B \longrightarrow \infty) \longrightarrow 0$).

The ratio of τ_p/τ_e, shown in Fig. 3.18c, is much larger than unity and steadily increases with a magnetic field. This is because, as previously documented [127], the mobility of

electrons diminishes with a magnetic field, presumably because partially extended disorder becomes more effective in scattering electrons with increasing magnetic field which confines the electron wave function. The phonon scattering time on the other hand is barely affected by magnetic field.

By assuming equality between $\Delta\kappa_{xy}$ and $\kappa_{xy}(drag)$ and using Eq. 3.18, we can extract f. The results are shown in Fig. 3.18d. We find that $f < 1$, attesting the soundness of our approach. The efficiency of momentum transfer between phonons and electrons is close to 1 at the peak temperature and steadily decreases with temperature. As the temperature decreases, the relative frequency of electron-phonon scattering events decreases. We also note that a strong coupling between electrons and soft ferroelectric phonons has been invoked [135; 136] to explain the transport properties of metallic STO [83; 132]. The steady field-induced decrease in f indicates that the efficiency of the momentum transfer between phonons and electrons decreases with the decrease in the electronic scattering time and the growing mismatch between the phonon and the electron scattering time.

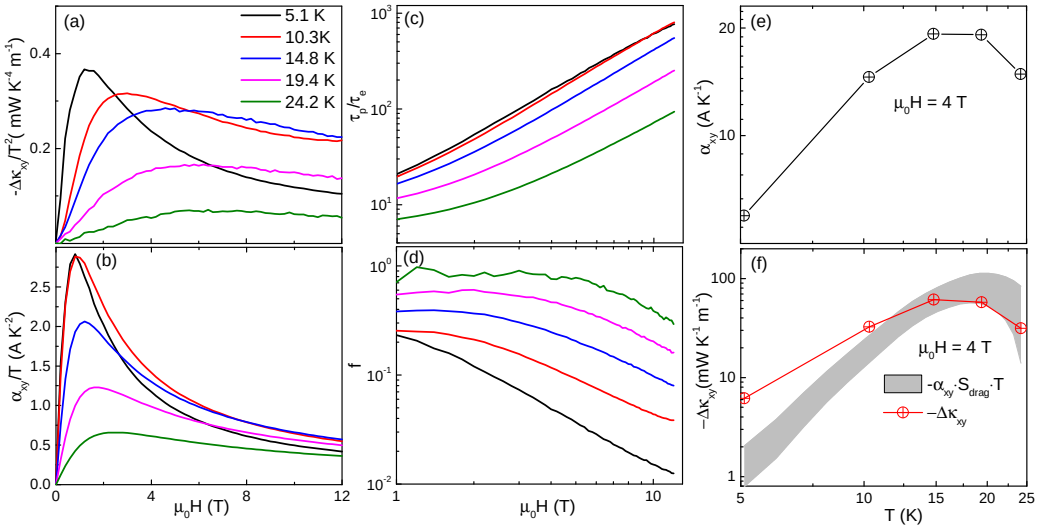

Fig. 3.18 ***Quantitative analysis of $\Delta\kappa_{xy}$:*** *(a) Field dependence of $\Delta\kappa_{xy}/T^3$ at different temperatures. (b) Field dependence of α_{xy}/T at different temperatures. In our picture, this is the main driver of the field dependence of $\Delta\kappa_{xy}$ (c) Field dependence of the ratio of the phonon to electron scattering time, extracted from electric and thermal conductivity data. Note that $\tau_P \gg \tau_e$ and the ratio enhances with a magnetic field. (d) The field dependence of f, obtained by equating $\Delta\kappa_{xy}$ and $\kappa_{xy}(drag)$ given by Eq. 3.18. (e), The temperature dependence of α_{xy} at 4 T. (f) The temperature dependence of $-\Delta\kappa_{xy}$ and $-\alpha_{xy}S_{drag}\cdot T$. The width of the latter represents the uncertainty in separating the phonon-drag and the diffusive components of the Seebeck coefficient (see Fig 3.16).*

fig3.17

The soundness of our diagnostic can be checked by comparing the extra thermal Hall effect and the phonon drag Seebeck effect, supposed to share the same origin. Both effects, measured by distinct experiments, peak around 20 K. Their amplitude match too. Eq.3.15 and Eq.3.18 together with the Kelvin relation ($\Pi = ST$) and the identification of $\Delta\kappa_{xy}$ with $\kappa_{xy}(drag)$ implies an equality between the two extracted quantities: $\Delta\kappa_{xy} \approx -\alpha_{xy}S_{drag}T$.

Fig. 3.18 f compares $\Delta\kappa_{xy}$ and $-\alpha_{xy} \cdot S_{drag} \cdot T$ as a function of temperature at 4 T. The agreement between 25 K down to 10 K confirms the quantitative self-consistency of the data. The disagreement at 5 K indicates the limits of our approximations when f strongly varies with a magnetic field.

3.4.5 Electron-phonon drag THE in other metallic solids

Our result implies that the combination of phonon-drag (frequently encountered in semiconductors) and a sizeable transverse thermoelectric conductivity, α_{xy} (known to become large when the carrier density is low density and carrier mobility is high [137]) can give rise to a phonon-drag THE. These conditions can be formulated in terms of a hierarchy of time scales. The scattering time of phonons should exceed the scattering time of electrons and the latter should in turn exceed the inverse of the cyclotron frequency, in order to ensure longitudinal-to-transverse conversion. Thus, a sizeable phonon drags THE requires:

$$\tau_p > \tau_e > \omega_c^{-1} \tag{3.19}$$ eq3.19

The second condition is that the rate of momentum lost by phonons is to be comparable to the rate of phonon-electron exchange :

$$f \gg 0 \tag{3.20}$$ eq3.20

Note that the latter condition can only be satisfied at finite temperatures. The hydrodynamic window, identified by Gurzhi [36] requires a hierarchy of time scales too: The momentum-conserving scattering time should outweigh the boundary scattering time, itself larger than the momentum-relaxing scattering time. As a result, hydrodynamic features are expected in a limited temperature window and in a limited number of materials.

Inequalities 3.19 and 3.20 specify the conditions for expecting a phonon drag THE. Long τ_p is expected in a crystal at low temperature when phonon wavelength is long and point defects cannot scatter them. In many dilute metals, when the Bohr radius of the semiconducting parent is long [24] carriers are more mobile than in metallic silicon. As a consequence, the inequality $\tau_e > \omega_c^{-1}$ is easily satisfied at low fields. If electron-phonon momentum exchange happens to be frequent too, then an effect similar to the one observed here is expected. Possible candidates are Bi_2Se_3 [138], InAs [139], PbTe [140] and their sister compounds. It is not surprising that the thermal Hall effect in metallic cuprates is not detectably amplified by phonon drag [93]. In their case the mobility of carriers in cuprates is low and, as a consequence, condition 3.19 is not satisfied. Indeed, the measured Hall angle in $La_{1-x}Sr_xCuO_4$ is quite small. At B=10 T, $\sigma_{xy}/\sigma_{xx} \ll 0.1$ [141] and therefore $\omega_c\tau_e < 1$.

3.5 Conclusion

In this chapter, we show that the amplitude of the phonon THE in strontium titanate drastically varies with atomic substitution. First, it is suppressed by a tiny substitution of Ca on Sr which stabilizes the ferroelectric order. This result shows that ferroelectric fluctuation is a key ingredient to the phonon THE of STO. Second, it is enhanced by oxygen vacancies and the emergence of dilute metalicity. We show that this enhancement is an

unexpected consequence of the phonon drag in the presence of a large Hall angle. The coupling between two types of heat carriers, one with a long scattering time (here phonons) and another with a large Hall angle (here electrons) can be studied in other contexts such as insulating solid with ordinary phonons (with a long scattering time) and magnetic excitations a short scattering time and a large transverse response.

Chapter 4

Electronic thermal transport in metallic STO

Summary of the Chapter

Quadratic temperature dependent (T-square) electrical resistivity is a hallmark of Fermi-liquid. Momentum dissipation as a result of the collision between electrons is either associated with Umklapp scattering or with the Baber mechanism. These two momentum-relaxing mechanisms are known to generate a T-square electronic thermal resistivity. However, the discovery of a persistent T-square resistivity in the dilute regime of metallic $SrTiO_3$ ($n \simeq 10^{17}$ cm^{-3}) where none of these two mechanisms operates, has provided a new perspective on the origin of T-square resistivity observed in many metals. There has been no relevant study of the temperature-dependence of electronic thermal conductivity in dilute metallic $SrTiO_3$. Motivated by the observation of a T-square thermal resistivity in the ^{3}He Fermi liquid without Umklapp scattering, We studied thermal transport in two samples of $SrTi_{1-x}Nb_xO_3$. By applying a magnetic field, we succeeded in extracting the electronic thermal conductivity. Comparing our results with other Fermi liquids, especially ^{3}He, I will discuss the possible origins of the T-square electrical and electronic thermal resistivity.

The content of this chapter is based on the paper published in S. Jiang et al., Phys. Rev. Lett. 131, 016301 [142].

4.1 T-square resistivity in two dilute metals

Landau and Pomeranchuk [143], and contemporaneously Baber [16] postulated that electron-electron collisions cause a quadratic temperature dependence in the electrical resistivity of metals. Subsequent experiments found that this is prominent in metals hosting strongly-correlated electrons (such as UPt_3 [144] or strontium titanate [145]), but also those with a small carrier concentration (like bismuth [146] and graphite [147]). In these cases, at sufficiently low temperatures, resistivity, ρ, can be expressed as :

$$\rho = \rho_0 + AT^2 \tag{4.1}$$ eq4.1

Here, ρ_0 is the residual resistivity, which depends on the disorder. The prefactor, A, on the other hand, is intrinsic to each metal. The ubiquity of equation 4.1 across various families of Fermi liquids raises two questions: 1) What makes the exchange of momentum between two colliding electrons detrimental to electrical conduction? 2) What sets the amplitude of A?

The two identified answers to the first question are Umklapp and the Baber mechanism. An Umklapp event occurs when the momentum vector sum of the colliding electrons gets out of the Brillouin zone, leading to a loss of momentum equivalent to one reciprocal unit vector [14; 31]. The Baber mechanism [16] refers to the existence of two distinct electron reservoirs whose momentum exchange is a bottleneck in the path of momentum leak from the electron bath to the phonon bath. The second question was addressed first by Rice [17] in seven elemental transition metals and then by Kadowaki and Woods in Heavy-fermion metals [84] (See also [148; 149]) who argued that the amplitude of A scales with the square of the T-linear specific heat, γ^2 called Kadowaki-Woods(KW) scaling, because both depend on the density of states. The KW scaling fails when considering the semi-metals(Bi, C, Sb) because thousands of atoms share a single electron, and the low carrier density pulls down the magnitude of γ. As we know the phase space for collisions between two electrons is proportional to $(\frac{k_B T}{E_F})^2$, the standard KW scaling becomes $A \propto E_F^{-2}$ and A can be written as

$$A = \frac{\hbar}{e^2}(\frac{K_B}{E_F})^2 l_{quad} \tag{4.2}$$ eq4.2

Here l_{quad} is a material-dependent length scale that can be set by the Fermi wavelength of electrons, the interatomic distance, or a combination of both.

In Fig 4.1, the amplitude of A in several families of Fermi liquids is plotted as a function of the Fermi temperature. In this plot, the Kadowaki–Woods bound and the Rice bound appear as bounds to l_{quad} (≈ 40 and ≈ 1.6 nm. Dilute metallic STO whose carrier density varies from $10^{21} cm^{-3}$ to $10^{17} cm^{-3}$ displayed in Fig 4.1 (a) and (b) is in this range.

However, none of the two referred mechanisms works in STO because its Fermi surface is too small to allow Umklapp scattering and it consists of a single pocket with carrier density below $10^{18} cm^{-3}$ [5; 77; 78].

Following this observation, two theoretical studies [135; 136] showed that the temperature dependence of electrical resistivity in STO one can be explained with a scenario based on the scattering of electrons by two soft transverse optical (TO) phonons. This would account for the persistence of T-square resistivity above the degeneracy temperature. On the other hand, low-temperature T-square resistivity (well below the minimum energy of TO phonons) remained a mystery. Another development was the discovery of T-square resistivity in dilute metallic Bi_2O_2Se [20], with a small single Fermi surface and without any soft phonon mode. The T-square prefactor was found to scale with the Fermi energy as shown in Fig 4.1 (b). This demonstrated that STO is not an isolated case and called for an e-e scattering scenario in the absence of Umklapp.

In fact that the phase space for electron–electron scattering growing quadratically with temperature also has a signature in thermal transport. Defining the electronic thermal resistivity as $WT = T/\kappa^e$, one expects:

$$WT = (WT)_0 + BT^2 \tag{4.3}$$ eq4.3

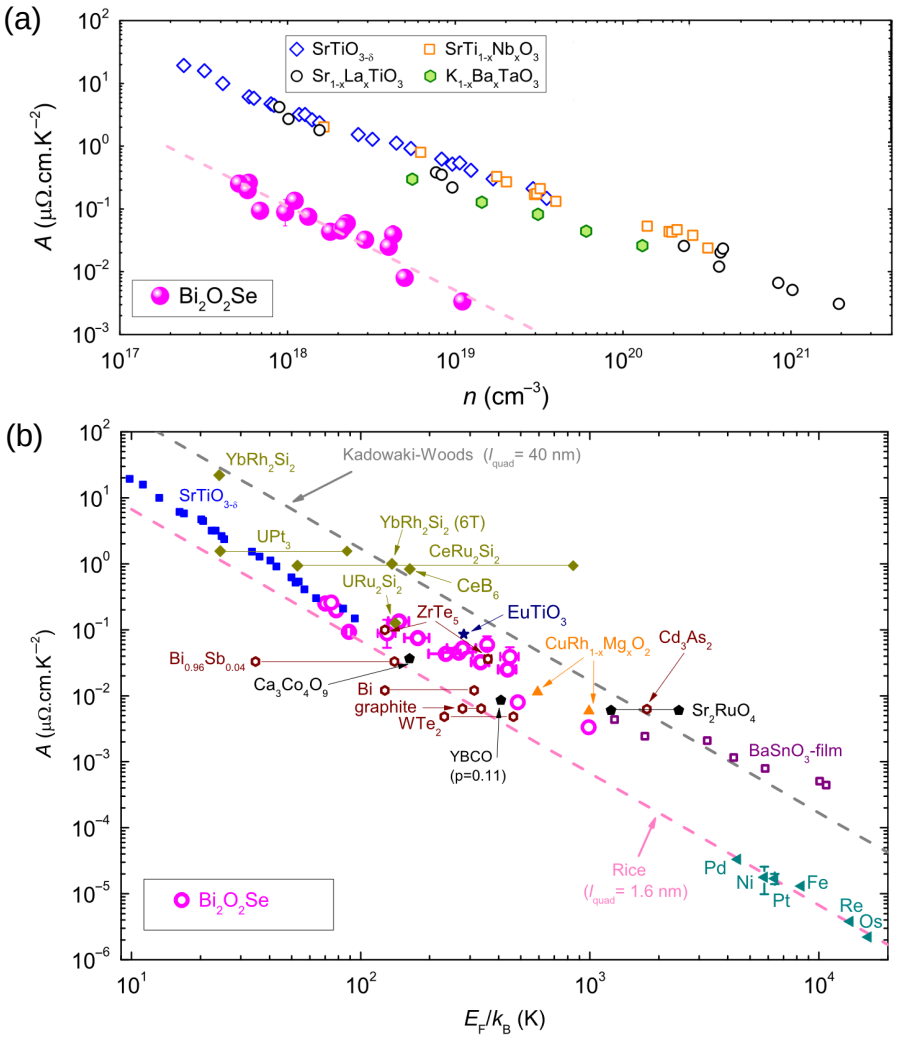

Fig. 4.1 *(a) The slope of T^2 resistivity (A) as a function of n for Bi_2O_2Se: compared with doped $SrTiO_3$ and other correlated or dilute metals. Most of the data are bounded by the two dashed lines set by Kadowaki–Woods and Rice, corresponding to a material-dependent length scale l_{quad} of 40 and 1.6 nm, respectively [20].*

fig4.1

here, $(WT)_0$ is the residual thermal resistivity, expected to obey the Wiedemann Franz (WF) law: $L_0(WT)_0 = \rho_0$ with $L_0 = \frac{\pi^2}{3}\frac{k_B^2}{e^2} = 2.44 \times 10^{-8} V^2 K^{-2}$. On the other hand, $L_0 B > A$, because, compared to energy flow, momentum flow is less affected by small-angle scattering [29; 150]. Experiments on various metals, including Ni [151], Al [152], W[153], Sb [154], $CeRhIn_5$ [155], WP_2 [156], UPt_3 [157]) have confirmed both these expectations. Then we turn our sight to the thermal transport of electrons in the dilute metal STO.

4.2 Electronic thermal conductivity in $SrTi_{1-x}Nb_xO_3$

In Fermi liquids with low carrier density, phonon becomes the dominant heat carrier. It is also the case for metallic STO. Moreover, the thermoelectric effect and electron-phonon interaction will also have an effect on its thermal transport. All of these make it difficult to acquire electronic thermal conductivity in experiments. Here we studied thermal transport in two $SrTi_{1-x}Nb_xO_3$ samples, by using the magnetic field succeeded in extracting the electronic thermal conductivity.

4.2.1 Samples

$SrTi_{1-x}Nb_xO_3$ crystals were commercially provided by SurfaceNet GmbH. The nominal Nb content for sample #1 is 1 $wt\%$(weight percent) and sample #2 is 0.5 $wt\%$. The expected carrier concentration for #1 and #2 is $3.3\times10^{20}cm^{-3}$ and $1.7\times10^{20}cm^{-3}$ (one Nb substitutes one Ti will provide one electron). We also acquired their carrier concentration by measuring the Hall coefficient in 2 K and for #1 $n_H = 3.1 \times 10^{20}cm^{-3}$(for #2 $n_H = 1.8 \times 10^{20}cm^{-3}$) which is in good agreement with the expected value.

4.2.1.1 Resistivity and thermal conductivity

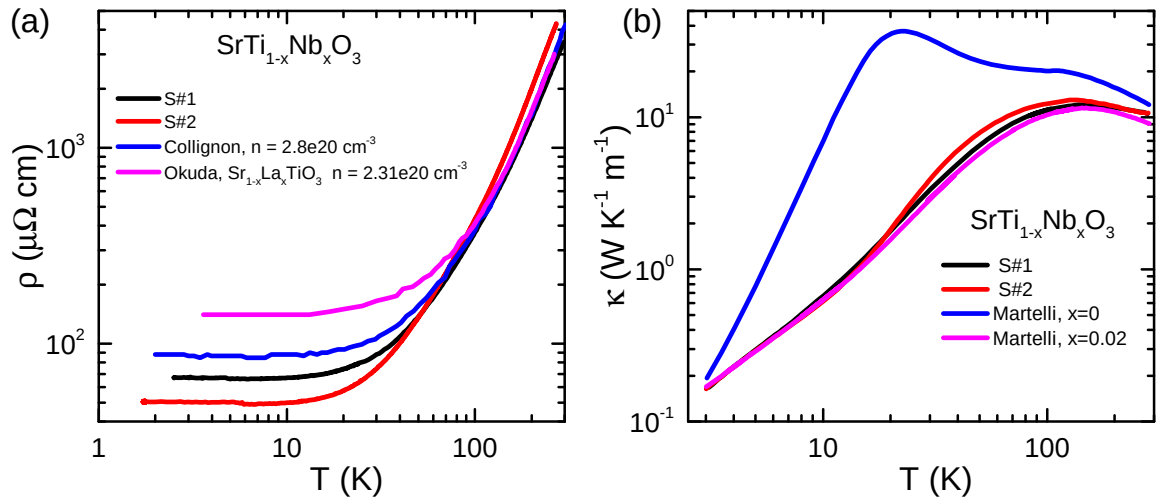

Fig. 4.2 *Electrical resistivity (a) and thermal conductivity (b) of the samples used in this study.*

fig4.2

We compare the temperature-dependence of their resistivity with previous data on $SrTi_{1-x}Nb_xO_3$ [123; 132; 158] and $Sr_{1-x}La_xTiO_3$ [158] at similar carrier doping levels as shown in Fig 4.2 (a). Above 100 K, the resistivity of samples with the same carrier concentration is very similar. Below 80 K, they show different residual resistivities. Our samples tend to display a comparatively lower residual resistivity. Fig 4.2 (b) compares the temperature dependence of their thermal conductivity with previous reports on pristine STO and $SrTi_{1-x}Nb_xO_3$ with $x = 0.02$ (correspond to 1 $wt\%$). The large suppression of thermal conductivity by Nb doping below 100 K is not due to the electron contribution but to the

decrease of the phonon thermal conductivity. The random distribution of Nb atoms introduces additional scattering processes that decrease the phonon mean free path. This reduced phonon contribution makes the extraction of the electronic thermal conductivity easier than in low-doped $SrTiO_{3-\delta}$.

4.2.1.2 Thermal conductivity influenced by thermoelectricity

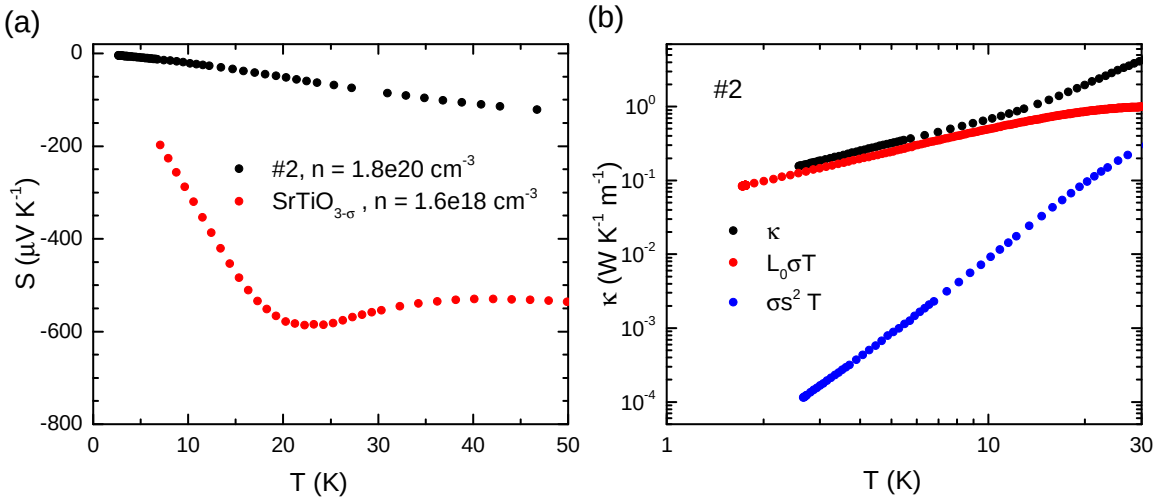

Fig. 4.3 ***Seebeck effect and the component of thermal conductivity:*** *(a) Seebeck coefficient (S), (b) the modification term $\sigma S^2 T$ with the expected electronic thermal conductivity $L_0\sigma T$ and total thermal conductivity κ as a function of temperature in log-log scale. The $L_0\sigma T$ becomes closer to κ as temperature decreases.*

fig4.3

As discussed in Chapter 1, the existence of the thermoelectric effect modifies Ohm's and Fourier's law to the transport equations related by Onsager's relations. It is also the case in the presence of two types of entropy carriers such as electron and phonon in our case as already discussed in $SrTiO_{3-\delta}$ in Chapter 2. The modification term in thermal conductivity $\overline{\overline{\Xi}} = \overline{\alpha}\,\overline{\rho}\,\overline{\alpha}\,T$ as shown in Eq 3.4 can be rewritten as

$$\overline{\overline{\Xi}} = \overline{\sigma}\,\overline{s}^2\,T \tag{4.4}$$

eq4.4

For extracting the electronic thermal conductivity, we should quantify the modification term $\overline{\overline{\Xi}}$.

Without a magnetic field, $\overline{\overline{\Xi}}$ can be expressed as scalar form. Fig 4.3 (a) shows the Seebeck effect of sample #2 compared with the $SrTiO_{3-\delta}$ sample with a carrier density two orders of magnitude lower $n = 1.6\times10^{18} cm^{-3}$. While the Seebeck coefficient is much smaller and a phonon drag peak found in $SrTiO_{3-\delta}$ is absent in sample #2. Fig 4.3 (b) compares the modification term $\sigma S^2 T$ with the expected electronic thermal conductivity $L_0\sigma T$ and total thermal conductivity κ, the $L_0\sigma T$ becomes closer to κ as temperature decreases. Moreover, $\sigma S^2 T$ is more than 10 folds smaller than κ and $L_0\sigma T$ in the temperature range we are

interested in. It is also the case for sample #1. According to these results, the possible influence on κ by the thermoelectric effect can be ignored in the two samples. We can also extend it to the situation with magnetic fields. Then we can directly use Fourier's law during our measurements. Nevertheless, the total thermal conductivity κ is still a mixture of electron and phonon contribution.

4.2.2 Difference of thermal conductivity in magnetic field

As discussed before, the total thermal conductivity in the two $SrTi_{1-x}Nb_xO_3$ samples is approximately equal to the sum of phononic and electronic parts. Previous reports on bismuth and antimony [154; 159–161], succeed in separating the phononic and the electronic contribution to the total thermal conductivity by exploiting the effect of the magnetic field on the electron contribution. We will use this method in our two samples to separate the electron and phonon contribution.

The sketch of the measurement setup has been introduced in Chapter 1. In the presence of a magnetic field along the z-axis and heat flux along the x-axis, a longitudinal (∇T_x) and transverse (∇T_y) thermal gradient turns up. The longitudinal thermal conductivity is equal to $k_{xx} = -\frac{J^Q \nabla T_x}{\nabla T_x^2 + \nabla T_y^2}$ and the transverse thermal conductivity is equal to $k_{xy} = \frac{J^Q \nabla T_y}{\nabla T_x^2 + \nabla T_y^2}$ (see chapter 1 Eq 1.64 and 1.65). Note that in our cases, ∇T_y at 12 T is in the same order as ∇T_x in low temperature. So to get access to k_{xx} and k_{xy}, we need to measure both the ∇T_x and ∇T_y.

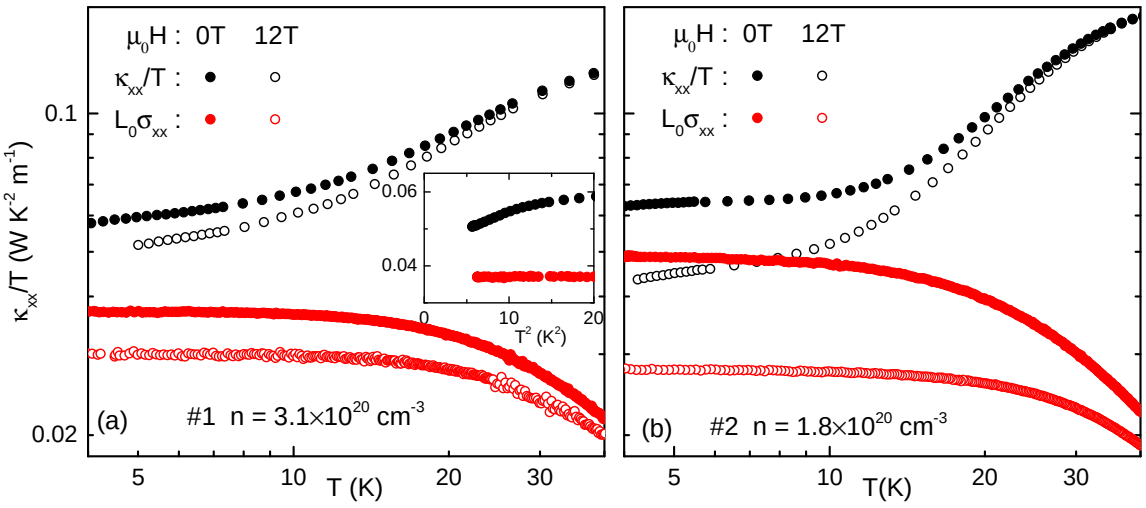

Fig. 4.4 ***Thermal conductivity in Nb-doped $SrTiO_3$:*** *Thermal conductivity divided by temperature (κ_{xx}/T) at B= 0 and B= 12 T compared with the electrical conductivity multiplied by the Sommerfeld value ($L_0\sigma_{xx}$) in sample #1 (a) and in sample #2 (b). κ_{xx}/T increases with warming, because of the phonon contribution, which rises faster than T. $L_0\sigma_{xx}$, which is a rough estimate of the electronic contribution to κ_{xx}/T decreases with warming due to the reduction of electrical conductivity by inelastic scattering. Note the reduction induced by the magnetic field in both. The inset is a zoom on the low-temperature data, showing that they tend to join in the zero-temperature limit.*

fig4.4

Fig 4.4 shows the temperature dependence of longitudinal thermal conductivity divided by temperature (κ_{xx}/T) with and without a magnetic field in two samples of $SrTi_{1-x}Nb_xO_3$. One can clearly see a difference of κ_{xx}/T between 0 T and 12 T. Studies of the thermal conductivity in the insulating parent compound $SrTiO_3$ show that a magnetic field of 12 T reduces κ_{xx} at most by 7×10^{-3} [162]. This is orders of magnitude smaller than the effect of the magnetic field of κ_{xx} in the sample #1 and #2 which change to about 4×10^{-2} at 30 K and increases as temperature goes down. This implies that the difference in thermal conductivity can be approximately attributed to electron contribution. Fig 4.4 also shows the expected electronic thermal conductivity divided by temperature ($L_0\sigma - xx$) at 0 and 12 T. Compare $L_0\sigma_{xx}$ and κ_{xx}/T at 0 T, they tend to join each other as temperature tends to zero (see inset) which agrees with the validity of WF law at zero limit temperature. At finite temperatures, the difference of $L_0\sigma_x x$ between 0 T and 12 T is a bit larger than the difference of κ/T showing the violation of WF law. One could also notice that the difference of κ_{xx}/T and $L_0\sigma_{xx}$ is larger in sample #1 is smaller than in sample #2 with a lower carrier concentration. It is a natural consequence of the lower carrier density of sample #1 that has larger electric conductivity because of the less impurity scattering which is also the case for electronic thermal conductivity.

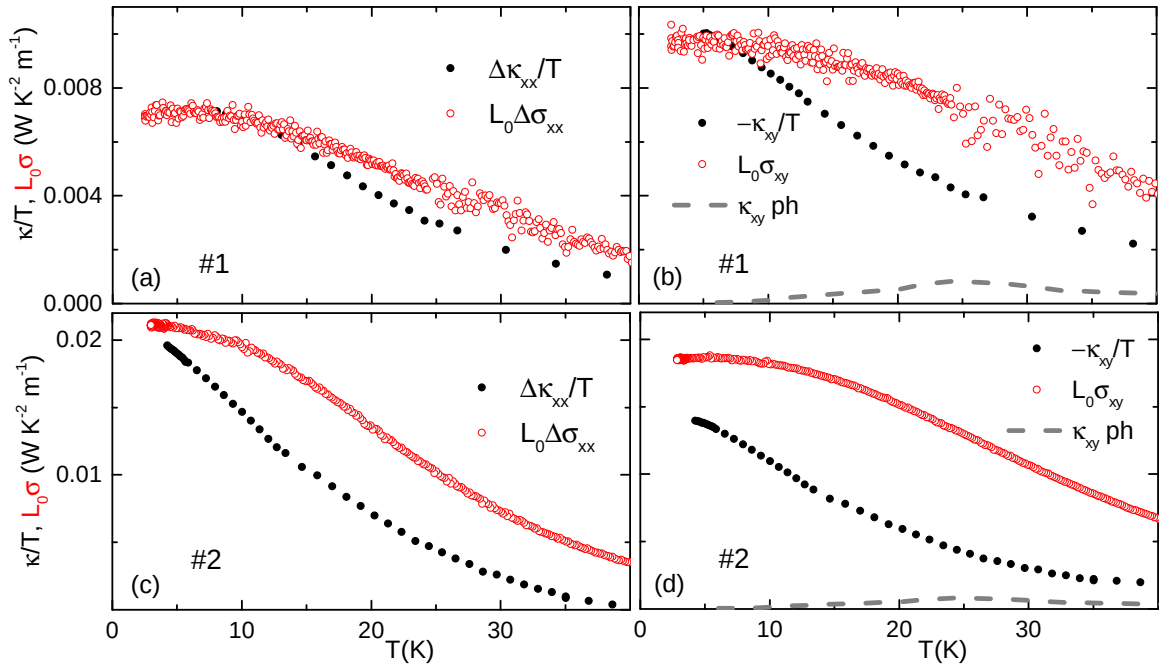

Fig. 4.5 ***Longitudinal and Hall conductivity:*** *(a) The difference in longitudinal thermal conductivity divided by temperature between zero field and 12 T. ($\Delta\kappa_{xx} = \kappa_{xx}(0T) - \kappa_{xx}(12T)$) in sample #1. Also shown is the difference in the longitudinal electric conductivity multiplied by the Sommerfeld value ($\Delta\sigma_{xx} = \sigma_{xx}(0T) - \sigma_{xx}(12T)$). (c) Same for sample #2. (b) The transverse thermal conductivity κ_{xy} divided by temperature, compared with the transverse electric conductivity σ_{xy} multiplied by L_0 (d) same for sample #2. Also shown in (b) and (d) is the κ_{xy}/T caused by phonons in undoped pure STO [108; 162].*

fig4.5

According to the previous discussion, we can safely identify the field-induced change in thermal conductivity $\Delta\kappa_{xx}$ with the thermal conductivity of electrons :

$$\Delta\kappa_{xx} = \kappa^{e}_{xx}(B=0) - \kappa^{e}_{xx}(B) \tag{4.5}$$ eq4.5

Fig 4.5 (a) and (c) compare $\Delta\kappa_{xx}/T$ with $L_0\Delta\sigma_{xx}$. In both samples, these two quantities converge at low temperatures and their difference grows with increasing temperature. This implies the validation of the WF law at zero temperature and a departure from it at finite temperature which agrees with Fig 4.4 shows. The finite-temperature departure from the WF law is more significant in the sample with lower carrier density.

By the way, let's also look at the off-diagonal components of the thermal conductivity of the two samples. Fig 4.5 (b) and (d) show the temperature dependence of the transverse thermal conductivity divided by temperature ($-\kappa_{xy}/T$). In the whole temperature range, it remains close (but smaller than $L_0\sigma_{xy}$), which is what is expected for the electronic part. The measured signal is much larger than κ^{ph}_{xy}/T measured in insulating STO. In STO samples with a carrier density two orders of magnitude lower ($n \approx 10^{18} cm^{-3}$), κ_{xy}/T is larger than $L_0\sigma_{xy}$(see chapter 3), in contrast with the samples studied here, where the carrier density is two orders of magnitude larger ($n \approx 10^{20} cm^{-3}$ and the Hall angle is much smaller than unity as shown in Fig 4.6). In this case, one does not expect to see a detectable phonon drag contribution to κ_{xy} as well as to κ_{xx}. So transverse thermal conductivity κ_{xy} can be approximately equal to the transverse thermal conductivity of electrons:

$$\kappa_{xy} \approx \kappa^{e}_{xy} \tag{4.6}$$ eq4.6

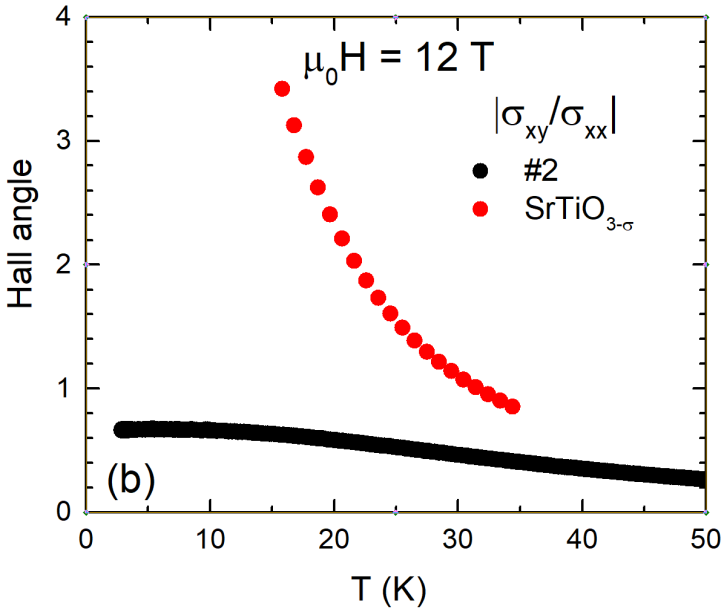

Fig. 4.6 *Hall angle as a function of temperature for sample #2 (n=1.8e10^{20}cm^{-3}) and in a lightly doped $SrTiO_{3-\sigma}$ (n=1.6e10^{18}cm^{-3}). No phonon drag peak is observed in sample #2. The Hall angle in sample #1 is much lower than in lightly doped $SrTiO_{3-\sigma}$.*

fig4.6

4.2.3 Magnetic response on the conductivity of electrons

We just show that the change in magnetic field of κ_{xx}, labeled $\Delta\kappa_{xx}$ has a purely electronic origin $\Delta\kappa_{xx} = \Delta\kappa^e_{xx}$ (see Eq. 4.5). In order to extract the temperature dependence of the longitudinal electronic thermal conductivity at zero magnetic fields ($\kappa^e_{xx}(B = 0)$) from thermal magneto-conductivity ($\Delta\kappa^e_{xx}$), we need an additional assumption: At any given temperature, the field dependence of κ^e_{xx}, is similar to the field dependence of the electrical conductivity (expressed by Eq. 4.8). Since the field-induced reduction in conductivity, in both thermal and electrical channels, is due to the same Lorentz force, this is a reasonable assumption.

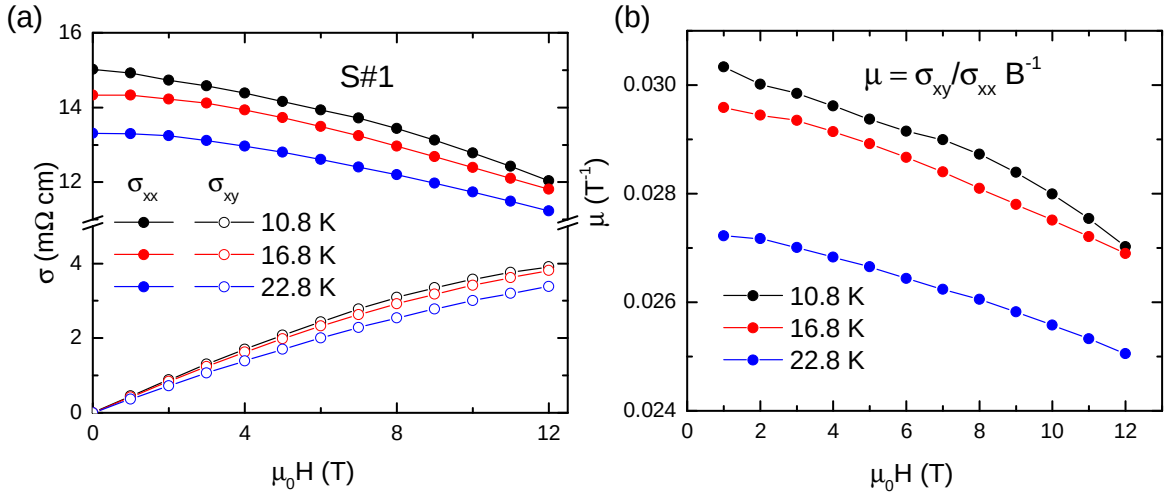

Fig. 4.7 ***Field dependence of the electric and thermal conductivity:*** *(a) Longitudinal thermal conductivity ($\Delta\kappa_{xx} = \kappa_{xx}(0) - \kappa_{xx}(B)$) divided by temperature, (b) Longitudinal electric conductivity ($\Delta\sigma_{xx} = \sigma_{xx}(0) - \sigma_{xx}(B)$) and (c) Longitudinal Lorenz ratio ($L_{xx}/L_0 = \Delta\kappa_{xx}/TL_0\Delta\sigma_{xx}$) as a function of the magnetic field for three temperatures. (d), (e) and (f) are the same as (a), (b), and (c) in transverse configuration. The Lorenz ratios L_{xx} and L_{xy} are constant in the field but smaller than L_0.*

fig4.7

Let's first look at the field-dependent electrical conductivity. The field-induced decrease in electrical conductivity σ_{xx} (i.e. the magnetoresistance) in metallic STO was the subject matter of a previous study [127], which found that both longitudinal and transverse conductivity shown in Eq 1.53 and 1.53 which follow the behavior expected in the semi-classical picture becomes:

$$\sigma_{xx} = \frac{ne\mu}{1 + \mu^2 B^2} \tag{4.7}$$ eq4.7

$$\sigma_{xy} = \frac{ne\mu}{1 + \mu^2 B^2}\mu B \tag{4.8}$$ eq4.8

Here, n is the carrier density, e is the electron charge and μ is mobility. Fig 4.7 (a) shows the field dependent σ_{xx} and σ_{xy} at 10.8, 16.8, and 22.8 K in two samples of $SrTi_{1-x}Nb_xO_3$.

σ_{xx} decreases with the field while σ_{xy} shows the opposite trend. Both σ_{xx} and σ_{xy} decrease with temperature but the decreasing of σ_{xx} is larger. These lead to the monotonically decreasing of μ with increasing magnetic field and/or temperature. The results agree with the previous study[127]. Thus, mobility $\mu(B,T)$ is the only adjustable parameter depending on temperature and magnetic field for σ_{xx} and σ_{xy}. A remarkable (and poorly understood) fact about metallic STO is that the field dependence of mobility shows little dependence on the orientation of the magnetic field [127].

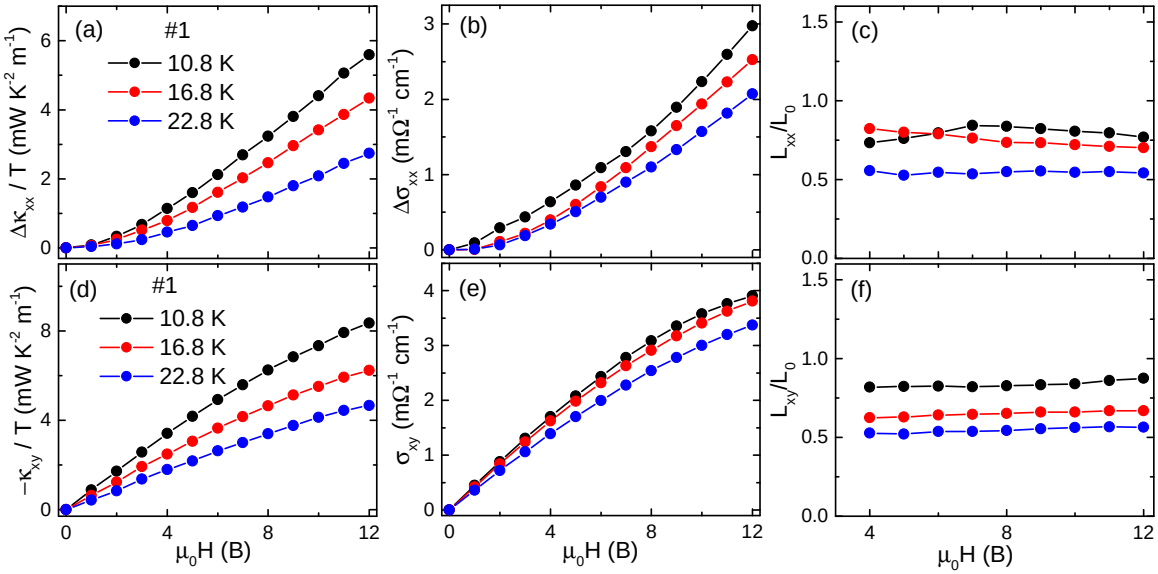

Fig. 4.8 ***Field dependence of the electric and thermal conductivity:*** *(a) Longitudinal thermal conductivity ($\Delta\kappa_{xx} = \kappa_{xx}(0) - \kappa_{xx}(B)$) divided by temperature, (b) Longitudinal electric conductivity ($\Delta\sigma_{xx} = \sigma_{xx}(0) - \sigma_{xx}(B)$) and (c) Longitudinal Lorenz ratio ($L_{xx}/L_0 = \Delta\kappa_{xx}/TL_0\Delta\sigma_{xx}$) as a function of the magnetic field for three temperatures. (d), (e) and (f) are the same as (a), (b), and (c) in transverse configuration. The Lorenz ratios L_{xx} and L_{xy} are constant in the field but smaller than L_0.*

fig4.8

Although the electric conductivity shows a unique response to the magnetic field in the two samples, the field response for electronic thermal conductivity should be the same. Because, in the semi-classical picture, electrical conductivity and electronic thermal conductivity (see Eq 1.53, 1.54, 1.55, and 1.56 in Chapter 1) show the same field dependence related to the common mobility μ. Then we turn our sight to the data. Fig 4.8 (a) (b) (c) shows the field dependent $\Delta\kappa_{xx}/T$, $\Delta\sigma_{xx}$ and L_{xx}/L_0 in sample #1 at 10.8, 16.8 and 22.8 K. Both $\Delta\kappa_{xx}/T$ and $\Delta\sigma_{xx}$ increase with the field. We note that L_{xx}/L_0 are smaller than one but independent of the field which proves our suppose. In transverse, the $-\kappa_{xy}/T$, σ_{xy} and L_{xy}/L_0 evolving with the field as shown in Fig 4.8 (d) (e) (f) are similar. While the little difference between L_{xx}/L_0 and L_{xy}/L_0 as shown in Fig 4.8 (c) and (g) can be attributed to the transverse phononic thermal conductivity which is not extracted from the κ_{xy}.

Our assumption here is consistent with our field-dependent data discussed before, which shows at a given temperature $\frac{L_{xx}}{L_0}$ is less than unity, but its amplitude does not depend on

the magnetic field. Combining with Eq. 4.5 the number L can express as

$$L = \frac{\kappa^e_{xx}(B=0)}{\sigma_{xx}(B=0)T} = \frac{\Delta\kappa_{xx}}{\Delta\sigma_{xx}T} \tag{4.9}$$ eq4.9

Here $\sigma_{xx}(B=0)$, $\Delta\kappa_{xx}$ and $\Delta\sigma_{xx}$ can be directly acquired from the experiment measurement. The combination of the three quantities allows us to evaluate the electronic thermal conductivity

$$\kappa^e_{xx}(B=0) = \frac{\Delta\kappa_{xx}}{\Delta\sigma_{xx}} \cdot \sigma_{xx}(B=0) \tag{4.10}$$ eq4.10

4.2.4 Electronic and phononic thermal conductivity

Having quantified κ^e_{xx} from Eq 4.10, we can also deduce κ^{ph}_{xx} by subtracting the electronic component from the total conductivity. **Fig 4.9** shows electronic and phononic thermal conductivity(κ^e and κ^{ph}) compared with the total thermal conductivity κ and the expected electronic thermal conductivity $L_0\sigma_0 T$ in sample #1 and #2 at zero field. One can see for both the two samples in panels (a) and (b) that, above 20 K, κ^{ph}_{xx} becomes an order of magnitude larger than κ_e. However, since κ^{ph}_{xx} decreases faster than κ^e_{xx} with cooling, the electron contribution becomes prominent below 10 K. κ^e is almost equal to $L_0\sigma_0 T$ at low temperatures but becomes significantly lower at higher temperatures.

The phononic thermal conductivity κ^{ph} for sample #1 and #2, shown in Fig 4.9 (c), is significantly lower than κ^{ph}_{xx} in undoped STO [40]. As one can see in the figure, κ^{ph} of our metallic samples, with about 1% (2%) of Ti atoms replaced by Nb for sample #2(#1), is similar to the total κ of insulating samples of $Sr_{1-x}Ca_xTiO_3$, with 0.91% of Sr atoms are replaced by Ca. In both cases, κ^{ph} is reduced in comparison to pristine STO, because the substituting atoms are randomly distributed and their average distance is comparable with the order of magnitude of the wavelength of thermally excited phonons. The rough similarity between Nb doping (which brings mobile electrons) and Ca substitution (which does not), indicates that scattering by mobile electrons plays a minor role.

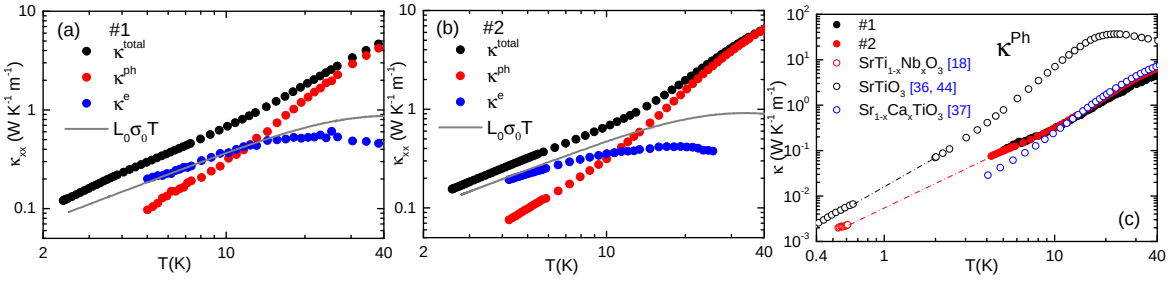

Fig. 4.9 ***Electron and phonon contributions to the thermal conductivity*** *(a) The total thermal conductivity (κ^{total}_{xx}) and its electronic (κ^e_{xx}) and phononic (κ^{ph}_{xx}) components as a function of temperature in sample #1. Also shown is the electrical conductivity multiplied by L_0. (b) same for sample #2. (c) Comparison of the phonon thermal conductivity in the two samples with total thermal conductivity of undoped STO [40; 163] with κ^{ph}_{xx} in $SrTi_{1-x}Nb_xO_3$ $n = 2.6\times10^{20} cm^{-3}$ just above the superconducting transition [78] and with $Sr_{0.991}Ca_{0.009}TiO_3$ [108].*

fig4.9

4.3 T-square resistivity prefactor in Nb-STO

Let us now turn our attention to the electronic thermal resistivity, WT, obtained by inverting κ^e_{xx}/T. Fig 4.10 shows ρ and L_0WT as a function of T^2 for the two samples. One can see that in both samples, Eq 4.1 and 4.3 hold. ρ_0 and L_0WT are identical at low temperatures confirming the validity of the WF Law in the zero-temperature limit. In both samples, the slope of $L_0WT(T^2)$ (B in Eq 4.3 times L_0) is larger than the slope of $\rho(T^2)$ (A in Eq 4.1). This behavior is similar to what has been observed in semimetals (like W, WP_2, and Sb) and heavy-fermions (like UPt_3, and $CeRhIn_5$, see Tab.4.1) and corresponds to what is theoretically expected in the e-e scattering picture [150].

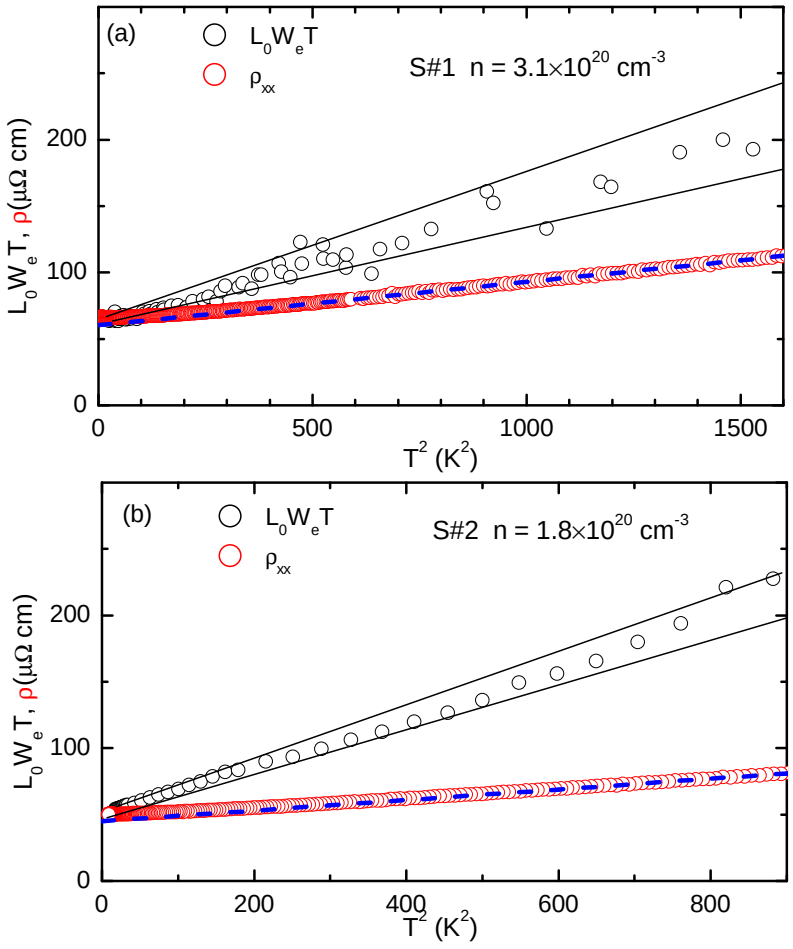

Fig. 4.10 ***Electronic thermal resistivity:*** *(a) Electric and thermal resistivity as a function of the square of the temperature for sample #1 (b) Same as in (a) for sample#2. In both cases, ρ and WT have the same intercept but different slopes. The two black solid lines show the lower and the upper limit to the slope of thermal resistivity in the two samples.*

fig4.10

The fermiology of doped strontium titanate has been the subject of several recent studies [76–78; 80; 164]. Experiments have confirmed that, as expected by band calculations [76],

three bands associated with Ti orbitals are successively filled, as the doping increases. In the two samples studied here, the carrier density is such that the Fermi surface consists of three concentric pockets all three centered at the Γ point. The average radius of the outer pocket is bounded by the carrier density: $k_F^{max} < (3\pi^2 n)^{1/3}$. This yields 2.1 (1.7) nm^{-1} in sample #1 (#2). The width of the Brillouin zone is $G = \frac{2\pi}{a} = 16.1 nm^{-1}$, where $a = 0.3905$ nm is the lattice parameter. Since $k_F^{max} < \frac{G}{4}$, Umklapp events cannot occur. This distinguishes metallic strontium titanate from other metals displaying T-square ρ and WT with amplitudes linked to each other by the WF law.

Material	ρ_0 $(n\Omega \cdot cm)$	A $(n\Omega \cdot cm \cdot K^{-2})$	B $(n\Omega \cdot cm \cdot K^{-2})$	B/A	reference
W	0.0566	8.7×10^{-4}	5.3×10^{-3}	6.1	[153]
Sb	30	0.3	0.63	2.1	[154]
WP_2	4.7	1.66×10^{-2}	7.56×10^{-2}	4.55	[156]
$CeRhIn_5$	37	21	57	2.7	[155]
$CeCoIn_5$ (B=7 T)	370	2600	5500	2.1	[165]
$CeCoIn_5$ (B=10 T)	530	900	1900	2.1	[165]
UPt_3 (a-axis)	230	590	905	1.5	[157]
UPt_3 (c-axis)	610	1600	2445	1.5	[157]
Nb:STO (S#1)	6×10^4	33	90 ± 20	2.7 ± 0.6	This work
Nb:STO (S#2)	4.5×10^4	40	185 ± 20	4.6 ± 0.5	This work

Table 4.1: ***T*-square resistivity in metals-** Residual resistivity ρ_0, and electrical (A) and thermal (B) T-square prefactors and their ratio in several Fermi liquids. In the case of $CeCoIn_5$ [165], the Fermi liquid behavior appears only in the presence of a magnetic field larger than the upper critical field of the superconductor. $\frac{B}{A}$ is always found to be larger than unity, varying between 1.5 and 6.

table4.1

4.4 Comparison with ^{3}He

The other Fermi liquid with a T-square thermal resistivity in the absence of Umklapp is normal liquid ^{3}He [166; 167]. The dominant contribution to thermal conductivity (in the zero-temperature limit) is proportional to the inverse of temperature. This κT term is strictly equivalent to the inverse of B, the slope of WT as a function T^2, and, as first calculated by Abrikosov and Khatalnikov [168], is proportional to the fermion-fermion scattering time, which quadratically decreases with temperature. Extracted from thermal conductivity, this scattering time was dubbed τ_κ, and $\tau_\kappa T^2$ was extensively measured by Greywall [169]. Theoretically, this quantity was computed by quantifying the Landau parameters of the Fermi liquid [170–172]. The agreement between the theoretically computed and the experimentally measured κT and $\tau_\kappa T^2$ is within experimental uncertainty at saturating vapor pressure and less than a factor of 2 near the melting pressure.

Let us now see how metallic strontium titanate fits in this picture. τ_κ is given by [169]:

$$\kappa = \frac{1}{3}\frac{C_V}{V_m} v_F^2 \tau_\kappa \tag{4.11}$$

eq4.11

Here, C_V is the molar-specific heat, V_m is the molar volume, and v_F is the Fermi velocity. This means that in analogy with the case of normal liquid ^{3}He [169], B, the prefactor of T-square thermal resistivity, is inversely proportional to $\tau_\kappa T^2$:

$$\frac{1}{\tau_\kappa T^2} = \frac{v_F^2}{3}\frac{\gamma}{V_m}B \tag{4.12}$$ eq4.12

Using the reported values of γ (ranging from 1.55 to 1.9 mJ/mol.K^2 [173–175] at this doping level) and extracting the average Fermi wave-vector from carrier density, one can quantify the Fermi velocity and find $\tau_\kappa T^2$. The results are listed in Tab. 4.2. Unsurprisingly, $\tau_\kappa T^2$ is orders of magnitude larger in STO than in ^{3}He, which has a lower Fermi temperature and higher fermion-fermion collision cross-section.

A more instructive basis for comparison is a dimensionless collision cross-section defined as [172; 176–178]:

$$\zeta = \frac{\hbar E_F}{\tau_\kappa T^2 k_B^2} \tag{4.13}$$ eq4.13

The amplitude of this quantity in a Fermi liquid is set by a combination of its Landau parameters [176; 179; 180]. As seen in table 4.2, ζ in ^{3}He, strongly correlated and close to both localization and a magnetic instability [181], varies from 35 to 60. In contrast, ζ in STO, at this doping level (where the effective mass is close to four times the bare electron mass [5; 173]), is ≈ 3.

System	κ T (W.m)	v_F (m/s)	k_F (nm^{-1})	E_F(K)	$\tau_\kappa T^2$ (ns.K^2)	ζ
^{3}He (saturating vapor pressure)	2.9×10^{-4}	60	7.9	1.8	3.9×10^{-4}	35
^{3}He (melting pressure)	7.3×10^{-5}	32.4	8.9	1.1	1.4×10^{-4}	58
$SrTi_{3-x}Nb_xO_3$ (n=$3.1\times10^{20} cm^{-3}$)	27 ± 6	6×10^4	2.1	480	1.4	2.6 ± 0.6
$SrTi_{3-x}Nb_xO_3$ (n=$1.8\times10^{20} cm^{-3}$)	13 ± 1.5	5×10^4	1.7	330	0.8	3.2 ± 0.3

Table 4.2: **Thermal and electronic properties of ^{3}He and $SrTi_{3-x}Nb_xO_3$:** Thermal conductivity, fermion-fermion scattering and Fermi liquid properties in a strongly correlated and a weakly correlated fermionic system. table4.2

Thus, not only the existence of the T-square thermal resistivity in metallic strontium titanate but also its amplitude can be accounted for by considering it as a Fermi liquid with moderate correlations. As for T-square electrical resistivity what we studied here at low temperatures (that is below the degeneracy temperature of electrons and the minimum energy of the soft TO phonons), could be accounted for, assuming a rough recovery of the Wiedemann-Franz law in the presence of disorder. However, the theory for such a scenario is yet to be elaborated. It may require including the gradient of momentum flow caused by the disorder and phonon scattering.

4.5 Conclusion

In this work, first we found a self-consistent experimental way to extract the electronic thermal conductivity in Nb-doped $SrTiO_3$. By detecting the magnetic field response of thermal conductivity, We hypothesize that the ignored electron-phonon interaction and phonon

contribution and the same field response in electrical and thermal conductivity (these hypotheses also be verified by experimental results), eventually extract the electronic thermal conductivity. Second, our results show a robust T-square thermal resistivity and its amplitude correlates with the T-square electrical resistivity. However, unlike other Fermi liquids with Umklap scattering, there is no difference in the T-square thermal resistivity in metallic strontium titanate and the others. Besides this, it also shows similarity with ^{3}He which is also absent of Umklap scattering. Third, according to these results, we can conclude that the electron transport behavior in dilute metal STO at least its T-square electrical and thermal conductivity at low temperatures can be considered a Fermi liquid. Nevertheless, the mechanism of the momentum and energy dissipation between the collision of electrons in dilute metal STO is still unknown.

Chapter 5

Thermal transport in $EuTiO_3$

Summary of the Chapter

In this chapter, I present the electric, thermoelectric, and thermal transport properties of $EuTiO_3$. The temperature dependence of the resistivity, ρ, the Hall carrier concentration n_H, and the Seebeck coefficient, S, all point to an insulating band gap of around 0.22 eV. A kink found in both ρ and S around 260 K is identified as a signature of the structural transition. A hysteresis in resistivity near this temperature may point to the first-order nature of this structural transition. The thermal conductivity (κ) is much lower compared to $SrTiO_3$ and is akin to the thermal conductivity of glasses. Its field dependence points to the scattering of phonons by the magnetic excitations as the source of the glass-like behavior of κ. The results provide an interesting challenge for the theory attempting to achieve a unified picture of thermal transport in crystals and glasses.

The contents of this chapter are based on the paper published in A. Jaoui, S. Jiang et al., arXiv:2307.02058 [182].

5.1 Motivation and samples

At room temperature, $EuTiO_3$ is isostructural to $SrTiO_3$ with the same lattice parameter $a \approx 0.39nm$ because the ionic radii of Eu^{2+} and Sr^{2+} are very similar. Like $SrTiO_3$, $EuTiO_3$ also undergoes a cubic-to-tetragonal transition but at a higher temperature (typically between 235 K to 280 K depending on the defects concentration). It is also a quantum paraelectric but with a much lower dielectric constant around 430 at 4.2 K (see Fig 2.11). However, in contrast with $SrTiO_3$, it has magnetic properties as the ionic Eu^{2+} host a large spin of $7\mu_B$ that order antiferromagnetically below $T_N = 5.5$ K[21; 183]. How the Eu^{2+} spin influences the transport properties of the perovskite quantum paralectrics is the main motivation of this study.

Compared to $SrTiO_3$ which are commercially available, the growth of $EuTiO_3$ crystal is more dedicated. One of the reasons is that $EuTiO_3$ hosts divalent europium: Eu^{2+} with large magnetic momentum of $7\mu_B$ and Eu^{3+} with no magnetic moment. It thus requires starting with high-purity europium oxide. The $EuTiO_3$ (ETO) single crystals studied here were provided by two different labs: in Tsukuba (Sample T1 and T2) and in Colone (Sample C1, C2, and C3). They all used the floating-zone technique to grow the sample

as described in Ref. [184]. In order to prevent the formation of the $Eu_2Ti_2O_7$ pyrochlore phase, the growth was performed in Argon atmosphere and without any preliminary powder reaction, similar to Ref. [185]. Powders of Eu_2O_3, TiO, and TiO_2 were mixed in a ratio to reach $EuTiO_{3-\delta}$, pressed to a rod, and installed into the floating-zone furnace. In a series of growth attempts, it turned out that it was necessary to mix the above materials with a nominal oxygen deficiency of $\delta = 0.05$. This allowed to compensation possible off-stoichiometries of the starting materials or an oxygen capture during the growth process. Single crystallinity of the grown crystal was confirmed by Laue images and phase purity was verified by X-ray powder diffraction.

5.2 Results

In the following section, I will present the results on electric, thermoelectric, and heat transport in two $EuTiO_3$ samples labelled T1 and T2, receptively.

5.2.1 Resistivity and Hall effect

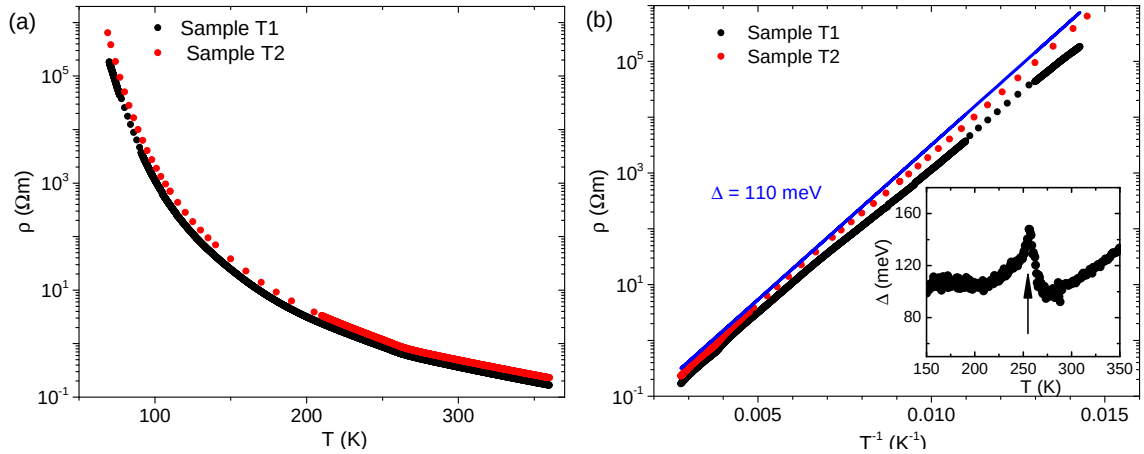

Fig. 5.1 **Electrical resistivity and activation gap of $EuTiO_3$:** *(a) Resistivity, ρ, as a function of temperature in two single crystals of $EuTiO_3$ in a semi-logarithmic plot. (b) Arrhenius plot of the same data: $ln\rho$ vs. T^{-1}. The solid blue line corresponds to $\Delta = 110$ meV. The inset shows the temperature variation of $\Delta = -k_B T^2 \frac{\partial ln\rho}{\partial T}$, with an arrow pointing to T_{AFD}, the temperature of antiferrodistortive transition.*

fig5.1

DC electrical resistivity of Sample T1 and T2 was measured from 360 K to 60 K. Fig.5.1 (a) shows the temperature dependence of electrical resistivity ρ. It increases exponentially by seven orders of magnitude upon cooling from 360 K to 60 K. Notice that below 60 K, DC electrical resistivity measurement of $EuTiO_3$ becomes unreliable because its resistance increases to tens of Giga Ω which is comparable with the impedance of the voltmeter. We also studied the Hall response. The Hall resistivity is linear with the field at several temperatures 100 K, 150 K, 200 K, 250 K, and 300 K [see in Fig.5.2 (a)]. Measurements at B = 3 T and -3 T between 60 K and 360 K allow us to extract the Hall resistivity as a function of the

temperature shown in Fig.5.2 (b). We note that $\rho_{xy} < 0$ implies the temperature-activated charge carrier is the electron. Based on this result we can deduce carrier concentration $n_H = \mu_0 H/(-\rho_{xy} e)$.

Both ρ and n_H plot in log scale as a function of the inverse of the temperature display the linear behavior characteristic of the Arrhenius law $\sigma \propto n \propto exp(-\Delta/(K_B T))$ as show on Fig.5.1 (b) and Fig.5.2 (b). The estimated activated gap is 0.1 eV (blue lines on Fig.5.1 (b)). Derivative $ln\rho$ vs T^{-1}, we can obtain the Δ as function of temperature [see inset of Fig.5.1 (b)]. A small kink is found at around 260 K which we identify as the temperature of the structural transition in $EuTiO_3$ [22; 186]. We note that n_H deviates upwards from Arrhenius law above 200 K which implies the activation gap increases with temperature. The reason for this deviation is still unknown.

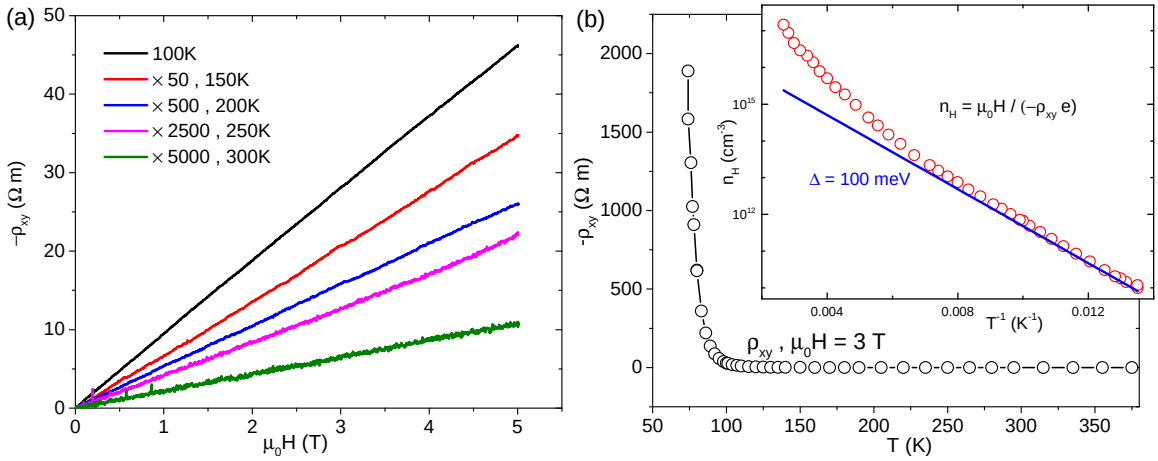

Fig. 5.2 **Hall effect and carrier concentration of $EuTiO_3$:** *(a) Hall resistivity ρ_{xy} as a function of field up to 5 T in different temperatures. The linear behavior with a negative value implies electron is the only electric carrier. (b) Temperature dependence of ρ_{xy} at 3 T. Arrhenius plot of the Hall carrier concentration: ln n_H vs. T^{-1}.*

fig5.2

5.2.2 The Seebeck coefficient

This activated behavior is also confirmed by our measurements of the Seebeck coefficient [See Fig.5.3]. The thermoelectric power has a negative sign and an amplitude in the range of mV/K, typical of a narrow gap semiconductor. The Seebeck coefficient in an intrinsic semiconductor is expected to be $\approx \frac{k_B}{e}\frac{\Delta}{k_B T}$ [24]. Thus, by plotting S as a function of T^{-1} (see the inset), one expects to see a straight line whose slope yields Δ. As seen in the inset of Fig.5.3, this is indeed what our data yields, with Δ around 0.1 eV. Note that this temperature dependence is qualitatively distinct from what is expected in extrinsic semiconductors [187] as seen, for example, in the case of Nb-doped STO [132].

Thus, the temperature dependence of resistivity, carrier concentration, and Seebeck coefficient all point to a similar energy gap between the chemical potential and the conduction band. The Hall and the Seebeck coefficients are both negative, indicating that carriers are electron-like and thermally excited to live in the conduction band originating from Ti$-d$

orbitals.

S also shows an anomaly near 260 K which agrees with ρ. Now we can undoubtedly identify the kink as the temperature of the structural transition in $EuTiO_3$ [22; 186]. Like $SrTiO_3$ [46], this transition makes $EuTiO_3$ tetragonal [188]. We cannot rule out a very small difference in the amplitude of the activation gap between the cubic and the tetragonal phases [See the inset of Fig5.1 (b)].

Assuming that the chemical potential is at halfway between the chemical potential and the valence band leads us to conclude that the band gap of $EuTiO_3$ is $\approx$ 0.22 eV. This is remarkably smaller than the 3.2 eV gap of $SrTiO_3$ [5], but only slightly smaller than what a recent DFT calculation [189] found (0.27-0.33 eV). According to another and earlier theoretical study [190], the magnitude of the band gap in $EuTiO_3$ depends on the amplitude of the Hubbard U, and a realistic U (5-6 eV) would lead to a band gap of 0.2-0.4 eV. Thus, the narrow gap detected by our transport studies is close to what is intrinsically expected in this solid. Optical probes, however, have detected a larger gap (0.8-0.9 eV) [191; 192]. Such larger energy scales are possible indications that the Density of States (DOS) near the Eu$-f$ level is not featureless [189].

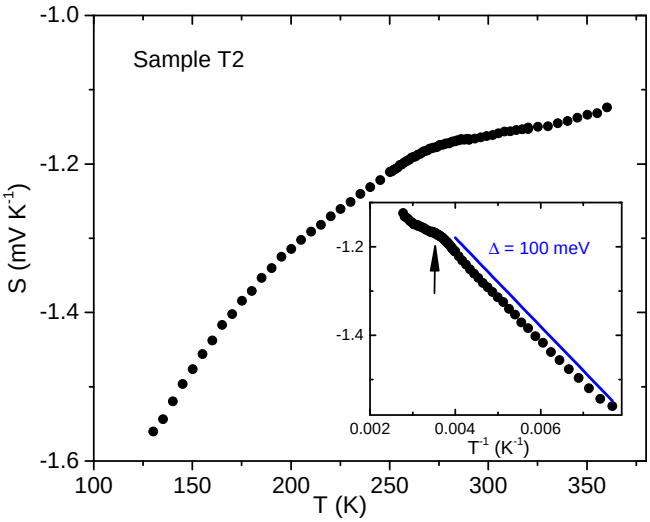

Fig. 5.3 **Temperature dependence of Seebeck coefficient S** . *The data is restricted to $T > 120K$, below which measurement becomes problematic. The inset shows S as a function of T^{-1}. The solid blue line corresponds to $\Delta = 0.1eV$. The arrow points to T_{AFD}.*

fig5.3

5.2.3 Resistivity hysteresis near the AFD transition

We also detected an unexpected and reproducible hysteresis of resistivity near this phase transition [see Fig. 5.4]. We carefully measured the resistivity during sweeping temperatures up and down between 230 K and 300 K. The hysteresis behavior turns up as $EuTiO_3$ entering the tetragonal phase around 260 K which is independent of the temperature sweeping rates and currents [see Fig. 5.4 (a)]. By plotting $d\rho/dT$ as a function of T, the hysteresis becomes clearer as shown in Fig. 5.4 (b). Taken at its face value, this indicates that this structural phase transition is first order.

The structural transition in $EuTiO_3$ is believed to be similar to the structural transition in $SrTiO_3$ an antiferrodistortive transition in which adjacent octahedra rotate in opposite orientations [22]. In the case of $SrTiO_3$, this transition is known as a rare case of second-order structural phase transition. However, in our study of resistivity, we found that the anomaly at $\approx$ 260 K presents a hysteresis, which was found to be reproducible. This may point to the first-order nature of this structural transition in $EuTiO_3$.

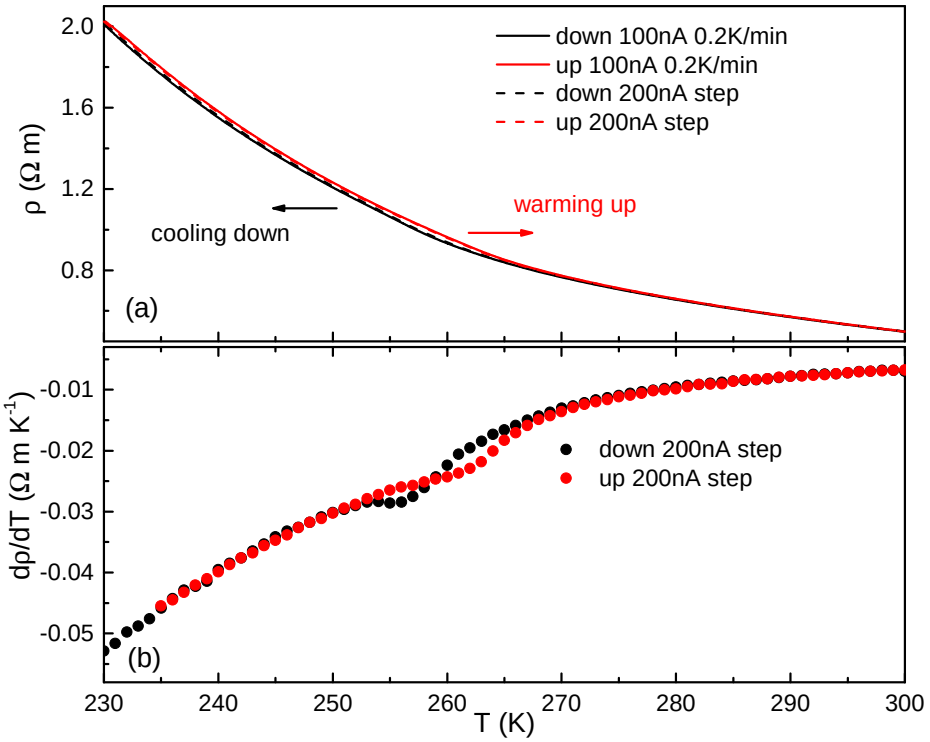

Fig. 5.4 **Hysteresis of temperature-dependent resistivity**: *(a) Temperature dependence of resistivity near the structural transition for upward and downward sweeps either with a continuous ramp or by steps. (b) The temperature derivative of resistivity for an upward and a downward sweep with discrete steps.*

fig5.4

5.2.4 Temperature dependent thermal conductivity

After discussing the intriguing electric and thermoelectric transport properties of $EuTiO_3$, then we turn our attention to thermal transport. Thermal conductivity κ was measured from 300 K to 0.3 K [see Fig. 5.5]. First κ was measured in PPMS including two temperature ranges: 300 K to 50 K by using Type E thermocouples(red open circle) and 60 K to 6 K by using Cernox 1030 (black open circle). Below 6 K, κ was measured in dilution by using Cernox 1030 (blue open circle). The measurement setups are shown in Chapter 1 and Appendix B. They all agree well after correcting the geometric factor of about 10%.

Fig. 5.5 shows the temperature dependence of thermal conductivity, κ, of $EuTiO_3$ sample T1 compared to $SrTiO_3$ in log scale. Unlike in $SrTiO_3$ where κ displays a peak at 20K, κ of $EuTiO_3$ shows two minimum. One is around 260 K (inset) which is associated with the

AFD transition, the other is around 5 K where the antiferromagnetic order appears.

As we discussed in Chapter 1, in insulating crystals, the flow of heat can be understood by considering the response of a gas of phonons to a temperature gradient. This picture, first drawn by Peierls [35], using a linearized Boltzmann equation, is remarkably successful in describing the thermal conductivity, κ, of most insulators [193; 194]. It explains why at an intermediate temperature, κ peaks [195], separating a high-temperature decrease by warming (due to anharmonicity), and a low-temperature decrease by cooling (due to phonon depopulation). It's the case for quantum paraelectric $SrTiO_3$. While in amorphous solids, on the other hand, there is no such peak in $\kappa(T)$ and heat diffuses thanks to off-diagonal coupling across harmonic branches [196–199]. While in some crystals, however, display glass-like thermal conductivity[200–206]. The thermal conductivity of these materials can be very low and/or feature a monotonic temperature dependence (lacking the T^{-1} decrease at high temperature). They are sought after since a low lattice thermal conductivity would lead to a large thermoelectric figure of merit [207]. $EuTiO_3$ is one of the cases. It shows a striking result that the large reduction of the amplitude of κ in $EuTiO_3$ between 2K to 300K and the absence of a peak around 20K in the paramagnetic state. Such behavior of κ is akin to what is seen in amorphous silica. We will discuss it in Section 3.

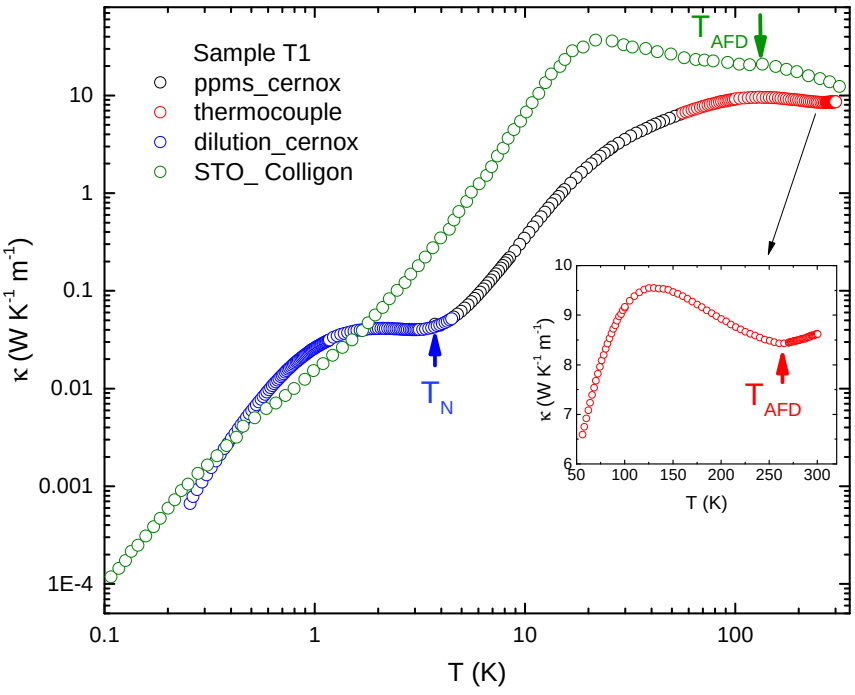

Fig. 5.5 **Thermal conductivity κ of $EuTiO_3$ and $SrTiO_3$** *FOr $EuTiO_3$, from 0.3 K to 6 K κ were measured by using Cernox1030 as the thermometer in dilution(blue circle). From 6 K to 60 K is in PPMS(black circle). From 60 K to 300 K were using type E thermal couple in PPMS(red circle). Insert is zooming from 50 K to 300 K. The blue arrow corresponds to the Antiferromagnetic transition. The red and green arrows correspond to the Antiferrodistortive transition.*

fig5.5

5.2.5 Field dependent thermal conductivity

To identify the origin of the reduced thermal conductivity in ETO we studied the field dependence of κ_{xx}. Fig. 5.6 shows κ_{xx} as a function of temperature in different magnetic fields of Sample T1. As the magnetic field increases, κ_{xx} vs T first shows a small dip with a peak around 1 K and then gradually becomes monotonic. Fig. 5.6 (b) displays the normalized κ_{xx} as a function of the magnetic field in different temperatures. It shows a sharp peak around 2 T at 0.35 K which gradually becomes two small border peaks at 2 K. As the temperature increases, the field-dependence becomes monotonic. Both results show that κ_{xx} in ETO is extremely sensitive to the magnetic field in contrast to the case of STO. This result implies that it is the scattering of the phonon on the Eu2+ ions that gives rise to the reduced thermal conductivity in ETO. Our result shows also the presence of several field scales that may be a consequence of the various energy levels of the magnetic ions and their coupling to phonon modes.

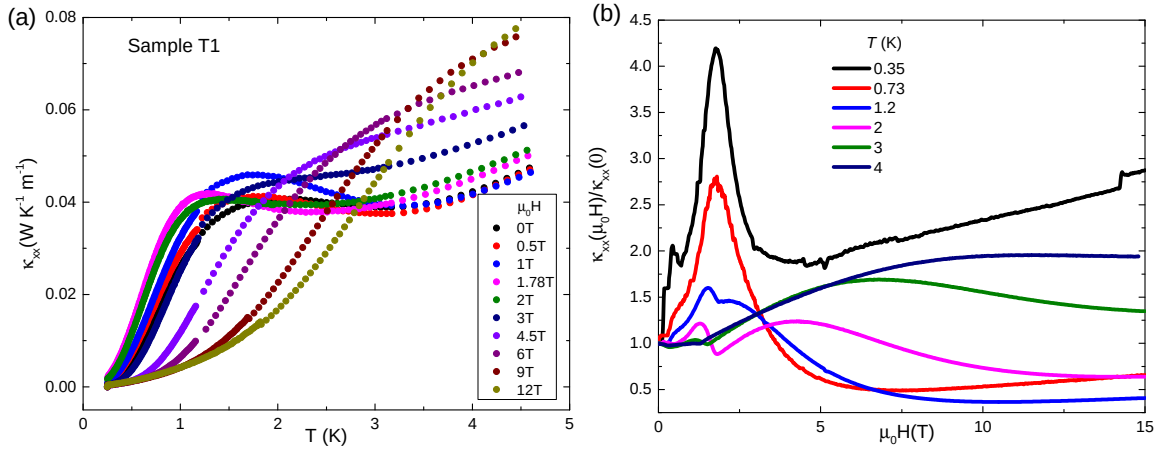

Fig. 5.6 **Longitudinal thermal conductivity κ_{xx} in magnetic field**: *(a) κ_{xx} as a function of temperature in different magnetic fields. (b) κ_{xx} as a function of the magnetic field in different temperatures.*

fig5.6

5.3 Discussion

$EuTiO_3$ displays a very different thermal conductivity compared to $SrTiO_3$. In this section, by remembering the magnetization results measured in Cologne, we excluded the extrinsic reason: $Eu^{2+/3+}$ off-stoichiometry. The glass-like thermal conductivity of $EuTiO_3$ is similar to Silica or frustrated magnet $Tb_2Ti_2O_7$. Comparison with non-magnetic perovskite solids, $SrTiO_3$, $KTaO_3$, and $EuCoO_3$, shows that what impedes heat transport are $4f$ spins at Eu^{2+} sites, which couple to phonons well above the ordering temperature. Thus, in this case, superexchange and valence fluctuations, not magnetic frustration, are the drivers of glass-like thermal conductivity.

5.3.1 Magnetization

Fig. 5.7(a) displays magnetization data M(T) of a $EuTiO_3$ single crystal for different magnetic fields between 10 and 500 mT applied along a $[100]_c$ direction of the cubic room temperature phase. At the lowest fields, the antiferromagnetic ordering causes a maximum in $M(T)$. This peak becomes a kink at an intermediate field of 500 mT. The corresponding inverse susceptibility follows a straight line over the entire temperature range from 300 K down to about 7 K (See panels (b) and (c)). The Curie-Weiss fit yields an effective magnet moment of $\mu_{eff} = 7.8\,\mu_B$/f.u. and a positive Weiss temperature of $\theta_W = 3.55\,K$, which signals a net ferromagnetic coupling. These values agree with the literature. The positive θ_W has been explained by the fact that in $EuTiO_3$ the antiferromagnetic coupling of the Eu^{2+} spins to 6 nearest neighbors (NN) is overcompensated by a larger ferromagnetic coupling to 12 next nearest neighbors[183; 192; 208–210].

Note that there is no magnetic frustration resulting from the ferromagnetic and antiferromagnetic couplings because both couplings support the G-type antiferromagnetic order. Nevertheless, a comparatively weak magnetic field of about 1.2 T is sufficient to induce a polarized magnetic state. This is because only the weaker NN antiferromagnetic coupling needs to be overcome. As shown in Fig. 5.7(d), the saturation magnetization $M_{sat} \simeq 6.73\,\mu_B$/f.u. reaches about 96 % of the expected spin-only value of $M_{sat} \simeq g\mu_B S_z = 7\mu_B$ for Eu^{2+} with half-filled $4f$ shell. An analogous 4 % reduction is obtained from the Curie-Weiss fit in the paramagnetic phase for the Curie constant, which results in a 2 % reduction of the effective magnetic moment $\mu_{eff} = 7.8\,\mu_B$/f.u. in comparison to the expected $\mu_{eff} = g\sqrt{S(S+1)}\mu_B = 7.94\,\mu_B$ for $S = 7/2$.

As is shown in Fig 5.7(e) this weakly reduced saturation magnetization has been observed in various pristine insulating samples that were obtained from different growth attempts. In contrast, however, other $EuTiO_3$ samples that were cut from the same mother crystals, but were made conducting via vacuum annealing at high temperature, see e.g. [184], reached the expected saturation magnetization of $7\mu_B/Eu^{2+}$. As it is known that the vacuum annealing of STO and ETO causes electron doping which is traced back to a reduction of the oxygen content, the different saturation magnetizations of pristine versus doped ETO can be interpreted as follows: apparently, the pristine ETO samples have a weak oxygen surplus that results in a corresponding partial oxidization of Eu^{2+} to Eu^{3+} which has a vanishing magnetic moment thereby reducing the overall magnetization. Vice versa, with decreasing oxygen content, the magnetization of pristine ETO should first increase but remain insulating until all Eu^{3+} ions are reduced to Eu^{2+} and only with further oxygen reduction a metal-insulator transition sets in via electron doping into the 3d band of Ti [184].

5.3.2 Sample dependence of thermal conductivity

As discussed above, the magnetization data of pristine ETO crystals indicate the presence of a certain mixture of Eu^{2+} and Eu^{3+} valencies, and it is known from many intermetallic materials that Eu (or other rare-earth) valence instabilities can drastically influence the magnetic and/or transport properties [211]. Therefore, we compared several $EuTiO_3$ crystals in order to check whether there is some correlation between the surprisingly low, glass-like thermal conductivity and the reduced saturation magnetization. As can be seen from Fig. 5.8(a), the overall variation of the $\kappa(T)$ curves obtained on the different samples is covered by the data obtained on samples C1 and T1, which are discussed in the previous section.

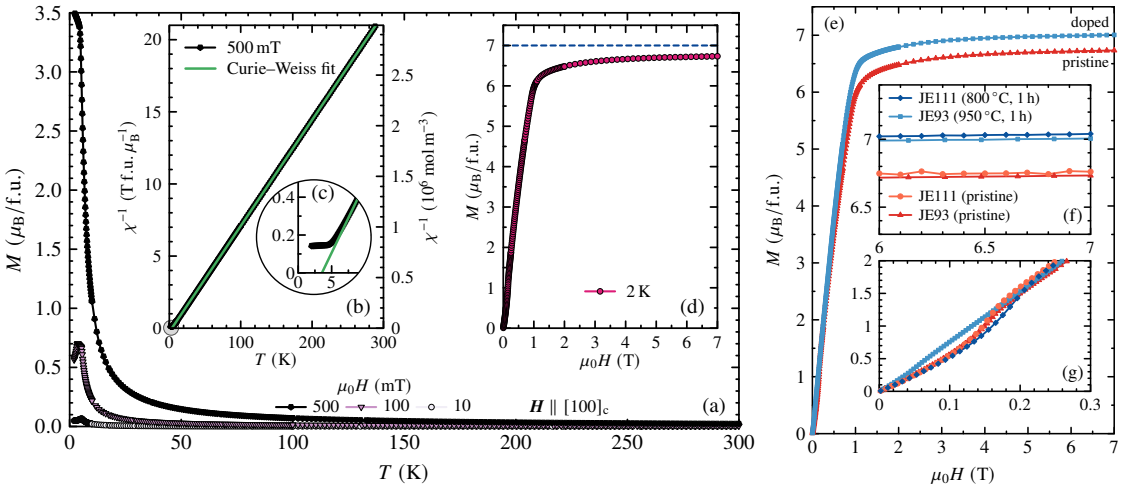

Fig. 5.7 *(a) Magnetization of $EuTiO_3$ as a function of temperature for different magnetic fields applied along the cubic $[100]_c$ direction. (b) Inverse susceptibility $\chi^{-1} = \mu_0 H/M$ at 500 mT with a Curie–Weiss fit (line) for $T > 20$ K (c) Detailed view of the low-temperature regime, revealing the Weiss temperature $\theta_W = 3.55$ K. (d) Magnetization curve measured at 2 K, which almost reaches the saturation magnetization expected for a spin 7/2 system (dashed line) (e) Magnetization curves measured on 2 different pristine $EuTiO_3$ single crystals (JE93, JE111), which both were insulating, in comparison to 2 metallic $EuTiO_3$ samples, which were weakly electron-doped by vacuum annealing [184]. Insets show enlarged views of the same data in the region of (f) the saturation magnetization and of (g) a spin-flop transition occurring at ≈ 0.2 T when the field is applied along a cubic $[100]_c$ direction (3 samples), but remains absent for $H[110]_c$ (doped sample JE93).*

fig5.7

The magnetization data of the pristine samples C2 and T1 are essentially identical to each other and agree with the data of the other pristine samples shown in Fig.5.8. While this is not surprising for C1, which is another piece from the same mother crystal JE111, this was not necessarily to be expected for T1, which was grown independently under somewhat different conditions (see above) and it is evident from the panel (a) that overall the $\kappa(T)$ curve of T1 is lying above those measured on the samples C1, C2, and C3. On the other hand, the magnetization of C3 is the only one that essentially reaches $7\mu_B$. This can be traced back to the fact this sample was vacuum annealed for 1 h at 700°C. Resistivity measurements before and after annealing did not show a measurable difference, whereas the enhanced magnetization indicates a significant variation of Eu valence towards almost pure Eu^{2+}. Nevertheless, the thermal conductivity of this particular C3 sample remains as low and glassy as those of all the ETO samples. Thus, we conclude that the weak $Eu^{2+/3+}$ off-stoichiometry is not the main mechanism that induces the unusual glass-like phonon heat transport in the ETO crystals.

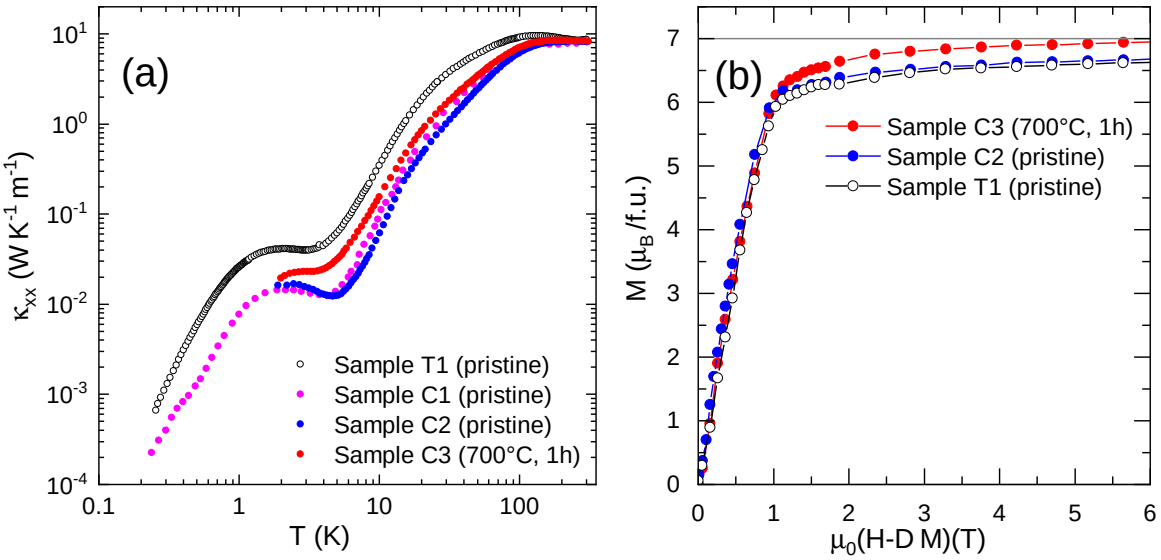

Fig. 5.8 **Sample difference of thermal conductivity κ and magnetization M** *(a) Comparison of $\kappa(T)$ of $EuTiO_3$, which were measured on different samples, which stem from different sources (T1 versus C1, C2, C3) (b) M measured on the same samples apart from C1, that got broken in the meanwhile. Note that the field axis was corrected for demagnetization effects to account for the rather different sample geometries.*

fig5.8

5.3.3 Glass-like thermal conductivity

In order to put our observation in a proper context, we compare our data with what has been reported in the case of SiO_2, which shows a spectacular difference in the thermal conductivity in its crystalline and amorphous structures [212]. As seen in Fig. 5.9, κ in amorphous silica monotonically decreases with cooling, in contrast to crystalline quartz, which has a prominent peak. At any given temperature, the crystal conducts heat at least an order of magnitude more than the glass [195]. Not only the thermal conductivity of $EuTiO_3$ is similar to silica in temperature dependence, but also in the cryogenic temperature range around the Néel temperature ($T_N \simeq 5.5$K), the $EuTiO_3$ crystalline samples conduct heat less than amorphous silica.

The order of magnitude of thermal conductivity and its temperature dependence in $EuTiO_3$ is comparable with other crystalline solids displaying a glass-like thermal conductivity, such as $Tb_2Ti_2O_7$ [202], $Tb_3Ga_5O_{12}$ [214], $Na_4Ir_3O_8$ [215], $Pr_2Ir_2O_7$ [120] and $La_{0.2}Nb_{0.4}Pb_{0.4}MnO_4$ [200]. In order to allow a direct comparison, Fig.5.9 includes the data for $Tb_2Ti_2O_7$ [202], the compound with the lowest thermal conductivity among these frustrated magnets. Note that in contrast to other members of this club of materials, $EuTO_3$ is a G-type antiferromagnet and is not frustrated.

As a further comparison, we also include κ of $EuCoO_3$ [213], which displays a temperature dependence typical of a crystalline insulator. $EuCoO_3$ is a perovskite like ETO, but it has an orthorhombic symmetry, and the valence is Eu^{3+} with only 6 electrons in the 4f shell. According to Hund's rules, this causes a vanishing magnetic moment ($J = L - S = 0$),

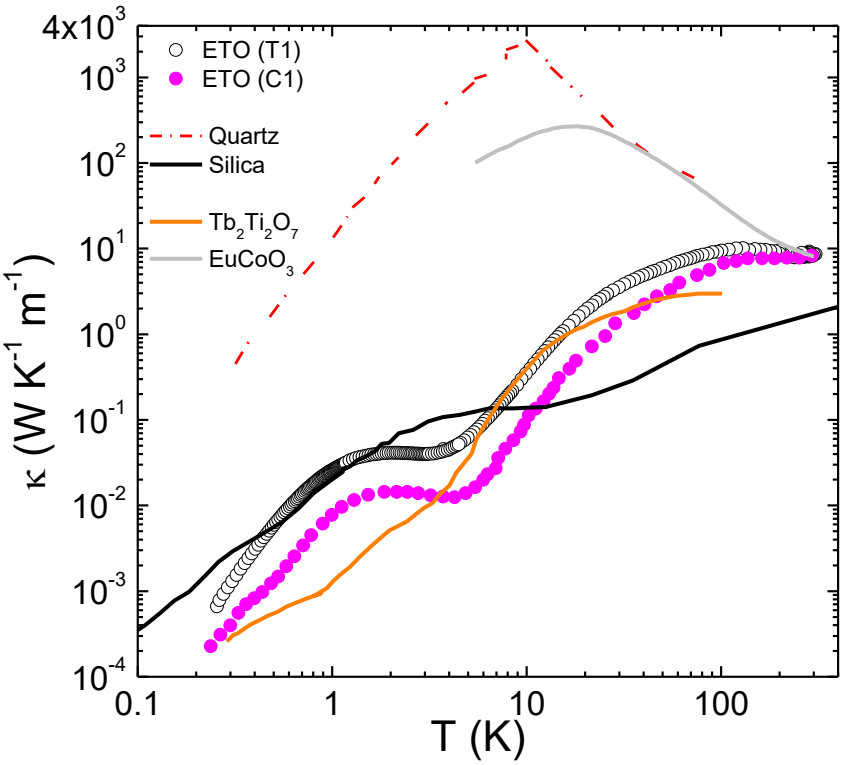

Fig. 5.9 **Comparison with crystals, glasses and glass-like crystals:** *Thermal conductivity as a function of temperature in crystalline quartz, in vitreous silica [212], in $EuTiO_3$ and in the frustrated magnet $Tb_2Ti_2O_7$ [202]. The latter two crystalline compounds conduct heat like a glass rather than like a crystal. Also shown is the crystal-like thermal conductivity of non-magnetic $EuCoO_3$ [213].*

fig5.9

in agreement with the experimentally observed van Vleck susceptibility [216], drastically different from the large local moments of $7\,\mu_B/Eu^{2+}$ in ETO.

Fig.5.10 compares the thermal conductivity of $EuTO_3$ and two other ABO_3 perovskites. $SrTiO_3$ and $KTaO_3$ are also quantum paraelectric, but not magnetic solids. Our new data on these two materials is in good agreement with previous studies of heat transport in $SrTiO_3$ [40; 92; 217] and in $KTaO_3$ [92; 217; 218]. In both cases, there is also a visible sample dependence, which is more pronounced near the peak. However, this sample dependence is much smaller than the difference between the three compounds. At room temperature, this difference is small, yet visible: $\kappa(300K)$ is ≈ 9 W/(K.m) in $EuTO_3$, ≈ 11 W/(K.m) in $SrTiO_3$ and ≈ 17 W/(K.m) in $KTaO_3$. Much more drastic is the difference in the temperature dependence between the three sister compounds. The enhancement with cooling observed in the other perovskites is absent in $EuTO_3$. This difference extends over the full temperature range above the magnetic ordering.

5.3.4 Specific heat

As reported previously [210], the specific heat in $EuTiO_3$ displays a strong dependence on the magnetic field. To separate the magnetic C_{mag} and the phononic C_{phon} contribution, we

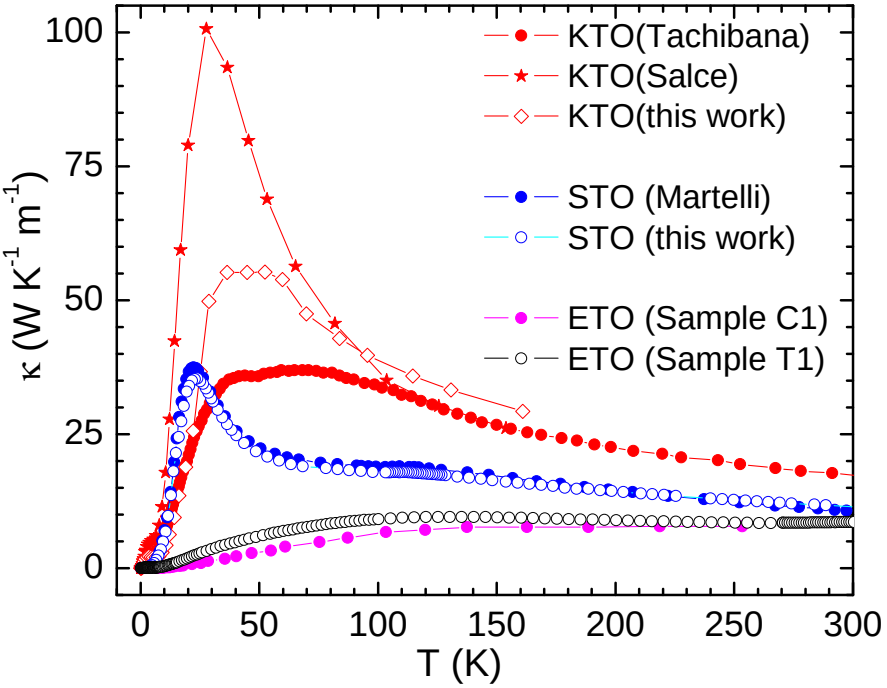

Fig. 5.10 **Thermal conductivity of three quantum para-electric solids:** *Thermal conductivity of the two $EuTiO_3$ samples in a linear scale compared with thermal conductivity of $SrTiO_3$ [40] and $KTaO_3$ [203; 218]. Note the drastic reduction of thermal conductivity in the paramagnetic $EuTiO_3$. The visible sample dependence of the data for each material is much smaller than the difference between the three compounds.*

fig5.10

subtracted from the total specific heat of $EuTiO_3$ the measured specific heat of $SrTiO_3$ (with a temperature re-scaled by a factor of 0.83 such that the positions of the C/T^3 maxima of both materials match). Note that this scaling factor is close to the ratio of the molar masses $\sqrt{M_{\rm STO}/M_{\rm ETO}} = 0.86$, the expected ratio of their Debye temperatures. Fig. 5.11 (b) shows the magnetic heat capacity C_{mag}/T of $EuTiO_3$ for different magnetic fields from 0 up to 10 T applied along a $[100]_c$ direction of the cubic room temperature phase. The sharp zero-field anomaly signals the antiferromagnetic order at $T_N = 5.5$ K that gets strongly broadened already in a field of 1 T. This reflects the magnetic-field-induced switching to the polarized magnetic state, which sets in around 1.2 T in $EuTiO_3$ [208] and, consequently, the C_{mag}/T data in larger fields no longer signal a spontaneous magnetic ordering transition, but a continuous evolution of magnetic entropy as it is the case for ferromagnets in an external magnetic field. In fact, the C_{mag}/T data of $EuTiO_3$ strongly resembles the corresponding data obtained on the Eu^{2+}-based ferromagnet EuC_2, which orders at $T_C = 14$ K [219]. The magnetic entropy obtained by integrating C_{mag}/T is displayed in the inset of Fig. 5.11 (b) and reveals that the full magnetic entropy $N_A k_B \ln(2S+1)$ of a spin 7/2 system is reached above about 15 K for zero field and also for 1 T, whereas for fields above 2 T the entropy evolution drastically broadens and extends to much higher temperatures.

As discussed in Section 2, the field dependence of κ, shown in Fig. 5.6, further points to

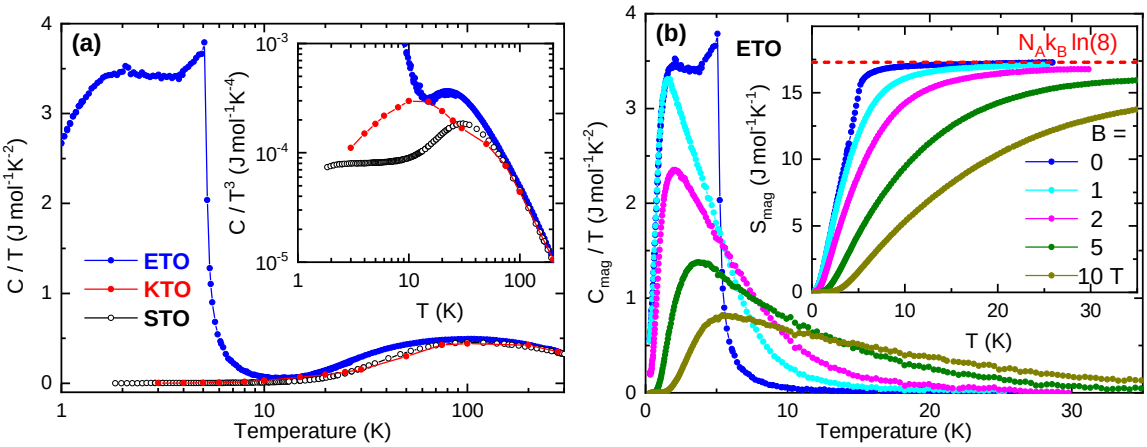

Fig. 5.11 **Specific heat in three quantum paraelectric solids:** *a) Temperature dependence of the total specific heat in $KTaO_3$, $SrTiO_3$ and $EuTiO_3$ plotted as C/T vs. T. The inset is an enlarged view of the same data shown as $\frac{C_p}{T^3}$ vs. T. Note the presence of Einstein modes in all three solids and the additional magnetic specific heat in ETO emerging below 15 K. b) Evolution of C_{mag}/T of ETO for different magnetic fields up to 10 T. The inset shows the corresponding magnetic entropy $S_{mag} = \int C_{mag}/T\, dT$ of ETO and the maximum magnetic entropy $N_A k_B \ln(2S+1)$ of a spin 7/2 system is indicated by the dashed line.*

fig5.11

an intricate coupling between Eu^{2+} spins and heat-carrying phonons.

5.3.5 Thermal diffusivity and phonon mean-free-path

Replacing Sr by Eu reduces the thermal conductivity in a wide temperature range and enhances the specific heat below 15 K. Therefore, the ratio of thermal conductivity (in W/(K.m)) to specific heat per volume (in J/(K. m^3)), i.e. the thermal diffusivity, D, (in m^2/s) is drastically modified. It is plotted in Fig. 5.12. The most striking feature of $D(T)$ is its two-orders-of-magnitude drop at the Néel temperature. Within the entry to the antiferromagnetically ordered phase, at 5.5 K, it becomes exceptionally low. Its minimum, 0.03 mm^2/s, is almost two orders of magnitude lower than the thermal diffusivity of a typical glass [220]. This low thermal diffusivity, a consequence of the combination of an unusually low lattice thermal conductivity and a very large magnetic entropy may find applications in heat management in a cryogenic context.

The thermal conductivity of an insulator can be written as:

$$\kappa = \sum_{s,\mathbf{q}} C_s(\mathbf{q}) \mathbf{v_s^2}(\mathbf{q}) \tau_\mathbf{s}(\mathbf{q}) \qquad (5.1)$$

eq5.1

the index s refers to different modes and $\mathbf{q}$ is the wave-vector. C_s, v_s and τ_s are, specific heat, velocity and scattering time. There are modes contributing to the total specific heat ($C = \sum_s C_s$), but not to thermal conductivity, because of their negligible velocity. Theoretically [22], paramagnons in the paramagnetic state have no dispersion and therefore do not carry heat. They can, however, reduce the phonon thermal transport. In ETO, phonons not only dominate thermal conductivity but also, at least down to 15 K, the specific heat. Therefore,

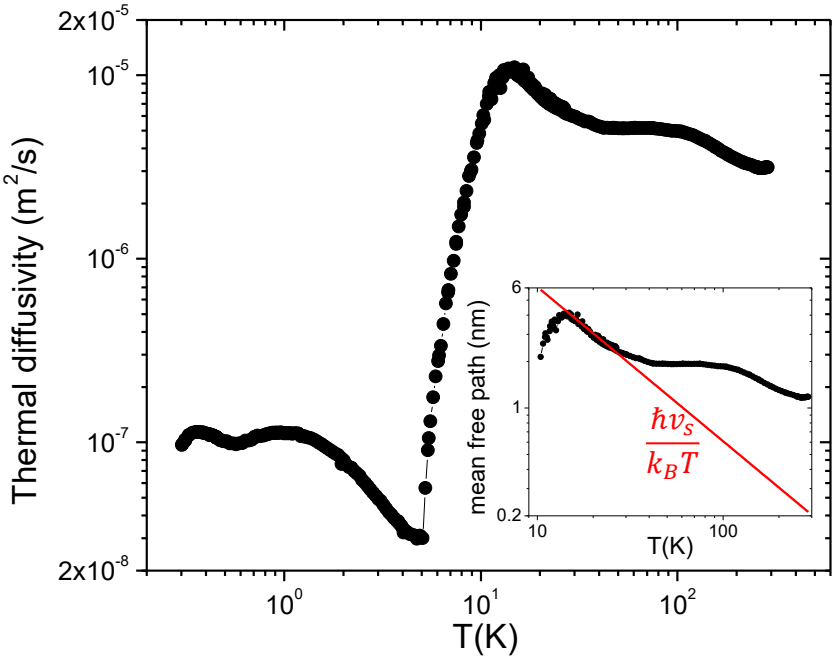

Fig. 5.12 **Thermal Diffusivity of $EuTiO_3$ and the mean-free-path of phonons:** *Temperature dependence of thermal diffusivity, D, by taking the ratio of thermal conductivity and the specific heat per volume in sample C1. Note the drastic drop across the magnetic transition. The insets show the Temperature dependence of the mean free path in the paramagnetic phase, assuming that all phonons have the same scattering time and velocity for the same sample. The red solid line represents the inverse of the wavevector of the thermally excited acoustic phonons.*

fig5.12

one can simply write $\kappa = 1/3Cv_s\ell_{ph}$. This neglects the q dependence of the scattering time and assumes that all modes have the same velocity. Taking v_s= 6.8 km/s, the measured sound velocity in STO [221], and in reasonable agreement with the dispersion of acoustic branches in ETO [186], one can estimate ℓ_{ph}, shown in the inset of Fig. 5.12. Comparing it to the inverse of the wave-vector of thermally excited phonons: $q_s = \frac{k_BT}{\hbar v_s}$, one finds that below 20 K, $q_s\ell_{ph} \cong 1$, reminiscent of the Anderson localization. There is a drop at 15K, below which specific heat is no more phonon-dominated.

5.3.6 Discussion on glass-like thermal conductivity

Evidence for coupling between spin and lattice degrees of freedom in this compound was first reported by Katsufuji and Takagi [21], who found that when the spins order at 5.5 K, the electric permittivity of ETO drops by 7 percent and this drop is suppressed by the application of a magnetic field of the order of 3 T. This magneto-electric effect implies coupling between Eu^{2+} spins and the soft mode governing the electric permittivity. Reuvekamp *et al.* [222] have found a quantitative agreement between the amplitude of the magneto-electric effect and the low-temperature magnetostriction of the system.

Our main finding is that lattice-spin coupling drastically attenuates the propagation of heat in ETO, even at temperatures where magnetic ordering is absent and magnetic entropy is practically saturated at its maximum value $k_B \ln(2S+1)$/spin. This implies that even when the spins are randomly oriented, heat-carrying phonons couple to Eu^{2+} states and their large magnetic moments (6.9-7 μ_B). According to ref. [189], without incorporating the loss of spin symmetry, the DFT calculations cannot explain the absence of metallicity and the finite band gap of the paramagnetic phase.

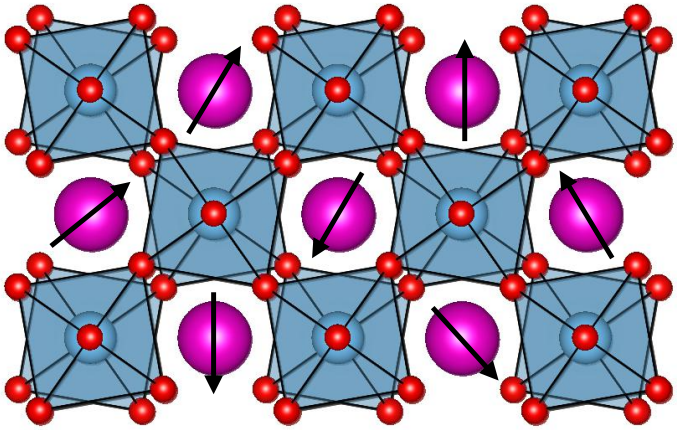

Fig. 5.13 **Crystal structure of $EuTiO_3$ in its paramagnetic phase:** *Random magnetic moments at Eu sites are located between TiO_6 octahedra, which are tilted off each other. Superexchange interaction between these spins involves Ti and oxygen atoms. This can impede phonons to have a well-defined wave vector over long distances.*

fig5.13

The random orientation of magnetic moments at Eu sites (See Fig. 5.13) is the most plausible source of phonon localization. The superexchange interaction between Eu spins occurs through Ti ions [223]. The inter-atomic force constant can depend on the relative orientation of spins. The calculated phonon frequencies for parallel or anti-parallel alignment of adjacent spins are not the same [224], which implies that phonons cannot keep a well-defined dispersion in the presence of random spin orientation.

The narrow energy separation between the Eu^{2+} energy level and the chemical potential may also play a role. In some Eu-based metals, the thermoelectric response has been linked to the temperature dependence of Eu valence [211]. Remarkably, a theoretical study [225] has concluded that the contribution of optical phonons to the overall lattice thermal conductivity is unusually large in this lattice structure. A coupling between heat-carrying optical phonons and Eu valence may be the source of observed κ attenuation.

Inelastic neutron scattering is a promising probe of this physics. In the case of $Tb_3Ga_5O_{12}$, for example, it documented the coupling between spin and lattice [226]). A recent study on STO [64] has found evidence for an unusual hybridization between acoustic and optic phonon branches. No neutron scattering data is presently available to compare ETO with STO.

Finally, let us note that the glass-like thermal conductivity of $EuTiO_3$, in contrast to spin-liquid crystals, occurs in a solid with a simple G-type anti-ferromagnetic ground state [183]. A formal theoretical treatment may be achieved by complementing the picture drawn

by Eq.5.1 with an 'off-diagonal' coupling between different vibrational states [198; 199; 206]:

$$\kappa_{od} = \sum_{ss',\mathbf{q}}^{s\neq s'} C_{ss'}(\mathbf{q})\mathbf{v}^{\mathbf{2}}_{\mathbf{ss'}}(\mathbf{q})\tau_{\mathbf{ss'}}(\mathbf{q}) \tag{5.2}$$ eq5.2

This equation was conceived for non-magnetic crystals, in which harmonic coupling occurs across phonon branches [198; 206]. It can be extended to magnetic modes.

5.4 Conclusion

This is the first detailed study of transport in bulk magnetic quantum paraelectric $EuTiO_3$. Resistivity, Hall effect, and Seebeck effect were measured down to 60 K. The negative Hall number and Seebeck coefficient and their temperature dependence show a semiconducting behavior and n-type carriers. The Arrhenius plot of resistivity and Hall carrier concentration and Seebeck coefficient versus T^{-1} yield an insulating band gap of ~ 0.22 eV which is close to the recent DFT calculation [189]. Both the Seebeck coefficient and resistivity show a kink around 260 K corresponding to the Antiferrodistortive transition which is believed to be similar to $SrTiO_3$. The hysteresis in the temperature dependence of resistivity implies a first-order transition. The most important result is that a glass-like thermal conductivity was found in $EuTiO_3$. Its amplitude above the Néel temperature is lower than $SrTiO_3$. Its field dependence points to the scattering of phonons by the magnetic excitations.

Conclusion

In this thesis, we addressed a series of thermal, electrical, and thermoelectric transport studies surrounding the perovskite quantum paraelectrics $SrTiO_3$ and $EuTiO_3$.

In the first part, motivated by the sizable phonon thermal Hall effect found in quantum paraelectric $SrTiO_3$, We studied its thermal Hall effect evolving with Ca substitution and O vacancies. When Sr is substituted by Ca stabilizing the ferroelectric order, the thermal Hall effect coming from the phonon is suppressed. Such suppression of the thermal Hall effect was also found in isotopic substitution (of $^{1}6O$ with $^{1}8O$) samples also with the stable ferroelectric order. These point to the role of ferroelectric fluctuations in generating the thermal Hall effect in $SrTiO_3$. Contrary to Ca substitution, the thermal Hall effect is amplified by removing oxygen atoms and the emergence of dilute metallicity. In this case, we identify a new source of the thermal Hall effect, which is phonon drag in the context of an exceptionally large electronic Hall angle. The coupling between two types of heat carriers, one with a long scattering time (here phonons) and another with a large Hall angle (here electrons) can be studied in other contexts such as insulating solid with ordinary phonons (with a long scattering time) and magnetic excitations a short scattering time and a large transverse response.

In the second part, we focused on the electronic thermal conductivity in Nb-doped $SrTiO_3$. In dilute metal, its electronic thermal conductivity is mixed up with phononic, thermoelectrical, and electron-phonon coupling contributions [108]. Here, found a self-consistent experimental way to extract the electronic thermal conductivity in two Nb-doped $SrTiO_3$ samples. By detecting the magnetic field response of thermal conductivity, We hypothesized that the ignored electron-phonon interaction and phonon contribution and the same field response in electrical and thermal conductivity (these hypotheses also be verified by experimental results), eventually extracted the electronic thermal conductivity and found a robust T-square thermal resistivity. The T-square resistivity and thermal resistivity observed in metallic strontium titanate make us consider it a Fermi liquid. However, there is no difference in the T-square thermal resistivity in metallic strontium titanate and the other Fermi liquids with Umklap scattering. Besides this, it also shows similarity with ^{3}He which is also absent of Umklap scattering. According to these results, we concluded that the electron transport behavior in dilute metal STO at least its T-square electrical and thermal conductivity at low temperatures can be considered a Fermi liquid. It proposed a new challenge for theory to understand the mechanism of the energy and momentum dispassion during electron-electron scattering in Fermi liquids.

In the third part, We studied the electric, thermoelectric, and thermal transport properties of $EuTiO_3$, another quantum paraelectric with an antiferromagnetic order at 5.5 K. The resistivity, Hall effect, and Seebeck effect were measured to 60 K because it becomes

insulating as cooling. The minus Hall conductivity and Seebeck coefficient and their temperature dependence show an intrinsic n-type semiconductor behavior. The Arrhenius plot of resistivity and Hall carrier concentration and Seebeck coefficient versus T^{-1} yield an insulating band gap of ~ 0.22 eV which is close to the recent DFT calculation [189]. Both the Seebeck coefficient and resistivity show a kink around 260 K corresponding to the Antiferrodistortive transition which is believed same as the $SrTiO_3$. While a hysteresis behavior of temperature dependence resistivity implies a first-order transition. Moreover, it displays a glass-like thermal conductivity and its amplitude above the Néel temperature is lower than $SrTiO_3$. Its field dependence points to the scattering of phonons by the magnetic excitations as the source of the glass-like behavior of thermal conductivity. The results provide an interesting challenge for the theory attempting to achieve a unified picture of thermal transport in crystals and glasses.

Appendices

Appendix A

Using thermocouple measure thermal conductivity

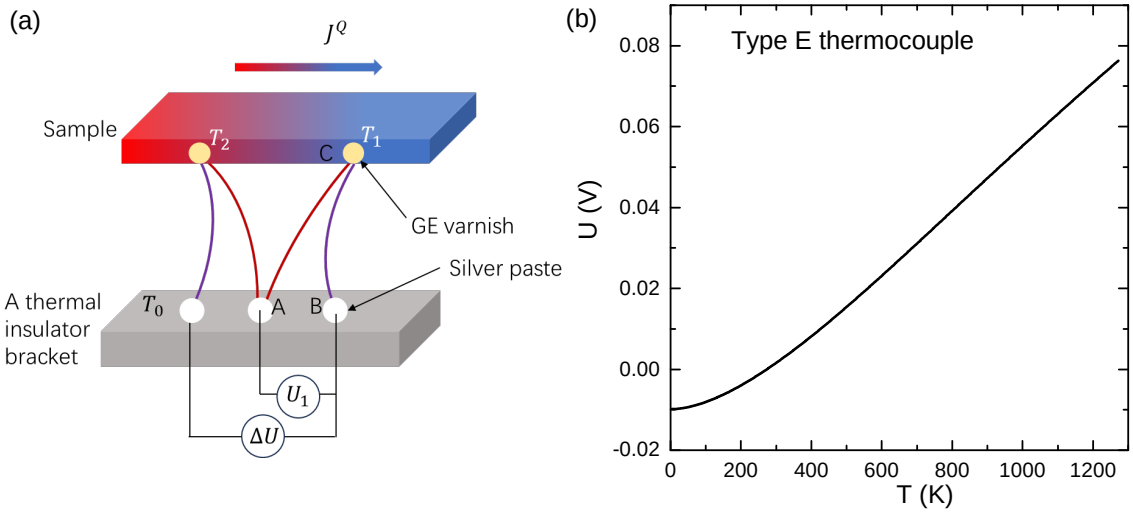

Fig. A.1 *(a) Sketch of the setup by using thermocouples measure the thermal conductivity. One thermocouple consists of a Nickel-Chromium wire (purple line) and a Constantan (red line) and junction C (which is glued on the sample by GE varnish) and endpoints A and B(which are glued on a thermal insulator bracket by sliver paste). The temperature difference between T_0 and T_1 T_2 leads to a detectable voltage signal U_1 and ΔU because of the different Seebeck coefficient between Nickel-Chromium and Constantan. ΔU is the difference signal of the two thermocouples. (b) is the voltage-temperature calibration curve of type E thermocouple. The temperature of endpoints A and B are fixed at 273.15 K (0 ^oC), and the temperature of the junction is the x axis.*

fig.ap1

In Chapter 5, we used thermocouples to measure the thermal conductivity at a high-temperature range. Fig A.1 (a) shows the sketch of the setup. The junction of the thermocouple is glued on the sample with a temperature T_1 or T_2, and the other two endpoints A and B are glued to a thermal insulator bracket which has a homogeneous temperature T_0.

This setup is used in PPMS. During the measurement, T_0 equals the system temperature of PPMS. T_1 and T_2 can be acquired by detecting the voltage U_1 and ΔU as shown in Fig A.1 (a). Then I will show how can we get T_1 and T_2 by using the detected voltage U_1 and ΔU and the standard calibration curve shown in Fig A.1 (b). The calibration curve is acquired by fixing the temperature of the two endpoints A and B at 273.15 K. The voltage U_1 only responds to the signal of $T_1 - T_0$, so we need first add an extra voltage $U(T_0)$ to U_1 and then use the calibration curve to acquire the absolute temperature T_1. It is also the same for T_2. After we have the T_1 and T_2, then the temperature difference is equal to $T_1 - T_2$, at the end by using Eq 1.3 we can acquire the thermal conductivity. We note that the Seebeck coefficients of thermocouples increase with temperature, so it is usually used in the high-temperature range.

Appendix B

Résumé long en français

B.1 Résumé en français

Dans cette thèse, nous avons étudié systématiquement les propriétés de transport thermique dans deux matériaux diélectriques quantiques : le titanate de strontium ($SrTiO_3$) et le titanate d'europium ($EuTiO_3$).

Dans la première partie, nous avons présenté une étude sur l'effet Hall thermique dans $SrTiO_3$ en évolution avec la substitution atomique. Lorsque le Sr est substitué par le Ca stabilisant l'ordre ferroélectrique, l'effet Hall thermique provenant du phonon est supprimé, ce qui souligne le rôle des fluctuations ferroélectriques dans la génération de cet effet. Il est amplifié en retirant les atomes d'oxygène et par l'émergence de la métallicité diluée. Dans ce cas, nous identifions une nouvelle source de l'effet Hall thermique, qui est le phénomène de traînée du phonon dans le contexte d'un angle de Hall électronique exceptionnellement grand.

Dans la deuxième partie, nous nous concentrons sur la conductivité thermique électronique dans $SrTiO_3$ dopé au Nb. En séparant les contributions électroniques et phononiques au transport de chaleur, nous extrayons la résistivité thermique électronique et montrons qu'elle présente une dépendance en température au carré (T-square). En comparaison avec sa résistivité électrique T-square, nous constatons que la loi de Wiedemann-Franz est strictement respectée dans la limite de température zéro, mais les préfacteurs T-square sont différents d'un facteur d'environ ≈ 3. Cela est similaire à d'autres liquides de Fermi. En se rappelant du cas de ^{3}He, nous soutenons que la résistivité thermique T-square ne nécessite pas d'événements Umklapp. La récupération approximative de la loi de Wiedemann-Franz en présence de désordre pourrait expliquer une résistivité électrique T-square sans Umklapp.

Dans la troisième partie, nous avons étudié les propriétés de transport électrique, thermoélectrique et thermique du $EuTiO_3$. La dépendance en température de la résistivité électrique et du coefficient Seebeck nous a permis de conclure que la bande interdite isolante est de 0,22 eV. De plus, la conductivité thermique de $EuTiO_3$ est considérablement réduite et présente une amplitude et une dépendance en température similaires à celles de la silice amorphe. Après avoir exclu les impuretés Eu^{+3}, nous avons proposé deux mécanismes qui entravent la conductivité thermique dans $EuTiO_3$: l'une est la fluctuation de valence. L'énergie du plus haut phonon optique dans cette structure cristalline et la distance entre le niveau f de Eu et le potentiel chimique sont toutes deux d'environ 0,1 eV. L'autre est

l'interaction de superéchange entre les spins Eu qui se produit à travers les ions Ti.

B.2 Introduction en français

Lorsqu'un système est contraint de sortir de l'équilibre, il aura tendance à revenir à l'état d'équilibre. C'est le cas dans les phénomènes de transport. Dans les solides, la différence de potentiel conduit les électrons à se déplacer du côté à fort potentiel électrique vers le côté à faible potentiel, et la différence de température entraîne un flux de chaleur des parties plus chaudes vers les plus froides. Ces deux phénomènes sont appelés transport électrique et transport thermique. En physique de la matière condensée, le transport électrique et thermique dans les solides, généralement provoqué par les électrons et les phonons, peuvent être décrits par l'équation de transport de Boltzmann dans une image semi-classique. Néanmoins, l'interaction entre ces deux types de quasi-particules peut donner naissance à des propriétés émergentes telles que la supraconductivité ou l'effet de traînée des phonons qui méritent d'être étudiées. C'est le cas dans le pérovskite titanate de strontium ($SrTiO_3$) et son homologue le titanate d'europium ($EuTiO_3$) qui ont récemment suscité beaucoup d'attention.

Le pérovskite titanate de strontium ($SrTiO_3$) est connu depuis longtemps. C'est un paraélectrique quantique : l'instabilité ferroélectrique est supprimée en raison des fluctuations quantiques [1]. L'ordre ferroélectrique peut être stabilisé par de petites substitutions chimiques (en remplaçant Sr par Ca [2] ou Ba [3], ou en substituant ^{16}O par ^{18}O [4]). Le $SrTiO_3$ pur est un isolant avec une grande bande interdite, mais il peut facilement être transformé en métal en introduisant une faible concentration de dopants (vacances d'oxygène, Nb ou dopage au La) en raison de sa grande permittivité [5]. Ce métal a un état fondamental supraconducteur dilué.

Le sujet de cette thèse porte sur le transport thermique dans deux matériaux paraélectriques quantiques. Il consiste en une étude de l'évolution du transport thermique avec la substitution atomique dans le $SrTiO_3$, ainsi qu'une première étude du transport thermique dans l'$EuTiO_3$, un matériau étroitement apparenté avec la particularité d'être ordonné magnétiquement. La thèse est divisée en trois parties.

La première partie est consacrée à l'effet Hall thermique (THE) dans le $SrTiO_3$ et à sa variation avec la substitution atomique. Le THE est l'analogue thermique de l'effet Hall électrique. Au lieu d'une tension transversale induite par un champ magnétique perpendiculaire en présence d'un courant électrique, une différence de température transversale est générée en présence d'un courant thermique. Dans les métaux, l'existence d'un tel effet n'est pas surprenante, car les porteurs de chaleur chargés sont influencés par la force de Lorentz. Il s'agit d'un effet thermique Hall électronique lié à l'effet Hall électrique par la loi de Wiedemann-Franz. En revanche, la présence d'un tel effet dans les isolants n'est pas comprise. L'effet THE des phonons a d'abord été observé dans l'isolant paramagnétique $Tb_3Ga5O12$ [7; 8] et attribué à la diffusion oblique des phonons par des impuretés magnétiques Tb super-stœchiométriques. Par la suite, il a également été observé dans des matériaux non magnétiques (comme le $SrTiO_3$ [9]), où l'origine phonique du THE ne fait pas débat. De nombreuses scénarios théoriques ont été proposés pour expliquer comment les phonons peuvent générer un THE. Ils peuvent être classés en intrinsèques (invoquant les particularités du spectre des phonons) ou extrinsèques (se référant à des mécanismes de

diffusion phononique spécifiques). Jusqu'à présent, l'origine du THE des phonons reste une question ouverte.

Poursuivant les études précédentes sur le $SrTiO_3$, j'ai mesuré pour la première fois l'effet Hall thermique dans des échantillons de $SrTiO_3$ substitués au calcium et réduits en oxygène. Cette étude a révélé que la substitution du calcium, qui stabilise l'ordre ferroélectrique, réduit considérablement le THE, ce qui implique que l'ordre ferroélectrique nuit à l'effet THE. D'autre part, j'ai constaté que dans les échantillons réduits en oxygène, l'effet THE est plus important que dans le STO pur. De manière surprenante, dans le STO métallique dilué, l'amplitude de l'effet THE dépasse la somme des contributions électronique et phonique [attendues]. Nous avons avancé l'argument que cela peut s'expliquer en invoquant la traînée entre les électrons et les phonons. Dans notre plage de température d'intérêt, la chaleur est presque exclusivement transportée par les phonons, mais l'angle de Hall électronique est bien plus élevé que l'angle de Hall phononique. La combinaison de ces deux caractéristiques avec des échanges fréquents de moment entre les phonons et les électrons peut constituer une source supplémentaire de l'effet Hall thermique. C'est la première fois que des signatures de la traînée des phonons ont été observées par une sonde purement thermique (et non thermélectrique).

La deuxième partie contribue au débat en cours sur l'origine de la résistivité quadratique en fonction de la température dans les métaux dilués. Dans les liquides de Fermi, la collision entre les électrons est connue pour générer une contribution à la résistivité électrique croissant avec le carré de la température. Cela correspond à la dépendance en température de l'espace de phase pour la diffusion électron-électron. Les électrons participant à une collision résident tous deux dans une fenêtre thermique du niveau de Fermi. Par conséquent, le principe d'exclusion de Pauli est appliqué deux fois, d'où une dépendance quadratique en température. Cependant, la source microscopique de la dissipation n'est pas évidente. Pour expliquer comment les collisions électron-électron entraînent des pertes de moment, deux scénarios ont été proposés. Le premier invoque les événements Umklapp, qui sont des collisions où la somme des deux vecteurs d'onde en collision devient plus grande que la largeur de la zone de Brillouin. Le deuxième scénario invoque la présence de réservoirs électroniques multiples. Dans ce contexte, l'observation de la résistivité en carré T dans deux métaux dilués, à savoir le $SrTiO_3$ et le Bi_2O_2Se, est énigmatique. En effet, aucun de ces deux scénarios ne s'applique dans ces cas. Dans le cas du $SrTiO_3$, il a été proposé que la diffusion en carré T pourrait être causée par la diffusion des électrons par deux phonons optiques mous [18; 19]. Ce scénario ne s'applique pas au Bi_2O_2Se.

La deuxième partie de ma thèse porte sur le pendant thermique de la résistivité en carré T dans le $SrTiO_3$ métallique dilué. J'ai étudié la conductivité thermique électronique du STO dopé au Nb à deux concentrations de porteurs. Malgré la dominance de la composante du réseau de la conductivité thermique, nous avons réussi à extraire la contribution électronique au transport de chaleur en exploitant l'effet différenciateur du champ magnétique sur les phonons et les électrons. Nous avons constaté que la résistivité thermique $W\mathrm{T}$ ($W = \kappa^{-1}$) suit un comportement en carré T et que son préfacteur est supérieur à celui de sa contrepartie électrique d'un facteur d'environ 3. Cela n'est pas compatible avec ce qui est attendu dans le scénario basé sur les phonons, où la diffusion quasi-élastique devrait conduire à une égalité parfaite entre les deux préfacteurs. Ainsi, la résistivité en carré T du STO dopé au Nb ne peut pas être distinguée des autres métaux où l'origine électron-électron de la résistivité en carré T ne fait pas débat. Cela nous amène à conclure que la résistivité en carré T (électrique

et thermique) peut être causée sans Umklapp comme conséquence de la diminution en carré T de l'amplitude de la diffusivité (de moment et d'énergie) dans un liquide de Fermi causée par la diffusion fermion-fermion. Une théorie complète de ce phénomène doit encore être élaborée.

Dans la troisième partie, l'attention se porte sur un autre paraélectrique quantique, l'$EuTiO_3$. Comme le $SrTiO_3$, l'$EuTiO_3$ a une structure cubique à température ambiante et subit également une transition antiferrodistortive où les octaèdres TiO_6 adjacents tournent dans des directions opposées. Tout comme le $SrTiO_3$, il présente un comportement paraélectrique quantique, mais de manière beaucoup plus atténuée [21] : sa constante diélectrique atteint 300, contre 20000 dans le $SrTiO_3$. Les électrons Eu $f-$ sont ordonnés antiferromagnétiquement en dessous de $T_N = 5{,}5K$ [21]. Fait intéressant, la constante diélectrique montre une cuspide à cette température. Ce couplage magnéto-électrique [22] a fait l'objet de recherches théoriques et expérimentales.

Nous avons étudié les propriétés électriques, thermélectriques et thermiques de l'$EuTiO_3$. La dépendance en température de la résistivité électrique et du coefficient Seebeck nous a permis de conclure que la bande interdite isolante est d'environ 0,22 eV. De plus, la conductivité thermique de l'$EuTiO_3$ est considérablement réduite et présente une amplitude et une dépendance en température similaires à celles de la silice amorphe. Une comparaison avec d'autres solides paraélectriques quantiques, à savoir le $SrTiO_3$ et le $KTaO_3$, montre que les spins $4f$ au niveau des sites Eu^{2+} entravent considérablement le transport de chaleur par les phonons bien au-dessus de la température de transition magnétique. Ce résultat constitue un nouveau défi pour la théorie qui tente d'élaborer une vision unifiée du transport de chaleur dans les cristaux et les verres.

Les trois ensembles de résultats sont détaillés dans les chapitres trois à cinq de ce manuscrit. Le premier chapitre donnera un aperçu de la théorie du transport et des techniques expérimentales. Le deuxième chapitre est une présentation du contexte de la recherche introduisant les matériaux paraélectriques quantiques.

Bibliography

Example of Content inserted after chapter title and list

Muller1979 [1] K. A. Müller & H. Burkard; "$SrTiO_3$: An intrinsic quantum paraelectric below 4 K"; Phys. Rev. B **19**, p. 3593–3602 (1979). https://link.aps.org/doi/10.1103/PhysRevB.19.3593. Cited pages xi, 22, and 92

bednorz1984 [2] J. Bednorz & K. Müller; "$Sr_{1-x}Ca_xTiO_3$: an XY quantum ferroelectric with transition to randomness"; Physical Review Letters **52**, p. 2289 (1984). Cited pages xi, 22, 23, 36, and 92

lemanov1996 [3] V. Lemanov, E. Smirnova, P. Syrnikov & E. Tarakanov; "Phase transitions and glasslike behavior in $Sr_{1-x}Ba_xTiO_3$"; Physical Review B **54**, p. 3151 (1996). Cited pages xi, 22, and 92

itoh1999 [4] M. Itoh, R. Wang, Y. Inaguma, T. Yamaguchi, Y. Shan & T. Nakamura; "Ferroelectricity induced by oxygen isotope exchange in strontium titanate perovskite"; Physical Review Letters **82**, p. 3540 (1999). Cited pages xi, 21, 22, 36, and 92

collignon2019 [5] C. Collignon, X. Lin, C. W. Rischau, B. Fauqué & K. Behnia; "Metallicity and superconductivity in doped strontium titanate"; Annual Review of Condensed Matter Physics **10**, p. 25–44 (2019). Cited pages xi, 23, 24, 25, 26, 54, 66, 72, and 92

gastiasoro2020 [6] M. N. Gastiasoro, J. Ruhman & R. M. Fernandes; "Superconductivity in dilute $SrTiO_3$: A review"; Annals of Physics **417**, p. 168 107 (2020). Cited pages xi and 26

strohm2005 [7] C. Strohm, G. Rikken & P. Wyder; "Phenomenological evidence for the phonon Hall effect"; Physical review letters **95**, p. 155 901 (2005). Cited pages xi, 31, 32, and 92

inyushkin2007 [8] A. V. Inyushkin & A. Taldenkov; "On the phonon Hall effect in a paramagnetic dielectric"; Jetp Letters **86**, p. 379–382 (2007). Cited pages xi, 31, and 92

li2018 [9] S. Li & D. L. Maslov; "Lorentz ratio of a compensated metal"; Physical Review B **98**, p. 245 134 (2018). Cited pages xi, 27, 31, 32, and 92

sheng2006 [10] L. Sheng, D. Sheng & C. Ting; "Theory of the phonon Hall effect in paramagnetic dielectrics"; Physical review letters **96**, p. 155 901 (2006). Cited page xi

chen2020 [11] J.-Y. Chen, S. A. Kivelson & X.-Q. Sun; "Enhanced thermal Hall effect in nearly ferroelectric insulators"; Physical Review Letters **124**, p. 167 601 (2020). Cited pages xi, 33, and 36

mangeolle2022 [12] L. Mangeolle, L. Balents & L. Savary; "Phonon thermal hall conductivity from

scattering with collective fluctuations"; Physical Review X **12**, p. 041 031 (2022). Cited page xi

guo2022 [13] H. GUO, D. G. JOSHI & S. SACHDEV; "Resonant thermal Hall effect of phonons coupled to dynamical defects"; Proceedings of the National Academy of Sciences **119**, p. e2215141 119 (2022). Cited page xi

Yamada1986 [14] K. YAMADA & K. YOSIDA; "Fermi liquid theory on the basis of the periodic Anderson Hamiltonian"; Progress of theoretical physics **76**, p. 621–638 (1986). Cited pages xii, 5, 26, and 54

Maebashi [15] H. MAEBASHI & H. FUKUYAMA; "Electrical Conductivity of Interacting Fermions. I. General Formulation"; Journal of the Physical Society of Japan **66**, p. 3577–3590 (1997). Cited page xii

Baber1937 [16] W. BABER; "The contribution to the electrical resistance of metals from collisions between electrons"; Proceedings of the Royal Society of London. Series A-Mathematical and Physical Sciences **158**, p. 383–396 (1937). Cited pages xii, 5, 26, 53, and 54

Rice1968 [17] M. RICE; "Electron-electron scattering in transition metals"; Physical Review Letters **20**, p. 1439 (1968). Cited pages xii, 5, and 54

Maslov2016 [18] D. L. MASLOV & A. V. CHUBUKOV; "Optical response of correlated electron systems"; Reports on Progress in Physics **80**, p. 026 503 (2016). Cited pages xii and 93

epifanov1981 [19] Y. N. EPIFANOV, A. LEVANYUK & G. LEVANYUK; "Interaction of carriers with to-phonons and electrical conductivity of ferroelectrics"; Ferroelectrics **35**, p. 199–202 (1981). Cited pages xii and 93

Wang2020 [20] J. WANG, J. WU, T. WANG, Z. XU, J. WU, W. HU, Z. REN, S. LIU, K. BEHNIA & X. LIN; "T-square resistivity without Umklapp scattering in dilute metallic Bi_2O_2Se"; Nature Communications **11**, p. 3846 (2020). Cited pages xii, 5, 54, and 55

katsufuji2001 [21] T. KATSUFUJI & H. TAKAGI; "Coupling between magnetism and dielectric properties in quantum paraelectric $EuTiO_3$"; Physical Review B **64**, p. 054 415 (2001). Cited pages xiii, 29, 30, 69, 82, and 94

n_Holder_2012 [22] A. BUSSMANN-HOLDER, Z. GUGUCHIA, J. KÖHLER, H. KELLER, A. SHENGELAYA & A. R. BISHOP; "Hybrid paramagnon phonon modes at elevated temperatures in $EuTiO_3$"; New Journal of Physics **14**, p. 093 013 (2012). https://doi.org/10.1088/1367-2630/14/9/093013. Cited pages xiii, 71, 72, 73, 81, and 94

sears1975 [23] F. W. SEARS & G. L. SALINGER; "Thermodynamics, kinetic theory, and statistical thermodynamics"; (No Title) (1975). Cited page 2

behnia2015 [24] K. BEHNIA; *Fundamentals of thermoelectricity* (OUP Oxford) (2015). Cited pages 2, 9, 12, 25, 51, and 71

idemantel2003 [25] T. SCHEIDEMANTEL, C. AMBROSCH-DRAXL, T. THONHAUSER, J. BADDING & J. O. SOFO; "Transport coefficients from first-principles calculations"; Physical Review B **68**, p. 125 210 (2003). Cited page 2

messiah2014 [26] A. MESSIAH; *Quantum mechanics* (Courier Corporation) (2014). Cited page 3

ashcroft2022 [27] N. W. ASHCROFT & N. D. MERMIN; *Solid state physics* (Cengage Learning) (2022).

Cited pages 4 and 5

franz1853 [28] R. Franz & G. Wiedemann; "Ueber die wärme-leitungsfähigkeit der metalle"; Annalen der Physik **165**, p. 497–531 (1853). Cited page 5

ziman1972 [29] J. M. Ziman; *Principles of the Theory of Solids* (Cambridge university press) (1972). Cited pages 5, 6, 8, and 55

berman1978 [30] R. Berman & P. G. Klemens; "Thermal conduction in solids"; Physics Today **31**, p. 56 (1978). Cited page 5

Maebashi1998 [31] H. Maebashi & H. Fukuyama; "Electrical conductivity of interacting fermions. II. Effects of normal scattering processes in the presence of Umklapp scattering processes"; Journal of the Physical Society of Japan **67**, p. 242–251 (1998). Cited pages 5, 26, and 54

Lin2015sc [32] X. Lin, B. Fauqué & K. Behnia; "Scalable T^2 resistivity in a small single-component Fermi surface"; Science **349**, p. 945–948 (2015). Cited page 5

debye1912 [33] P. Debye; "Zur theorie der spezifischen wärmen"; Annalen der Physik **344**, p. 789–839 (1912). Cited page 7

yang2004 [34] J. Yang; "Theory of thermal conductivity"; Thermal Conductivity: Theory, Properties, and Applications p. 1–20 (2004). Cited page 7

peierls1929 [35] R. Peierls; "Zur kinetischen theorie der wärmeleitung in kristallen"; Annalen der Physik **395**, p. 1055–1101 (1929). Cited pages 8 and 74

gurzhi1968 [36] R. Gurzhi; "Hydrodynamic effects in solids at low temperature"; Soviet Physics Uspekhi **11**, p. 255 (1968). Cited pages 8 and 51

homlinson1969 [37] W. C. Thomlinson; "Evidence for anomalous phonon excitations in solid He 3"; Physical Review Letters **23**, p. 1330 (1969). Cited page 8

kopylov1973 [38] V. Kopylov & L. Mezhov-Deglin; "Study of kinetic coefficients of bismuth at helium temperatures"; Zhurnal Ehksperimental'noj i Teoreticheskoj Fiziki **65**, p. 720–734 (1973). Cited page 8

zholonko2006 [39] N. Zholonko; "Poiseuille flow of phonons in solid hydrogen"; Physics of the Solid State **48**, p. 1678–1680 (2006). Cited page 8

martelli2018 [40] V. Martelli, J. L. Jiménez, M. Continentino, E. Baggio-Saitovitch & K. Behnia; "Thermal transport and phonon hydrodynamics in strontium titanate"; Physical review letters **120**, p. 125 901 (2018). Cited pages 8, 27, 36, 63, 79, and 80

machida2018 [41] Y. Machida, A. Subedi, K. Akiba, A. Miyake, M. Tokunaga, Y. Akahama, K. Izawa & K. Behnia; "Observation of Poiseuille flow of phonons in black phosphorus"; Science advances **4**, p. eaat3374 (2018). Cited page 8

mott1958 [42] N. F. Mott, H. Jones, H. Jones & H. Jones; *The theory of the properties of metals and alloys* (Courier Dover Publications) (1958). Cited page 12

goldsmid2010 [43] H. J. Goldsmid *et al.*; *Introduction to thermoelectricity*; tome 121 (Springer) (2010). Cited page 13

machida2020 [44] Y. Machida, N. Matsumoto, T. Isono & K. Behnia; "Phonon hydrodynamics and ultrahigh–room-temperature thermal conductivity in thin graphite"; Science **367**, p. 309–312 (2020). Cited page 14

tilley2016 [45] R. J. Tilley; *Perovskites: structure-property relationships* (John Wiley & Sons) (2016). Cited page 19

lytle1964 [46] F. W. Lytle; "X-ray diffractometry of low-temperature phase transformations in strontium titanate"; Journal of Applied Physics **35**, p. 2212–2215 (1964). Cited pages 19 and 72

unoki1967 [47] H. Unoki & T. Sakudo; "Electron spin resonance of Fe^{3+} in $SrTiO_3$ with special reference to the 110 K phase transition"; Journal of the Physical Society of Japan **23**, p. 546–552 (1967). Cited page 20

salje1998 [48] E. Salje, M. Gallardo, J. Jiménez, F. Romero & J. Del Cerro; "The cubic-tetragonal phase transition in strontium titanate: excess specific heat measurements and evidence for a near-tricritical, mean field type transition mechanism"; Journal of Physics: Condensed Matter **10**, p. 5535 (1998). Cited pages 20 and 21

muller1970 [49] K. Müller, W. Berlinger, M. Capizzi & H. Gränicher; "Monodomain strontium titanate"; Solid State Communications **8**, p. 549–553 (1970). Cited page 20

bauerle1978 [50] D. Bäuerle & W. Rehwald; "Structural phase transitions in semiconducting $SrTiO_3$"; Solid State Communications **27**, p. 1343–1346 (1978). Cited page 21

tao2016 [51] Q. Tao, B. Loret, B. Xu, X. Yang, C. W. Rischau, X. Lin, B. Fauqué, M. J. Verstraete & K. Behnia; "Nonmonotonic anisotropy in charge conduction induced by antiferrodistortive transition in metallic $SrTiO_3$"; Physical Review B **94**, p. 035 111 (2016). Cited page 21

de2015 [52] B. De Lima, M. Da Luz, F. Oliveira, L. Alves, C. Dos Santos, F. Jomard, Y. Sidis, P. Bourges, S. Harms, C. Grams *et al.*; "Interplay between antiferrodistortive, ferroelectric, and superconducting instabilities in $Sr_{1-x}Ca_xTiO_{3-\delta}$"; Physical Review B **91**, p. 045 108 (2015). Cited pages 21 and 34

smirnova2005 [53] E. Smirnova, A. Sotnikov, R. Kunze, M. Weihnacht, O. Kvyatkovskii & V. Lemanov; "Interrelation of antiferrodistortive and ferroelectric phase transitions in $Sr_{1-x}A_xTiO_3$ (A= Ba, Pb)"; Solid state communications **133**, p. 421–425 (2005). Cited page 21

mccalla2016 [54] E. McCalla, J. Walter & C. Leighton; "A unified view of the substitution-dependent antiferrodistortive phase transition in $SrTiO_3$"; Chemistry of Materials **28**, p. 7973–7981 (2016). Cited page 21

shirane1969 [55] G. Shirane & Y. Yamada; "Lattice-dynamical study of the 110 K phase transition in $SrTiO_3$"; Physical Review **177**, p. 858 (1969). Cited page 21

vogt1995 [56] H. Vogt; "Refined treatment of the model of linearly coupled anharmonic oscillators and its application to the temperature dependence of the zone-center soft-mode frequencies of $KTaO_3$ and $SrTiO_3$"; Physical Review B **51**, p. 8046 (1995). Cited page 22

hehlen1999 [57] B. Hehlen, L. Arzel, A. Tagantsev, E. Courtens, Y. Inaba, A. Yamanaka & K. Inoue; "Observation of the coupling between TA and TO modes in $SrTiO_3$ by Brillouin scattering"; Physica B: Condensed Matter **263**, p. 627–631 (1999). Cited page 22

fleury1968 [58] P. Fleury, J. Scott & J. Worlock; "Soft phonon modes and the 110 K phase transition in SrTi O 3"; Physical Review Letters **21**, p. 16 (1968). Cited page 21

uwe1976 [59] H. Uwe & T. Sakudo; "Stress-induced ferroelectricity and soft phonon modes in

SrTi O 3"; Physical Review B **13**, p. 271 (1976). Cited pages 21 and 22

Schneider1976 [60] T. Schneider, H. Beck & E. Stoll; "Quantum effects in an n-component vector model for structural phase transitions"; Phys. Rev. B **13**, p. 1123–1130 (1976). https://link.aps.org/doi/10.1103/PhysRevB.13.1123. Cited page 22

esswein2022 [61] T. Esswein & N. A. Spaldin; "Ferroelectric, quantum paraelectric, or paraelectric? Calculating the evolution from $BaTiO_3$ to $SrTiO_3$ to $KTaO_3$ using a single-particle quantum mechanical description of the ions"; Physical Review Research **4**, p. 033 020 (2022). Cited pages 22 and 23

rowley2014 [62] S. Rowley, L. Spalek, R. Smith, M. Dean, M. Itoh, J. Scott, G. Lonzarich & S. Saxena; "Ferroelectric quantum criticality"; Nature Physics **10**, p. 367–372 (2014). Cited page 22

chandra2017 [63] P. Chandra, G. G. Lonzarich, S. Rowley & J. Scott; "Prospects and applications near ferroelectric quantum phase transitions: a key issues review"; Reports on Progress in Physics **80**, p. 112 502 (2017). Cited page 22

fauque2022 [64] B. Fauqué, P. Bourges, A. Subedi, K. Behnia, B. Baptiste, B. Roessli, T. Fennell, S. Raymond & P. Steffens; "Mesoscopic fluctuating domains in strontium titanate"; Physical Review B **106**, p. L140 301 (2022). Cited pages 22 and 83

Verri2023 [65] G. G. Guzmán-Verri, C. H. Liang & P. B. Littlewood; "Lamellar Fluctuations Melt Ferroelectricity"; Phys. Rev. Lett. **131**, p. 046 801 (2023). https://link.aps.org/doi/10.1103/PhysRevLett.131.046801. Cited page 22

Muller1991 [66] K. A. Müller, W. Berlinger & E. Tosatti; "Indication for a novel phase in the quantum paraelectric regime of $SrTiO_3$"; Zeitschrift für Physik B Condensed Matter **84**, p. 277–283 (1991). ISSN 1431-584X. https://doi.org/10.1007/BF01313549. Cited page 22

itoh2003 [67] M. Itoh & R. Wang; "Universal relation between oxygen mass and T_c in $SrTiO_3$"; Journal of the Physical Society of Japan **72**, p. 1310–1311 (2003). Cited page 23

rischau2017 [68] C. W. Rischau, X. Lin, C. P. Grams, D. Finck, S. Harms, J. Engelmayer, T. Lorenz, Y. Gallais, B. Fauque, J. Hemberger *et al.*; "A ferroelectric quantum phase transition inside the superconducting dome of $Sr_{1-x}Ca_xTiO_{3-\delta}$"; Nature Physics **13**, p. 643–648 (2017). Cited pages 23, 25, and 36

hemberger1995 [69] J. Hemberger, P. Lunkenheimer, R. Viana, R. Böhmer & A. Loidl; "Electric-field-dependent dielectric constant and nonlinear susceptibility in $SrTiO_3$"; Physical Review B **52**, p. 13 159 (1995). Cited page 22

edge2015 [70] J. M. Edge, Y. Kedem, U. Aschauer, N. A. Spaldin & A. V. Balatsky; "Quantum critical origin of the superconducting dome in $SrTiO_3$"; Physical Review Letters **115**, p. 247 002 (2015). Cited page 23

bianchi1994 [71] U. Bianchi, W. Kleemann & J. Bednorz; "Raman scattering of ferroelectric $Sr1-xCa_xTiO_3$, $x = 0.007$"; Journal of Physics: Condensed Matter **6**, p. 1229 (1994). Cited page 24

wang1998 [72] Y. Wang, W. Kleemann, W. Zhong & L. Zhang; "Impurity-induced phase transition in quantum paraelectrics"; Physical Review B **57**, p. 13 343 (1998). Cited page 24

shirai2013 [73] K. Shirai & K. Yamanaka; "Mechanism behind the high thermoelectric power factor of $SrTiO_3$ by calculating the transport coefficients"; Journal of Applied Physics **113**, p. 053 705 (2013). Cited page 24

van2001 [74] K. Van Benthem, C. Elsässer & R. French; "Bulk electronic structure of $SrTiO_3$: Experiment and theory"; Journal of applied physics **90**, p. 6156–6164 (2001). Cited page 24

piskunov2004 [75] S. Piskunov, E. Heifets, R. Eglitis & G. Borstel; "Bulk properties and electronic structure of $SrTiO_3$, $BaTiO_3$, $PbTiO_3$ perovskites: an ab initio HF/DFT study"; Computational Materials Science **29**, p. 165–178 (2004). Cited page 24

Marel2011 [76] D. van der Marel, J. L. M. van Mechelen & I. I. Mazin; "Common Fermi-liquid origin of T^2 resistivity and superconductivity in n-type $SrTiO_3$"; Phys. Rev. B **84**, p. 205 111 (2011). https://link.aps.org/doi/10.1103/PhysRevB.84.205111. Cited pages 24 and 64

lin2013 [77] X. Lin, Z. Zhu, B. Fauqué & K. Behnia; "Fermi surface of the most dilute superconductor"; Physical Review X **3**, p. 021 002 (2013). Cited pages 25, 34, 46, 47, 49, 54, and 64

lin2014 [78] X. Lin, G. Bridoux, A. Gourgout, G. Seyfarth, S. Krämer, M. Nardone, B. Fauqué & K. Behnia; "Critical doping for the onset of a two-band superconducting ground state in $SrTiO_{3-\delta}$"; Physical Review Letters **112**, p. 207 002 (2014). Cited pages 25, 54, 63, and 64

van2011 [79] D. Van Der Marel, J. L. M. van Mechelen & I. Mazin; "Common Fermi-liquid origin of T 2 resistivity and superconductivity in n-type $SrTiO_3$"; Physical Review B **84**, p. 205 111 (2011). Cited page 25

allen2013 [80] S. J. Allen, B. Jalan, S. Lee, D. G. Ouellette, G. Khalsa, J. Jaroszynski, S. Stemmer & A. H. MacDonald; "Conduction-band edge and Shubnikov–de Haas effect in low-electron-density $SrTiO_3$"; Physical Review B **88**, p. 045 114 (2013). Cited pages 25 and 64

ttacharya2016 [81] A. Bhattacharya, B. Skinner, G. Khalsa & A. V. Suslov; "Spatially inhomogeneous electron state deep in the extreme quantum limit of strontium titanate"; Nature communications **7**, p. 12 974 (2016). Cited page 25

edwards1978 [82] P. P. Edwards & M. J. Sienko; "Universality aspects of the metal-nonmetal transition in condensed media"; Physical Review B **17**, p. 2575 (1978). Cited page 25

lin2015 [83] X. Lin, B. Fauqué & K. Behnia; "Scalable T^2 resistivity in a small single-component Fermi surface"; Science **349**, p. 945–948 (2015). Cited pages 25, 26, 35, and 50

kadowaki1986 [84] K. Kadowaki & S. Woods; "Universal relationship of the resistivity and specific heat in heavy-fermion compounds"; Solid state communications **58**, p. 507–509 (1986). Cited pages 26 and 54

schooley1965 [85] J. Schooley, W. Hosler, E. Ambler, J. Becker, M. L. Cohen & C. Koonce; "Dependence of the superconducting transition temperature on carrier concentration in semiconducting $SrTiO_3$"; Physical Review Letters **14**, p. 305 (1965). Cited page 26

koonce1967 [86] C. Koonce, M. L. Cohen, J. Schooley, W. Hosler & E. Pfeiffer; "Superconducting transition temperatures of semiconducting $SrTiO_3$"; Physical

Review **163**, p. 380 (1967). Cited page 26

enderlein2020 [87] C. Enderlein, J. F. de Oliveira, D. Tompsett, E. B. Saitovitch, S. Saxena, G. Lonzarich & S. Rowley; "Superconductivity mediated by polar modes in ferroelectric metals"; Nature communications **11**, p. 4852 (2020). Cited page 26

Beck1974 [88] H. Beck, P. F. Meier & A. Thellung; "Phonon hydrodynamics in solids"; physica status solidi (a) **24**, p. 11–63 (1974). https://onlinelibrary.wiley.com/doi/abs/10.1002/pssa.2210240102; https://onlinelibrary.wiley.com/doi/pdf/10.1002/pssa.2210240102. Cited page 27

Hehlen1995 [89] B. Hehlen, A.-L. Pérou, E. Courtens & R. Vacher; "Observation of a Doublet in the Quasielastic Central Peak of Quantum-Paraelectric $SrTiO_3$"; Phys. Rev. Lett. **75**, p. 2416–2419 (1995). https://link.aps.org/doi/10.1103/PhysRevLett.75.2416. Cited page 27

Koreeda2007 [90] A. Koreeda, R. Takano & S. Saikan; "Second Sound in $SrTiO_3$"; Phys. Rev. Lett. **99**, p. 265 502 (2007). https://link.aps.org/doi/10.1103/PhysRevLett.99.265502. Cited page 27

Bussmann1997 [91] A. Bussmann-Holder; "Electron-phonon-interaction-driven anharmonic mode-mode coupling in ferroelectrics: The origin of acoustic-mode anomalies"; Phys. Rev. B **56**, p. 10 762–10 765 (1997). https://link.aps.org/doi/10.1103/PhysRevB.56.10762. Cited page 27

li2020 [92] X. Li, B. Fauqué, Z. Zhu & K. Behnia; "Phonon thermal Hall effect in strontium titanate"; Physical review letters **124**, p. 105 901 (2020). Cited pages 27, 32, 33, 34, and 79

sonnanche2019 [93] G. Grissonnanche, A. Legros, S. Badoux, E. Lefrançois, V. Zatko, M. Lizaire, F. Laliberté, A. Gourgout, J.-S. Zhou, S. Pyon *et al.*; "Giant thermal Hall conductivity in the pseudogap phase of cuprate superconductors"; Nature **571**, p. 376–380 (2019). Cited pages 27, 31, 32, and 51

sahara2018prl [94] Y. Kasahara, K. Sugii, T. Ohnishi, M. Shimozawa, M. Yamashita, N. Kurita, H. Tanaka, J. Nasu, Y. Motome, T. Shibauchi *et al.*; "Unusual thermal Hall effect in a Kitaev spin liquid candidate α- RuCl 3"; Physical review letters **120**, p. 217 205 (2018). Cited page 27

kasahara2018 [95] Y. Kasahara, T. Ohnishi, Y. Mizukami, O. Tanaka, S. Ma, K. Sugii, N. Kurita, H. Tanaka, J. Nasu, Y. Motome *et al.*; "Majorana quantization and half-integer thermal quantum Hall effect in a Kitaev spin liquid"; Nature **559**, p. 227–231 (2018). Cited pages 27 and 31

hentrich2019 [96] R. Hentrich, M. Roslova, A. Isaeva, T. Doert, W. Brenig, B. Büchner & C. Hess; "Large thermal Hall effect in α- $RuCl_3$: Evidence for heat transport by Kitaev-Heisenberg paramagnons"; Physical Review B **99**, p. 085 136 (2019). Cited page 27

sim2021 [97] S. Sim, H. Yang, H.-L. Kim, M. J. Coak, M. Itoh, Y. Noda & J.-G. Park; "Sizable Suppression of Thermal Hall Effect upon Isotopic Substitution in $SrTiO_3$"; Phys. Rev. Lett. **126**, p. 015 901 (2021). https://link.aps.org/doi/10.1103/PhysRevLett.126.015901. Cited pages 27, 32, 33, 36, and 38

wemple1965 [98] S. WEMPLE; "Some Transport Properties of Oxygen-Deficient Single-Crystal Potassium Tantalate ($KTaO_3$)"; Physical Review **137**, p. A1575 (1965). Cited page 28

farhi2000 [99] E. FARHI, A. TAGANTSEV, R. CURRAT, B. HEHLEN, E. COURTENS & L. BOATNER; "Low energy phonon spectrum and its parameterization in pure $KTaO_3$ below 80 K"; The European Physical Journal B-Condensed Matter and Complex Systems **15**, p. 615–623 (2000). Cited page 28

fujishita2016 [100] H. FUJISHITA, S. KITAZAWA, M. SAITO, R. ISHISAKA, H. OKAMOTO & T. YAMAGUCHI; "Quantum paraelectric states in $SrTiO_3$ and $KTaO_3$: Barrett model, Vendik model, and quantum criticality"; Journal of the Physical Society of Japan **85**, p. 074 703 (2016). Cited page 28

liu2021two [101] C. LIU, X. YAN, D. JIN, Y. MA, H.-W. HSIAO, Y. LIN, T. M. BRETZ-SULLIVAN, X. ZHOU, J. PEARSON, B. FISHER *et al.*; "Two-dimensional superconductivity and anisotropic transport at $KTaO_3$ (111) interfaces"; Science **371**, p. 716–721 (2021). Cited page 28

chen2021KTO [102] Z. CHEN, Y. LIU, H. ZHANG, Z. LIU, H. TIAN, Y. SUN, M. ZHANG, Y. ZHOU, J. SUN & Y. XIE; "Electric field control of superconductivity at the $LaAlO_3/KTaO_3$ (111) interface"; Science **372**, p. 721–724 (2021). Cited page 28

shannon1976 [103] R. D. SHANNON; "Revised effective ionic radii and systematic studies of interatomic distances in halides and chalcogenides"; Acta crystallographica section A: crystal physics, diffraction, theoretical and general crystallography **32**, p. 751–767 (1976). Cited page 28

brous1953 [104] J. BROUS, I. FANKUCHEN & E. BANKS; "Rare earth titanates with a perovskite structure"; Acta crystallographica **6**, p. 67–70 (1953). Cited page 28

Narayan2019 [105] A. NARAYAN, A. CANO, A. V. BALATSKY & N. A. SPALDIN; "Multiferroic quantum criticality"; Nature Materials **18**, p. 223–228 (2019). ISSN 1476-4660. https://doi.org/10.1038/s41563-018-0255-6. Cited page 29

allieta2012 [106] M. ALLIETA, M. SCAVINI, L. J. SPALEK, V. SCAGNOLI, H. C. WALKER, C. PANAGOPOULOS, S. S. SAXENA, T. KATSUFUJI & C. MAZZOLI; "Role of intrinsic disorder in the structural phase transition of magnetoelectric $EuTiO_3$"; Physical Review B **85**, p. 184 107 (2012). Cited page 29

bussmann2011 [107] A. BUSSMANN-HOLDER, J. KÖHLER, R. KREMER & J. LAW; "Relation between structural instabilities in $EuTiO_3$ and $SrTiO_3$"; Physical Review B **83**, p. 212 102 (2011). Cited page 29

Jiang2022 [108] S. JIANG, X. LI, B. FAUQUÉ & K. BEHNIA; "Phonon drag thermal Hall effect in metallic strontium titanate"; Proceedings of the National Academy of Sciences **119**, p. e2201975 119 (2022). Cited pages 31, 59, 63, and 85

mori2014 [109] M. MORI, A. SPENCER-SMITH, O. P. SUSHKOV & S. MAEKAWA; "Origin of the phonon Hall effect in rare-earth garnets"; Physical review letters **113**, p. 265 901 (2014). Cited page 31

onose2010 [110] Y. ONOSE, T. IDEUE, H. KATSURA, Y. SHIOMI, N. NAGAOSA & Y. TOKURA; "Observation of the magnon Hall effect"; Science **329**, p. 297–299 (2010). Cited page 31

liu2017 [111] J. Liu, L. Cornelissen, J. Shan, T. Kuschel & B. Van Wees; "Magnon planar Hall effect and anisotropic magnetoresistance in a magnetic insulator"; Physical Review B **95**, p. 140 402 (2017). Cited page 31

murakami2017 [112] S. Murakami & A. Okamoto; "Thermal Hall effect of magnons"; Journal of the Physical Society of Japan **86**, p. 011 010 (2017). Cited page 31

ideue2017 [113] T. Ideue, T. Kurumaji, S. Ishiwata & Y. Tokura; "Giant thermal Hall effect in multiferroics"; Nature materials **16**, p. 797–802 (2017). Cited pages 31 and 32

boulanger2020 [114] M.-E. Boulanger, G. Grissonnanche, S. Badoux, A. Allaire, É. Lefrançois, A. Legros, A. Gourgout, M. Dion, C. Wang, X. Chen *et al.*; "Thermal Hall conductivity in the cuprate Mott insulators Nd2CuO4 and $Sr_2CuO_2Cl_2$"; Nature communications **11**, p. 5325 (2020). Cited pages 31 and 32

sonnanche2020 [115] G. Grissonnanche, S. Thériault, A. Gourgout, M.-E. Boulanger, E. Lefrançois, A. Ataei, F. Laliberté, M. Dion, J.-S. Zhou, S. Pyon *et al.*; "Chiral phonons in the pseudogap phase of cuprates"; Nature Physics **16**, p. 1108–1111 (2020). Cited pages 31 and 32

chen2022 [116] L. Chen, M.-E. Boulanger, Z.-C. Wang, F. Tafti & L. Taillefer; "Large phonon thermal Hall conductivity in the antiferromagnetic insulator Cu_3TeO_6"; Proceedings of the National Academy of Sciences **119**, p. e2208016 119 (2022). Cited page 32

ataei2023 [117] A. Ataei, G. Grissonnanche, M.-E. Boulanger, L. Chen, E. Lefrancois, V. Brouet & L. Taillefer; "Impurity-induced phonon thermal Hall effect in the antiferromagnetic phase of Sr_2IrO_4"; arXiv preprint arXiv:2302.03796 (2023). Cited page 32

li2023 [118] X. Li, Y. Machida, A. Subedi, Z. Zhu, L. Li & K. Behnia; "The phonon thermal Hall angle in black phosphorus"; Nature Communications **14**, p. 1027 (2023). Cited page 32

schberger2015 [119] M. Hirschberger, J. W. Krizan, R. Cava & N. Ong; "Large thermal Hall conductivity of neutral spin excitations in a frustrated quantum magnet"; Science **348**, p. 106–109 (2015). Cited page 32

uehara2022 [120] T. Uehara, T. Ohtsuki, M. Udagawa, S. Nakatsuji & Y. Machida; "Phonon thermal Hall effect in a metallic spin ice"; Nature Communications **13**, p. 4604 (2022). Cited pages 32 and 78

blanc1971 [121] J. Blanc & D. L. Staebler; "Electrocoloration in srti o 3: Vacancy drift and oxidation-reduction of transition metals"; Physical Review B **4**, p. 3548 (1971). Cited page 34

lee2016 [122] S. A. Lee, H. Jeong, S. Woo, J.-Y. Hwang, S.-Y. Choi, S.-D. Kim, M. Choi, S. Roh, H. Yu, J. Hwang *et al.*; "Erratum: Phase transitions via selective elemental vacancy engineering in complex oxide thin films"; Scientific Reports **6** (2016). Cited page 34

spinelli2010 [123] A. Spinelli, M. A. Torija, C. Liu, C. Jan & C. Leighton; "Electronic transport in doped $SrTiO_3$: Conduction mechanisms and potential applications"; Phys. Rev. B **81**, p. 155 110 (2010). https://link.aps.org/doi/10.1103/PhysRevB.81.155110. Cited pages 34, 35, and 56

wang2019 [124] J. WANG, L. YANG, C. W. RISCHAU, Z. XU, Z. REN, T. LORENZ, J. HEMBERGER, X. LIN & K. BEHNIA; "Charge transport in a polar metal"; npj Quantum Materials **4**, p. 61 (2019). ISSN 2397-4648. https://doi.org/10.1038/s41535-019-0200-1. Cited page 36

rischau2022 [125] C. W. RISCHAU, D. PULMANNOVÁ, G. W. SCHEERER, A. STUCKY, E. GIANNINI & D. VAN DER MAREL; "Isotope tuning of the superconducting dome of strontium titanate"; Phys. Rev. Research **4**, p. 013 019 (2022). https://link.aps.org/doi/10.1103/PhysRevResearch.4.013019. Cited page 36

bhowal2023 [126] S. BHOWAL & N. A. SPALDIN; "Polar metals: principles and prospects"; Annual Review of Materials Research **53**, p. 53–79 (2023). Cited page 36

Collignon2021 [127] C. COLLIGNON, Y. AWASHIMA, RAVI, X. LIN, C. W. RISCHAU, A. ACHECHE, B. VIGNOLLE, C. PROUST, Y. FUSEYA, K. BEHNIA & B. FAUQUÉ; "Quasi-isotropic orbital magnetoresistance in lightly doped $SrTiO_3$"; Phys. Rev. Materials **5**, p. 065 002 (2021). https://link.aps.org/doi/10.1103/PhysRevMaterials.5.065002. Cited pages 40, 44, 49, 61, and 62

Herring1954 [128] C. HERRING; "Theory of the Thermoelectric Power of Semiconductors"; Phys. Rev. **96**, p. 1163–1187 (1954). https://link.aps.org/doi/10.1103/PhysRev.96.1163. Cited pages 45 and 48

Gurevich1989 [129] Y. GUREVICH & O. MASHKEVICH; "The electron-phonon drag and transport phenomena in semiconductors"; Physics Reports **181**, p. 327–394 (1989). ISSN 0370-1573. https://www.sciencedirect.com/science/article/pii/0370157389900112. Cited page 45

MacDonald [130] D. K. C. MACDONALD; *Thermoelectricity : an introduction to the principles* (Dover Publications) (2006). Cited page 45

Cain2013 [131] T. A. CAIN, A. P. KAJDOS & S. STEMMER; "La-doped $SrTiO_3$ films with large cryogenic thermoelectric power factors"; Applied Physics Letters **102**, p. 182 101 (2013). Cited pages 45, 46, and 47

Collignon2020 [132] C. COLLIGNON, P. BOURGES, B. FAUQUÉ & K. BEHNIA; "Heavy Nondegenerate Electrons in Doped Strontium Titanate"; Phys. Rev. X **10**, p. 031 025 (2020). https://link.aps.org/doi/10.1103/PhysRevX.10.031025. Cited pages 45, 50, 56, and 71

Mousatov2021 [133] C. H. MOUSATOV & S. A. HARTNOLL; "Phonons, electrons and thermal transport in Planckian high T_c materials"; npj Quantum Materials **6**, p. 81 (2021). Cited page 49

REHWALD [134] W. REHWALD; "Anomalous ultrasonic attenuation at the 105°K transition in strontium titanate"; Solid State Communications **8**, p. 607–611 (1970). ISSN 0038-1098. https://www.sciencedirect.com/science/article/pii/0038109870901596. Cited page 49

Kumar2021 [135] A. KUMAR, V. I. YUDSON & D. L. MASLOV; "Quasiparticle and Nonquasiparticle Transport in Doped Quantum Paraelectrics"; Phys. Rev. Lett. **126**, p. 076 601 (2021). https://link.aps.org/doi/10.1103/PhysRevLett.126.076601.

Cited pages 50 and 54

Nazaryan2021 [136] K. G. Nazaryan & M. V. Feigel'man; "Conductivity and thermoelectric coefficients of doped $SrTiO_3$ at high temperatures"; Phys. Rev. B **104**, p. 115 201 (2021). https://link.aps.org/doi/10.1103/PhysRevB.104.115201. Cited pages 50 and 54

Behnia_2016 [137] K. Behnia & H. Aubin; "Nernst effect in metals and superconductors: a review of concepts and experiments"; Reports on Progress in Physics **79**, p. 046 502 (2016). https://doi.org/10.1088/0034-4885/79/4/046502. Cited page 51

Fauque2013 [138] B. Fauqué, N. P. Butch, P. Syers, J. Paglione, S. Wiedmann, A. Collaudin, B. Grena, U. Zeitler & K. Behnia; "Magnetothermoelectric properties of Bi_2Se_3"; Phys. Rev. B **87**, p. 035 133 (2013). https://link.aps.org/doi/10.1103/PhysRevB.87.035133. Cited page 51

Jaoui2020 [139] A. Jaoui, G. Seyfarth, C. W. Rischau, S. Wiedmann, S. Benhabib, C. Proust, K. Behnia & B. Fauqué; "Giant Seebeck effect across the field-induced metal-insulator transition of InAs"; npj Quantum Materials **5**, p. 94 (2020). ISSN 2397-4648. https://doi.org/10.1038/s41535-020-00296-0. Cited page 51

bookPbTe [140] Y. I. Ravich, B. A. Efimova & I. A. Smirnov; *Semiconducting Lead Chalcogenides*; Monographs in Semiconductor Physics 5; 1re édition (Springer US) (1970). Cited page 51

Ando2004 [141] Y. Ando, Y. Kurita, S. Komiya, S. Ono & K. Segawa; "Evolution of the Hall Coefficient and the Peculiar Electronic Structure of the Cuprate Superconductors"; Phys. Rev. Lett. **92**, p. 197 001 (2004). https://link.aps.org/doi/10.1103/PhysRevLett.92.197001. Cited page 51

jiang2023 [142] S. Jiang, B. Fauqué & K. Behnia; "T-Square Dependence of the Electronic Thermal Resistivity of Metallic Strontium Titanate"; Physical Review Letters **131**, p. 016 301 (2023). Cited page 53

Landau1936 [143] L. Landau & I. Pomerantschuk; "Über Eigneschaften der metalle bei sehr niedrigen Temperaturen"; Phys. Z. Sowjet **10**, p. 649–653 (1936). Cited page 53

Joynt2002 [144] R. Joynt & L. Taillefer; "The superconducting phases of UPt_3"; Rev. Mod. Phys. **74**, p. 235–294 (2002). https://link.aps.org/doi/10.1103/RevModPhys.74.235. Cited page 53

Maeno1997 [145] Y. Maeno, K. Yoshida, H. Hashimoto, S. Nishizaki, S.-i. Ikeda, M. Nohara, T. Fujita, A. Mackenzie, N. Hussey, J. Bednorz & F. Lichtenberg; "Two-Dimensional Fermi Liquid Behavior of the Superconductor Sr_2RuO_4"; Journal of the Physical Society of Japan **66**, p. 1405–1408 (1997). https://doi.org/10.1143/JPSJ.66.1405; https://doi.org/10.1143/JPSJ.66.1405. Cited page 53

Hartman1969 [146] R. Hartman; "Temperature Dependence of the Low-Field Galvanomagnetic Coefficients of Bismuth"; Phys. Rev. **181**, p. 1070–1086 (1969). https://link.aps.org/doi/10.1103/PhysRev.181.1070. Cited page 53

Uher1977 [147] C. Uher & W. P. Pratt; "High-Precision, Ultralow-Temperature Resistivity Measurements on Bismuth"; Phys. Rev. Lett. **39**, p. 491–494 (1977). https://link.aps.org/doi/10.1103/PhysRevLett.39.491. Cited page 53

Tsujii2003 [148] N. Tsujii, K. Yoshimura & K. Kosuge; "Deviation from the Kadowaki–Woods relation in Yb-based intermediate-valence systems"; Journal of Physics: Condensed Matter **15**, p. 1993 (2003). Cited page 54

Hussey2005 [149] N. E. Hussey; "Non-generality of the Kadowaki–Woods Ratio in Correlated Oxides"; Journal of the Physical Society of Japan **74**, p. 1107–1110 (2005). https://doi.org/10.1143/JPSJ.74.1107; https://doi.org/10.1143/JPSJ.74.1107. Cited page 54

Li-Maslov [150] S. Li & D. L. Maslov; "Lorentz ratio of a compensated metal"; Phys. Rev. B **98**, p. 245 134 (2018). https://link.aps.org/doi/10.1103/PhysRevB.98.245134. Cited pages 55 and 64

White1967 [151] G. White & R. Tainsh; "Electron scattering in nickel at low temperatures"; Physical Review Letters **19**, p. 165 (1967). Cited page 55

Garland1978 [152] J. Garland & D. Van Harlingen; "Low-temperature electrical and thermal transport properties of pure aluminum"; Journal of Physics F: Metal Physics **8**, p. 117 (1978). Cited page 55

Wagner1971 [153] D. Wagner, J. Garland & R. Bowers; "Low-temperature electrical and thermal resistivities of tungsten"; Physical Review B **3**, p. 3141 (1971). Cited pages 55 and 65

Jaoui2021 [154] A. Jaoui, B. Fauqué & K. Behnia; "Thermal resistivity and hydrodynamics of the degenerate electron fluid in antimony"; Nature Communications **12**, p. 195 (2021). Cited pages 55, 58, and 65

Paglione2005 [155] J. Paglione, M. Tanatar, D. Hawthorn, R. Hill, F. Ronning, M. Sutherland, L. Taillefer, C. Petrovic & P. Canfield; "Heat transport as a probe of electron scattering by spin fluctuations: The case of antiferromagnetic CeRhIn 5"; Physical review letters **94**, p. 216 602 (2005). Cited pages 55 and 65

Jaoui2018 [156] A. Jaoui, B. Fauqué, C. W. Rischau, A. Subedi, C. Fu, J. Gooth, N. Kumar, V. Süss, D. L. Maslov, C. Felser *et al.*; "Departure from the Wiedemann–Franz law in WP_2 driven by mismatch in T-square resistivity prefactors"; npj Quantum Materials **3**, p. 64 (2018). Cited pages 55 and 65

Lussier1994 [157] B. Lussier, B. Ellman & L. Taillefer; "Anisotropy of Heat Conduction in the Heavy Fermion Superconductor U Pt 3"; Physical Review Letters **73**, p. 3294 (1994). Cited pages 55 and 65

Okuda2001 [158] T. Okuda, K. Nakanishi, S. Miyasaka & Y. Tokura; "Large thermoelectric response of metallic perovskites: $Sr_{1-x}La_xTiO_3$ (0< ˜ x < ˜ 0.1)"; Physical Review B **63**, p. 113 104 (2001). Cited page 56

white1958 [159] G. K. White & S. B. Woods; "The thermal and electrical resistivity of bismuth and antimony at low temperatures"; The Philosophical Magazine: A Journal of Theoretical Experimental and Applied Physics **3**, p. 342–359 (1958). Cited page 58

Uher1974 [160] C. Uher & H. J. Goldsmid; "Separation of the Electronic and Lattice Thermal Conductivities in Bismuth Crystals"; physica status solidi (b) **65**, p. 765–772 (1974). Cited page 58

jaoui2022 [161] A. Jaoui, A. Gourgout, G. Seyfarth, A. Subedi, T. Lorenz, B. Fauqué & K. Behnia; "Formation of an Electron-Phonon Bifluid in Bulk Antimony"; Phys. Rev. X **12**, p. 031 023 (2022).

https://link.aps.org/doi/10.1103/PhysRevX.12.031023. Cited page 58

iaokangLi2020 [162] X. Li, B. Fauqué, Z. Zhu & K. Behnia; "Phonon Thermal Hall Effect in Strontium Titanate"; Phys. Rev. Lett. **124**, p. 105 901 (2020). https://link.aps.org/doi/10.1103/PhysRevLett.124.105901. Cited page 59

rischau2021 [163] C. W. Rischau, Y. Li, B. Fauqué, H. Inoue, M. Kim, C. Bell, H. Y. Hwang, A. Kapitulnik & K. Behnia; "Universal bound to the amplitude of the vortex Nernst signal in superconductors"; Physical review letters **126**, p. 077 001 (2021). Cited page 63

Fauque2022b [164] B. Fauqué, C. Collignon, H. Yoon, Ravi, X. Lin, I. Mazin, H. Y. Hwang & K. Behnia; "An electronic band sculpted by oxygen vacancies and indispensable for dilute superconductivity"; arXiv e-prints (2022). Cited page 64

Paglione2006 [165] J. Paglione, M. A. Tanatar, D. G. Hawthorn, F. Ronning, R. W. Hill, M. Sutherland, L. Taillefer & C. Petrovic; "Nonvanishing Energy Scales at the Quantum Critical Point of $CeCoIn_5$"; Phys. Rev. Lett. **97**, p. 106 606 (2006). https://link.aps.org/doi/10.1103/PhysRevLett.97.106606. Cited page 65

Dobbs [166] E. R. Dobbs; *Helium Three* (Oxford University Press) (2000). Cited page 65

Leggett_2016 [167] A. J. Leggett; "Liquid ^{3}He: a strongly correlated but well understood Fermi liquid"; Reports on Progress in Physics **79**, p. 054 501 (2016). https://dx.doi.org/10.1088/0034-4885/79/5/054501. Cited page 65

brikosov_1959 [168] A. A. Abrikosov & I. M. Khalatnikov; "The theory of a Fermi liquid (the properties of liquid ^{3}He at low temperatures)"; Reports on Progress in Physics **22**, p. 329–367 (1959). Cited page 65

greywall1984 [169] D. S. Greywall; "Thermal conductivity of normal liquid ^{3}He"; Physical Review B **29**, p. 4933 (1984). Cited page 65

Dy1969 [170] K. S. Dy & C. J. Pethick; "Transport Coefficients of a Normal Fermi Liquid: Application to Liquid He^3"; Phys. Rev. **185**, p. 373–384 (1969). https://link.aps.org/doi/10.1103/PhysRev.185.373. Cited page 65

Sykes1970 [171] J. Sykes & G. A. Brooker; "The transport coefficients of a fermi liquid"; Annals of Physics **56**, p. 1–39 (1970). Cited page 65

wolfle1979 [172] P. Wolfle; "Low-temperature properties of liquid ^{3}He"; Reports on Progress in Physics **42**, p. 269–346 (1979). Cited pages 65 and 66

Lin2014b [173] X. Lin, G. Bridoux, A. Gourgout, G. Seyfarth, S. Krämer, M. Nardone, B. Fauqué & K. Behnia; "Critical Doping for the Onset of a Two-Band Superconducting Ground State in $SrTiO_{3-\delta}$"; Phys. Rev. Lett. **112**, p. 207 002 (2014). https://link.aps.org/doi/10.1103/PhysRevLett.112.207002. Cited page 66

McCalla [174] E. McCalla, M. N. Gastiasoro, G. Cassuto, R. M. Fernandes & C. Leighton; "Low-temperature specific heat of doped $SrTiO_3$: Doping dependence of the effective mass and Kadowaki-Woods scaling violation"; Phys. Rev. Materials **3**, p. 022 001 (2019). https://link.aps.org/doi/10.1103/PhysRevMaterials.3.022001. Cited page 66

Ambler1966 [175] E. Ambler, J. H. Colwell, W. R. Hosler & J. F. Schooley; "Magnetization and Critical Fields of Superconducting $SrTiO_3$"; Phys. Rev. **148**, p. 280–286 (1966).

https://link.aps.org/doi/10.1103/PhysRev.148.280. Cited page 66

Pfitzner1985 [176] M. PFITZNER; "General polynomial expansion of the quasiparticle scattering amplitude in normal Fermi fluids"; Journal of Low Temperature Physics **61**, p. 141–154 (1985). ISSN 1573-7357. https://doi.org/10.1007/BF00682734. Cited page 66

Vollhardt1990 [177] D. VOLLHARDT & P. WOLFLE; *The superfluid phases of helium 3* (CRC Press) (1990). Cited page 66

Behnia2022b [178] K. BEHNIA; "On the dynamic distinguishability of nodal quasi-particles in overdoped cuprates"; SciPost Phys. **12**, p. 200 (2022). https://scipost.org/10.21468/SciPostPhys.12.6.200. Cited page 66

Pfitzner1983 [179] M. PFITZNER & P. WÖLFLE; "Quasiparticle scattering amplitude for normal liquid3He"; Journal of Low Temperature Physics **51**, p. 535–559 (1983). ISSN 1573-7357. https://doi.org/10.1007/BF00683227. Cited page 66

Pftiznzer1987 [180] M. PFITZNER & P. WÖLFLE; "Quasiparticle interaction in theFermi liquid ^{3}He"; Phys. Rev. B **35**, p. 4699–4712 (1987). https://link.aps.org/doi/10.1103/PhysRevB.35.4699. Cited page 66

Vollhardt1984 [181] D. VOLLHARDT; "Normal ^{3}He: an almost localized Fermi liquid"; Rev. Mod. Phys. **56**, p. 99–120 (1984). https://link.aps.org/doi/10.1103/RevModPhys.56.99. Cited page 66

jaoui2023 [182] A. JAOUI, S. JIANG, X. LI, Y. TOMIOKA, I. H. INOUE, J. ENGELMAYER, R. SHARMA, L. PÄTZOLD, T. LORENZ, B. FAUQUÉ *et al.*; "Glass-like thermal conductivity and narrow insulating gap of EuTiO _3"; arXiv preprint arXiv:2307.02058 (2023). Cited page 69

McGuire [183] T. R. MCGUIRE, M. W. SHAFER, R. J. JOENK, H. A. ALPERIN & S. J. PICKART; "Magnetic Structure of $EuTiO_3$"; Journal of Applied Physics **37**, p. 981–982 (1966). https://doi.org/10.1063/1.1708549; https://doi.org/10.1063/1.1708549. Cited pages 69, 76, and 83

ngelmeyer2019 [184] J. ENGELMAYER, X. LIN, C. P. GRAMS, R. GERMAN, T. FRÖHLICH, J. HEMBERGER, K. BEHNIA & T. LORENZ; "Charge transport in oxygen-deficient $EuTiO_3$: The emerging picture of dilute metallicity in quantum-paraelectric perovskite oxides"; Phys. Rev. Materials **3**, p. 051 401 (2019). https://link.aps.org/doi/10.1103/PhysRevMaterials.3.051401. Cited pages 70, 76, and 77

Katsufuji1999 [185] T. KATSUFUJI & Y. TOKURA; "Transport and magnetic properties of a ferromagnetic metal: $Eu_{1-x}R_xTiO_3$"; Phys. Rev. B **60**, p. R15 021–R15 023 (1999). https://link.aps.org/doi/10.1103/PhysRevB.60.R15021. Cited page 70

hchanskii2012 [186] K. Z. RUSHCHANSKII, N. A. SPALDIN & M. LEŽAIĆ; "First-principles prediction of oxygen octahedral rotations in perovskite-structure $EuTiO_3$"; Phys. Rev. B **85**, p. 104 109 (2012). https://link.aps.org/doi/10.1103/PhysRevB.85.104109. Cited pages 71, 72, and 82

Johnson1953 [187] V. A. JOHNSON & K. LARK-HOROVITZ; "Theory of Thermoelectric Power in Semiconductors with Applications to Germanium"; Phys. Rev. **92**, p. 226–232 (1953). https://link.aps.org/doi/10.1103/PhysRev.92.226. Cited page 71

Kennedy_2014 [188] B. J. Kennedy, G. Murphy, E. Reynolds, M. Avdeev, H. E. R. Brand & T. Kolodiazhnyi; "Studies of the antiferrodistortive transition in $EuTiO_3$"; Journal of Physics: Condensed Matter **26**, p. 495 901 (2014). https://dx.doi.org/10.1088/0953-8984/26/49/495901. Cited page 72

Malyi2022 [189] O. I. Malyi, X.-G. Zhao, A. Bussmann-Holder & A. Zunger; "Local positional and spin symmetry breaking as a source of magnetism and insulation in paramagnetic $EuTiO_3$"; Phys. Rev. Materials **6**, p. 034 604 (2022). https://link.aps.org/doi/10.1103/PhysRevMaterials.6.034604. Cited pages 72, 83, 84, and 86

Ranjan_2007 [190] R. Ranjan, H. S. Nabi & R. Pentcheva; "Electronic structure and magnetism of $EuTiO_3$: a first-principles study"; Journal of Physics: Condensed Matter **19**, p. 406 217 (2007). https://dx.doi.org/10.1088/0953-8984/19/40/406217. Cited page 72

Lee2009 [191] J. H. Lee, X. Ke, N. J. Podraza, L. F. Kourkoutis, T. Heeg, M. Roeckerath, J. W. Freeland, C. J. Fennie, J. Schubert, D. A. Muller, P. Schiffer & D. G. Schlom; "Optical band gap and magnetic properties of unstrained $EuTiO_3$ films"; Applied Physics Letters **94** (2009). ISSN 0003-6951. https://doi.org/10.1063/1.3133351. Cited page 72

Akamatsu2012 [192] H. Akamatsu, K. Fujita, H. Hayashi, T. Kawamoto, Y. Kumagai, Y. Zong, K. Iwata, F. Oba, I. Tanaka & K. Tanaka; "Crystal and Electronic Structure and Magnetic Properties of Divalent Europium Perovskite Oxides $EuMO_3$ (M = Ti, Zr, and Hf): Experimental and First-Principles Approaches"; Inorganic Chemistry **51**, p. 4560–4567 (2012). https://doi.org/10.1021/ic2024567; pMID: 22468559; https://doi.org/10.1021/ic2024567. Cited pages 72 and 76

Lindsay2013 [193] L. Lindsay, D. A. Broido & T. L. Reinecke; "Ab initio thermal transport in compound semiconductors"; Phys. Rev. B **87**, p. 165 201 (2013). https://link.aps.org/doi/10.1103/PhysRevB.87.165201. Cited page 74

subedi21 [194] A. Subedi; "First principles study of thermal conductivity of In_2O_3 in relation to Al_2O_3, Ga_2O_3, and $KTaO_3$"; (2021); 2101.02664. Cited page 74

ndersande1986 [195] J. W. Vandersande & C. Wood; "The thermal conductivity of insulators and semiconductors"; Contemporary Physics **27**, p. 117–144 (1986). https://doi.org/10.1080/00107518608211003; https://doi.org/10.1080/00107518608211003. Cited pages 74 and 78

Allen1999 [196] P. B. Allen, J. L. Feldman, J. Fabian & F. Wooten; "Diffusons, locons and propagons: Character of atomic vibrations in amorphous Si"; Philosophical Magazine B **79**, p. 1715–1731 (1999). https://doi.org/10.1080/13642819908223054; https://doi.org/10.1080/13642819908223054. Cited page 74

seyf2016 [197] H. R. Seyf & A. Henry; "A method for distinguishing between propagons, diffusions, and locons"; Journal of Applied Physics **120**, p. 025 101 (2016). https://doi.org/10.1063/1.4955420; https://doi.org/10.1063/1.4955420. Cited page 74

imoncelli2019 [198] M. Simoncelli, N. Marzari & F. Mauri; "Unified theory of thermal transport in

crystals and glasses"; Nature Physics **15**, p. 809–813 (2019). ISSN 1745-2481. https://doi.org/10.1038/s41567-019-0520-x. Cited pages 74 and 84

Isaeva2019 [199] L. ISAEVA, G. BARBALINARDO, D. DONADIO & S. BARONI; "Modeling heat transport in crystals and glasses from a unified lattice-dynamical approach"; Nature Communications **10**, p. 3853 (2019). ISSN 2041-1723. https://doi.org/10.1038/s41467-019-11572-4. Cited pages 74 and 84

Visser1997 [200] D. W. VISSER, A. P. RAMIREZ & M. A. SUBRAMANIAN; "Thermal Conductivity of Manganite Perovskites: Colossal Magnetoresistance as a Lattice-Dynamics Transition"; Phys. Rev. Lett. **78**, p. 3947–3950 (1997). https://link.aps.org/doi/10.1103/PhysRevLett.78.3947. Cited pages 74 and 78

Takahata2000 [201] K. TAKAHATA, Y. IGUCHI, D. TANAKA, T. ITOH & I. TERASAKI; "Low thermal conductivity of the layered oxide (Na,Ca)Co_2O_4: Another example of a phonon glass and an electron crystal"; Phys. Rev. B **61**, p. 12 551–12 555 (2000). https://link.aps.org/doi/10.1103/PhysRevB.61.12551. Cited page 74

Li2013 [202] Q. J. LI, Z. Y. ZHAO, C. FAN, F. B. ZHANG, H. D. ZHOU, X. ZHAO & X. F. SUN; "Phonon-glass-like behavior of magnetic origin in single-crystal $Tb_2Ti_2O_7$"; Phys. Rev. B **87**, p. 214 408 (2013). https://link.aps.org/doi/10.1103/PhysRevB.87.214408. Cited pages 74, 78, and 79

CHIBANA201316 [203] M. TACHIBANA; "Thermal conductivity of pyrochlore $R_2Ti_2O_7$ (R=rare earth)"; Solid State Communications **174**, p. 16–18 (2013). ISSN 0038-1098. https://www.sciencedirect.com/science/article/pii/S0038109813004183. Cited pages 74 and 80

Sugii2017 [204] K. SUGII, M. SHIMOZAWA, D. WATANABE, Y. SUZUKI, M. HALIM, M. KIMATA, Y. MATSUMOTO, S. NAKATSUJI & M. YAMASHITA; "Thermal Hall Effect in a Phonon-Glass $Ba_3CuSb_2O_9$"; Phys. Rev. Lett. **118**, p. 145 902 (2017). https://link.aps.org/doi/10.1103/PhysRevLett.118.145902. Cited page 74

Dutta2019 [205] M. DUTTA, S. MATTEPPANAVAR, M. V. D. PRASAD, J. PANDEY, A. WARANKAR, P. MANDAL, A. SONI, U. V. WAGHMARE & K. BISWAS; "Ultralow Thermal Conductivity in Chain-like TlSe Due to Inherent Tl^+ Rattling"; Journal of the American Chemical Society **141**, p. 20 293–20 299 (2019). ISSN 0002-7863. https://doi.org/10.1021/jacs.9b10551. Cited page 74

NUS2021100344 [206] R. HANUS, J. GEORGE, M. WOOD, A. BONKOWSKI, Y. CHENG, D. L. ABERNATHY, M. E. MANLEY, G. HAUTIER, G. J. SNYDER & R. P. HERMANN; "Uncovering design principles for amorphous-like heat conduction using two-channel lattice dynamics"; Materials Today Physics **18**, p. 100 344 (2021). ISSN 2542-5293. https://www.sciencedirect.com/science/article/pii/S2542529321000055. Cited pages 74 and 84

Snyder2008 [207] G. J. SNYDER & E. S. TOBERER; "Complex thermoelectric materials"; Nature Materials **7**, p. 105–114 (2008). ISSN 1476-4660. https://doi.org/10.1038/nmat2090. Cited page 74

Midya2016 [208] A. MIDYA, P. MANDAL, K. RUBI, R. CHEN, J.-S. WANG, R. MAHENDIRAN, G. LORUSSO & M. EVANGELISTI; "Large adiabatic temperature and magnetic entropy changes in $EuTiO_3$"; Phys. Rev. B **93**, p. 094 422 (2016).

https://link.aps.org/doi/10.1103/PhysRevB.93.094422. Cited pages 76 and 80

Chien1974 [209] C.-L. Chien, S. DeBenedetti & F. D. S. Barros; "Magnetic properties of $EuTiO_3$, Eu_2TiO_4, and $Eu_3Ti_2O_7$"; Phys. Rev. B **10**, p. 3913–3922 (1974). https://link.aps.org/doi/10.1103/PhysRevB.10.3913. Cited page 76

Petrovic2013 [210] A. P. Petrović, Y. Kato, S. S. Sunku, T. Ito, P. Sengupta, L. Spalek, M. Shimuta, T. Katsufuji, C. D. Batista, S. S. Saxena & C. Panagopoulos; "Electric field modulation of the tetragonal domain orientation revealed in the magnetic ground state of quantum paraelectric $EuTiO_3$"; Phys. Rev. B **87**, p. 064 103 (2013). https://link.aps.org/doi/10.1103/PhysRevB.87.064103. Cited pages 76 and 79

Stockert2020 [211] U. Stockert, S. Seiro, N. Caroca-Canales, E. Hassinger & C. Geibel; "Valence effect on the thermopower of Eu systems"; Phys. Rev. B **101**, p. 235 106 (2020). https://link.aps.org/doi/10.1103/PhysRevB.101.235106. Cited pages 76 and 83

Zeller1971 [212] R. C. Zeller & R. O. Pohl; "Thermal Conductivity and Specific Heat of Noncrystalline Solids"; Phys. Rev. B **4**, p. 2029–2041 (1971). https://link.aps.org/doi/10.1103/PhysRevB.4.2029. Cited pages 78 and 79

Berggold2008 [213] K. Berggold, M. Kriener, P. Becker, M. Benomar, M. Reuther, C. Zobel & T. Lorenz; "Anomalous expansion and phonon damping due to the Co spin-state transition in $RCoO_3$"; Physical Review B **78**, p. 134 402 (2008). ISSN 1098-0121. https://link.aps.org/doi/10.1103/PhysRevB.78.134402. Cited pages 78 and 79

Inyushkin2010 [214] A. V. Inyushkin & A. N. Taldenkov; "Low-temperature thermal conductivity of terbium-gallium garnet"; Journal of Experimental and Theoretical Physics **111** (2010). ISSN 1063-7761. https://www.osti.gov/biblio/21443350. Cited page 78

Fauque2015 [215] B. Fauqué, X. Xu, A. F. Bangura, E. C. Hunter, A. Yamamoto, K. Behnia, A. Carrington, H. Takagi, N. E. Hussey & R. S. Perry; "Thermal conductivity across the metal-insulator transition in the single-crystalline hyperkagome antiferromagnet $Na_{3+x}Ir_3O_8$"; Phys. Rev. B **91**, p. 075 129 (2015). https://link.aps.org/doi/10.1103/PhysRevB.91.075129. Cited page 78

Baier2005 [216] J. Baier, S. Jodlauk, M. Kriener, A. Reichl, C. Zobel, H. Kierspel, A. Freimuth & T. Lorenz; "Spin-state transition and metal-insulator transition in $La_{1-x}Eu_xCoO_3$"; Phys. Rev. B **71**, p. 014 443 (2005). https://link.aps.org/doi/10.1103/PhysRevB.71.014443. Cited page 79

teigmeier1968 [217] E. F. Steigmeier; "Field Effect on the Cochran Modes in $SrTiO_3$ and $KTaO_3$"; Phys. Rev. **168**, p. 523–530 (1968). https://link.aps.org/doi/10.1103/PhysRev.168.523. Cited page 79

Salce_1994 [218] B. Salce, J. L. Gravil & L. A. Boatner; "Disorder and thermal transport in undoped $KTaO_3$"; Journal of Physics: Condensed Matter **6**, p. 4077–4092 (1994). https://doi.org/10.1088/0953-8984/6/22/007. Cited pages 79 and 80

Heyer_2011 [219] O. Heyer, P. Link, D. Wandner, U. Ruschewitz & T. Lorenz; "Thermodynamic properties and resistivity of the ferromagnetic semiconductor EuC_2"; New Journal of Physics **13**, p. 113 041 (2011). https://dx.doi.org/10.1088/1367-2630/13/11/113041. Cited page 80

Yang1992 [220] G. Yang, A. D. Migone & K. W. Johnson; "Heat capacity and thermal diffusivity of a glass sample"; Phys. Rev. B **45**, p. 157–160 (1992). https://link.aps.org/doi/10.1103/PhysRevB.45.157. Cited page 81

Okai1975 [221] B. Okai & J. Yoshimoto; "Pressure Dependence of the Structural Phase Transition Temperature in $SrTiO_3$ and $KMnF_3$"; Journal of the Physical Society of Japan **39**, p. 162–165 (1975). https://doi.org/10.1143/JPSJ.39.162; https://doi.org/10.1143/JPSJ.39.162. Cited page 82

euvekamp_2015 [222] P. Reuvekamp, K. Caslin, Z. Guguchia, H. Keller, R. K. Kremer, A. Simon, J. Köhler & A. Bussmann-Holder; "Tiny cause with huge impact: polar instability through strong magneto-electric-elastic coupling in bulk $EuTiO_3$"; Journal of Physics: Condensed Matter **27**, p. 262 201 (2015). https://dx.doi.org/10.1088/0953-8984/27/26/262201. Cited page 82

Akamatsu2011 [223] H. Akamatsu, Y. Kumagai, F. Oba, K. Fujita, H. Murakami, K. Tanaka & I. Tanaka; "Antiferromagnetic superexchange via 3*d* states of titanium in $EuTiO_3$ as seen from hybrid Hartree-Fock density functional calculations"; Phys. Rev. B **83**, p. 214 421 (2011). https://link.aps.org/doi/10.1103/PhysRevB.83.214421. Cited page 83

Fennie2006 [224] C. J. Fennie & K. M. Rabe; "Magnetic and Electric Phase Control in Epitaxial $EuTiO_3$ from First Principles"; Phys. Rev. Lett. **97**, p. 267 602 (2006). https://link.aps.org/doi/10.1103/PhysRevLett.97.267602. Cited page 83

Feng_2015 [225] L. Feng, T. Shiga & J. Shiomi; "Phonon transport in perovskite $SrTiO_3$ from first principles"; Applied Physics Express **8**, p. 071 501 (2015). https://dx.doi.org/10.7567/APEX.8.071501. Cited page 83

Petit2021 [226] S. Petit, F. Damay, Q. Berrod & J. M. Zanotti; "Spin and lattice dynamics in the two-singlet system $Tb_3Ga_5O_{12}$"; Phys. Rev. Research **3**, p. 013 030 (2021). https://link.aps.org/doi/10.1103/PhysRevResearch.3.013030. Cited page 83